

LONG PERIOD VARIABLES IN  
LOCAL GROUP DWARF GALAXIES



Jan M. Snigula



# LONG PERIOD VARIABLES IN LOCAL GROUP DWARF GALAXIES

**Ph.D. Thesis**

at the Faculty of Physics & Astronomy  
of the  
Ludwig-Maximilian University Munich

submitted by

**Jan M. Snigula**

from Munich

Munich, December 2005

1. Evaluator: Prof. Dr. Ralf Bender

2. Evaluator: Dr. Achim Weiss

Date of the oral exam: 23. February 2006



Deep into that darkness peering, long I stood there wondering, fearing,  
Doubting, dreaming dreams no mortal ever dared to dream before  
But the silence was unbroken, and the darkness gave no token [...]

– E. A. Poe, The Raven

*to all those who made this possible*



## Zusammenfassung

Zwerggalaxien sind die kleinsten uns bekannten Galaxien. Zugleich sind sie die zahlreichsten Galaxien im Universum. Moderne Untersuchungen zeigen, daß sie Überreste der Bausteine sind aus denen im frühen Universum die Galaxien entstanden sind, die wir heute beobachten. Unsere eigene Galaxie, die Milchstraße, ist Teil einer kleinen Ansammlung von Galaxien, genannt die Lokale Gruppe. Diese Gruppe wird von zwei großen Spiralgalaxien dominiert (der Milchstraße und der Andromeda Galaxie), enthält aber zugleich eine große Anzahl von Zwerggalaxien. Diese Zwerggalaxien sind die uns nächsten Vertreter ihrer Art, und damit nah genug um Rückschlüsse auf ihre stellare Zusammensetzung und Entwicklungsgeschichte zu erlauben.

In dieser Arbeit stelle ich die Ergebnisse einer Suche nach veränderlichen Sternen in mehreren irregulärer Zwerggalaxien der Lokalen Gruppe vor. Das Augenmerk dieser Arbeit liegt dabei auf einer Suche nach Pulsationsveränderlichen mit langen Perioden ( $\sim 300$  Tage). Das Vorkommen dieses Variablentyps erlaubt es, Rückschlüsse auf die Zusammensetzung und das Alter einer stellaren Population zu ziehen.

Zu diesem Zweck wurden über mehrere Jahre mit dem institutseigenen 80 cm Teleskop auf dem Wendelstein verschiedene Zwerggalaxien regelmäßig beobachtet. Zusätzlich wurden Aufnahmen am Calar Alto Observatorium in Spanien gewonnen. Durch Anwendung der „Optimal Image Subtraction“ (OIS) Analyse wurden Sterne mit variabler Helligkeit detektiert. Bei diesem Verfahren werden Aufnahmen aus den verschiedenen Nächten von einem Referenzbild subtrahiert um Variationen in der Helligkeit zu finden. Für diese Kandidaten wurden Perioden, Amplituden und mittlere Helligkeiten bestimmt.

Um einen Vergleich der Ergebnisse untereinander und mit publizierten Daten zu ermöglichen, wurden die gemessenen Magnituden kalibriert. Dazu wurden einerseits am Calar Alto gewonnene Aufnahmen von Standardsternen und andererseits publizierte Photometrie für mit dem Hubble Space Telescope aufgenommene Daten verwendet und die Ergebnisse miteinander verglichen.

Um mögliche Unvollständigkeiten im Datensatz zu erkennen, wurden Vollständigkeitsimulationen durchgeführt. Hierbei wurde darauf Wert gelegt, den gesamten relevanten Parameterraum (Periode, Amplitude und Helligkeit) auszutesten.

Die gewonnenen Daten wurden dazu verwendet, Rückschlüsse über die Sternentstehungsgeschichte der untersuchten Zwerggalaxien zu ziehen. Hierzu wurden einerseits Farben-Helligkeitsdiagramme mit veröffentlichten theoretischen Isochronen verglichen und andererseits die Anzahl der jeweils gefundenen langperiodischen Variablen mit theoretischen Vorhersagen verglichen. Die Masse der Sterne im Stadium langperiodischer Variabilität variiert mit dem Alter der zugrundeliegenden stellaren Population. Mit der Masse variiert auch die Zeit die ein Stern typischerweise auf in dieser Phase verbringt, und damit die Anzahl der zu erwartenden Sterne, in Abhängigkeit der gemessenen Leuchtkraft der Population.

Es wurde gezeigt, daß langperiodische pulsationveränderliche Sterne ein brauchbares Werkzeug zur Analyse der Sternentstehungsgeschichte von Galaxien darstellen. Insbesondere können sie dazu dienen, die Alter-Metallizitäts Entartung unter der die Untersuchung von Farben-Helligkeitsdiagrammen leidet, zu brechen.



# Contents

<b>1</b>	<b>Introduction</b>	<b>1</b>
1.1	The Local Group of galaxies . . . . .	1
1.1.1	Substructure in the Local Group . . . . .	2
1.1.2	Membership to the Local Group . . . . .	2
1.1.3	A word on nomenclature . . . . .	6
1.2	Dwarf galaxies, your small stellar friend . . . . .	6
1.3	Stellar evolution and stellar populations . . . . .	8
1.3.1	Stellar evolution . . . . .	8
1.3.2	Stellar populations . . . . .	11
1.4	Variable stars . . . . .	12
1.5	Outline of the thesis . . . . .	14
<b>2</b>	<b>Observations and data reduction</b>	<b>17</b>
2.1	Object selection . . . . .	17
2.1.1	The observed sample of galaxies . . . . .	18
2.2	Observing strategy . . . . .	23
2.2.1	The Wendelstein observations . . . . .	23
2.2.2	The Calar Alto observations . . . . .	24
2.3	Data reduction . . . . .	25
2.3.1	The standard reduction . . . . .	26
2.3.2	Reference frame creation . . . . .	27
2.3.3	The difference imaging . . . . .	28
<b>3</b>	<b>Photometric calibration</b>	<b>29</b>
3.1	Why the effort? . . . . .	29
3.2	Calibration using HST photometry . . . . .	31
3.3	Calibration using observed standard stars . . . . .	32
3.4	Comparison of results . . . . .	35
<b>4</b>	<b>Catalog of variable sources</b>	<b>37</b>
4.1	Detection of the variable sources . . . . .	37
4.2	Period determination . . . . .	38
4.3	Estimation of the average magnitude . . . . .	39
4.3.1	The general case . . . . .	39
4.3.2	The specific cases . . . . .	41

4.4	The variable source catalog . . . . .	43
4.4.1	Leo A . . . . .	43
4.4.2	DDO 216 . . . . .	45
4.4.3	GR 8 . . . . .	49
4.4.4	DDO 210 . . . . .	50
<b>5</b>	<b>Completeness Simulations</b>	<b>51</b>
5.1	Introduction . . . . .	51
5.2	The technical implementation . . . . .	52
5.2.1	Generation of the light-curves . . . . .	53
5.2.2	Variation mask completeness . . . . .	53
5.2.3	DAOPHOT completeness . . . . .	54
5.2.4	Period search completeness . . . . .	54
5.3	Results . . . . .	54
5.3.1	Results for Leo A . . . . .	54
5.3.2	Results for DDO 216 . . . . .	58
5.3.3	Results for GR 8 . . . . .	61
5.3.4	Results for DDO 210 . . . . .	64
5.4	Summary . . . . .	68
<b>6</b>	<b>Conclusions about the stellar populations</b>	<b>69</b>
6.1	Tracers of the stellar populations . . . . .	69
6.1.1	The fuel consumption theorem . . . . .	69
6.1.2	Application to the data . . . . .	72
6.2	Leo A . . . . .	73
6.3	DDO 216 . . . . .	75
6.4	GR 8 . . . . .	77
6.5	DDO 210 . . . . .	78
<b>7</b>	<b>Telescope control software</b>	<b>81</b>
7.1	Motivation . . . . .	81
7.2	Integration with existing structure . . . . .	82
7.3	Server design . . . . .	82
7.3.1	The client interface . . . . .	84
7.3.2	The TCSState . . . . .	85
7.3.3	The scheduler . . . . .	86
7.3.4	The telescope connection . . . . .	86
7.4	Client software . . . . .	87
7.4.1	The reader GUI . . . . .	88
7.4.2	The control GUI . . . . .	88
<b>8</b>	<b>Summary</b>	<b>91</b>
8.1	Summary . . . . .	91
8.2	Concluding synthesis . . . . .	95
<b>A</b>	<b>Rejected dwarf galaxy candidates</b>	<b>105</b>

---

<b>B</b>	<b>Variable source lightcurves</b>	<b>107</b>
B.1	Light curves of Leo A variables . . . . .	107
B.2	Light curves of DDO 216 variables . . . . .	113
B.3	Light curves of GR 8 variables . . . . .	127
<b>C</b>	<b>TCS daemon commands</b>	<b>129</b>
	<b>Acknowledgements</b>	<b>131</b>
	<b>Curriculum Vitae</b>	<b>133</b>





# List of Figures

1.1	Membership of Local Group galaxies . . . . .	4
1.2	Hubble sequence of galaxies . . . . .	7
1.3	Color-magnitude diagram of nearby stars . . . . .	9
1.4	Stellar evolutionary tracks . . . . .	10
1.5	Color magnitude diagram for the globular cluster M5 . . . . .	11
1.6	Variable stars in the HRD . . . . .	13
2.1	Published distances of the observed dwarf galaxies. . . . .	20
2.2	Timespan and spacing of the obtained observations . . . . .	23
3.1	Comparison of the empirical data points with isochrones . . . . .	32
3.2	HST Calibration for Leo A <i>R</i> -Band . . . . .	33
3.3	Zeropoint fit for NGC 2264 . . . . .	34
3.4	Comparison of the calibration zeropoints . . . . .	35
4.1	Deviation of the reference magnitude from the true one using all available epochs . . . . .	40
4.2	Deviation of the reference magnitude from the true one using the epochs actually used in the reference frame for the Leo A and DDO 216 dwarf galaxies . . . . .	41
4.3	Deviation of the reference magnitude from the true one using the epochs actually used in the reference frame for the GR 8 and DDO 210 dwarf galaxies . . . . .	42
4.4	Finding chart for the detected variables sources in Leo A. . . . .	43
4.5	Luminosity function and color-magnitude diagram of the variables in Leo A . . . . .	44
4.6	Finding chart for the detected variables sources in DDO 216. . . . .	46
4.7	Postage stamps of three variables sources in DDO 216 . . . . .	46
4.8	Luminosity function of the variable sources found in DDO 216 . . . . .	49
4.9	Finding chart and color-magnitude diagram for the detected variables sources in GR 8. . . . .	50
5.1	Results of the completeness simulations for the thresholding on the variation mask and for the detection using the Lafler-Kinman statistic . . . . .	56

5.2	Combined results of the different completeness simulations for the Leo A dwarf galaxy . . . . .	57
5.3	Results of the completeness simulations for the thresholding on the variation mask and for the detection using the Lafler-Kinman statistic for the DDO 216 dwarf galaxy. . . . .	59
5.4	Combined results of the different completeness simulations for the DDO 216 dwarf galaxy . . . . .	60
5.5	Results of the completeness simulations for the thresholding on the variation mask and for the detection using the Lafler-Kinman statistic for the GR 8 dwarf galaxy. . . . .	62
5.6	Combined results of the different completeness simulations for the GR 8 dwarf galaxy . . . . .	63
5.7	Results of the completeness simulations for the thresholding on the variation mask and for the detection using the Lafler-Kinman statistic for the DDO 210 dwarf galaxy. . . . .	66
5.8	Combined results of the different completeness simulations for the DDO 210 dwarf galaxy . . . . .	67
6.1	Specific evolutionary flux . . . . .	71
6.2	Color magnitude diagrams for Leo A . . . . .	73
6.3	Mask and number of TPAGB stars predicted for the Leo A dwarf galaxy	74
6.4	Color magnitude diagrams for DDO 216 . . . . .	76
6.5	Mask and number of TPAGB stars predicted for the DDO 216 dwarf galaxy . . . . .	77
6.6	Color magnitude diagrams for GR 8 . . . . .	78
6.7	Mask and number of TPAGB stars predicted for the GR 8 dwarf galaxy	79
6.8	Color magnitude diagrams for DDO 210 . . . . .	80
6.9	Mask and number of TPAGB stars predicted for the DDO 210 dwarf galaxy . . . . .	80
7.1	Schematic layout of the TCSD telescope control server . . . . .	83
7.2	Schematic layout of the connection procedure between the clients and the server . . . . .	85
7.3	Schematic layout of the central scheduler loop . . . . .	87
7.4	Screenshot of the reader GUI . . . . .	88
7.5	Screenshot of the main window of the control GUI . . . . .	89
7.6	Screenshot of the object selection dialog of the control GUI . . . . .	89
B.1	Lightcurves for variable sources LeoA-1 to LeoA-2 . . . . .	107
B.2	Lightcurves for variable sources LeoA-3 to LeoA-6 . . . . .	108
B.3	Lightcurves for variable sources LeoA-7 to LeoA-10 . . . . .	109
B.4	Lightcurves for variable sources LeoA-11 to LeoA-14 . . . . .	110
B.5	Lightcurves for variable sources LeoA-15 to LeoA-18 . . . . .	111
B.6	Lightcurves for variable sources LeoA-19 to LeoA-22 . . . . .	112
B.7	Lightcurves for variable sources DDO216-1 to DDO216-3 . . . . .	113
B.8	Lightcurves for variable sources DDO216-4 to DDO216-7 . . . . .	114

---

B.9	Lightcurves for variable sources DDO216-8 to DDO216-11 . . . . .	115
B.10	Lightcurves for variable sources DDO216-12 to DDO216-15 . . . . .	116
B.11	Lightcurves for variable sources DDO216-16 to DDO216-19 . . . . .	117
B.12	Lightcurves for variable sources DDO216-20 to DDO216-23 . . . . .	118
B.13	Lightcurves for variable sources DDO216-24 to DDO216-27 . . . . .	119
B.14	Lightcurves for variable sources DDO216-28 to DDO216-31 . . . . .	120
B.15	Lightcurves for variable sources DDO216-32 to DDO216-35 . . . . .	121
B.16	Lightcurves for variable sources DDO216-36 to DDO216-39 . . . . .	122
B.17	Lightcurves for variable sources DDO216-40 to DDO216-43 . . . . .	123
B.18	Lightcurves for variable sources DDO216-44 to DDO216-47 . . . . .	124
B.19	Lightcurves for variable sources DDO216-48 to DDO216-51 . . . . .	125
B.20	Lightcurves for variable sources DDO216-52 to DDO216-55 . . . . .	126
B.21	Lightcurves for variable sources GR8-1 to GR8-3 . . . . .	127



# List of Tables

1.1	Data of certain Local Group members . . . . .	3
2.1	Parameters of the observed dwarf galaxies . . . . .	18
2.2	Alternative names of the observed dwarf galaxies . . . . .	19
2.3	Obtained observations . . . . .	25
3.1	Zeropoints of the HST based calibration . . . . .	33
3.2	Calibration zeropoints using observed standard stars . . . . .	35
4.1	The variable source catalog for Leo A . . . . .	45
4.2	The variable source catalog for DDO 216 . . . . .	48
4.3	The variable source catalog for GR 8 . . . . .	50
5.1	Completeness limits for the thresholding on the variation mask for Leo A	55
5.2	Completeness limits for the detection using the Lafler-Kinman statistic.	57
5.3	Completeness limits for the thresholding on the variation mask for DDO 216 . . . . .	58
5.4	Completeness limits for the detection using the Lafler-Kinman statistic.	60
5.5	Completeness limits for the thresholding on the variation mask for GR 8	63
5.6	Completeness limits for the detection using the Lafler-Kinman statistic.	64
5.7	Completeness limits for the thresholding on the variation mask for DDO 210 . . . . .	65
5.8	Completeness limits for the detection using the Lafler-Kinman statistic for the DDO 210 dwarf . . . . .	67
C.1	Overview of the commands currently implemented in the TCS daemon	130



# Chapter 1

## Introduction

Dwarf galaxies are the least massive, yet most numerous galaxies found in the universe. In our Local Group of galaxies we find a unique sample of dwarf galaxies with a large diversity of masses, metallicities and star formation histories. The distances to many of them remain uncertain despite their relative proximity. A study of their stellar content could help to further our understanding of their origin and evolution, clarifying their role in the context of current galaxy formation and evolution paradigms

This thesis describes the results of a survey for long period variables in a sample of irregular dwarf galaxies in the Local Group. This work covers the long period variables detected. The content of Cepheids, and the resulting distance determinations are covered in a second thesis by [Gössl \(2006\)](#). The aim of this first chapter is to provide the reader with some of the underlying astronomical fundamentals used throughout this work.

### 1.1 The Local Group of galaxies

On a clear night, far from the lights of civilization, lots of stars and nebulae can be seen with the naked eye. But of all these only three are not part of our own galaxy. Two of them, the Magellanic clouds, are nearby irregular dwarf galaxies currently merging with the Galaxy.

The third one, the Andromeda galaxy (M31), a large spiral galaxy, is the most distant object visible with the unaided eye ( $\sim 2 \times 10^6$  Lyrs). It was first mentioned in Al Sudi's "Book of Fixed Stars" in 964 A.D.. For a long time its distance and nature were unknown, it was even considered to be one of the closest nebulae. [Herschel \(1785\)](#) believed its distance would "not exceed 2000 times the distance of Sirius". [Hubble \(1929\)](#) was the first to finally prove the stellar structure of M31, and to measure its distance using the first Cepheid variable found therein.

It was [Hubble \(1936\)](#) as well who first noticed that our own galaxy belongs to "a typical, small group of nebulae which is isolated in the general field" he called the

Local Group. Further investigation showed, that almost half of all galaxies in the universe are part of groups or clusters, thus our Milky Way system resides in a rather typical environment.

The Local Group is dominated by two large spiral galaxies, our own, and the Andromeda galaxy. The rest of the population of the local group consists of a third, smaller, spiral galaxy, M33, a small elliptical galaxy, M32 and numerous dwarf galaxies. The best known are the two Magellanic Clouds in direct neighborhood of the Galaxy, easily visible from the southern hemisphere.

Nowadays the Local group is considered to be composed of a total of at least 36 galaxies (van den Bergh, 2000), but this number is still rather uncertain, as the membership of some galaxies has not been established definitely, and for sure not all dwarf galaxies in the Local Group have been discovered so far.

### 1.1.1 Substructure in the Local Group

The Local Group is divided into three different subgroups (Mateo, 1998), the largest one is dominated by the Galaxy and the Magellanic Cloud pair. The second one is formed by the Andromeda galaxy and its two elliptical satellites (M32 and M110). The third subgroup is basically just a clump of smaller galaxies. Dubbed the “Local Group Cloud” it forms an extended cloud of mostly irregular dwarf galaxies.

Mateo (1998) lists a fourth subgroup, a relatively small group of galaxies composed of NGC 3109, Sextans A, Sextans B and the Antila dwarf. According to newer works (van den Bergh, 2000) it is more likely that they form an isolated independent group. Table 1.1 lists some basic parameters of various Local Group members, as published by van den Bergh (2000). The information about the subgroup attribution from Mateo (1998) was added.

In addition, the Local Group contains a few isolated dwarf galaxies that cannot be attributed to one of the three subgroups, e.g. the recently discovered Cetus dwarf. Other isolated dwarf galaxies found near the Local Group may actually be members, but the distance measurements obtained so far do not allow a certain determination of their membership.

### 1.1.2 Membership to the Local Group

The factual membership of a galaxy can be determined by measuring the distance and/or the relative velocity of the prospective candidate. A galaxy is usually regarded as a member of the Local Group, if its distance from the barycenter is less than  $\sim 1500$  kpc or its radial velocity (corrected to a stationary center of mass) is less than  $50 - 100$  km s<sup>-1</sup> (e.g. Irwin, 1999).



Name	Alias	Type	Subgroup	$M_V$	$D_{MW}$ [Mpc]	$D_{LG}$ [Mpc]
WLM	DDO 221	Ir IV-V	LGC	-14.4	0.95	0.81
IC 10	UGC 192	Ir IV:	M31	-16.3	0.66	0.27
Cetus		dSph		-10.1	0.78	0.62
NGC 147	UGC 326	Sph	M31	-15.1	0.66	0.22
And III	A0032+36	dSph	M31	-10.2	0.76	0.31
NGC 185	UGC 396	Sph	M31	-15.6	0.66	0.22
NGC 205	M110	Sph	M31	-16.4	0.76	0.31
M32	NGC 221	E2	M31	-16.5	0.76	0.31
M31	NGC 224	Sb I-II	M31	-21.2	0.76	0.30
And I	A0043+37	dSph	M31	-11.8	0.81	0.36
SMC		Ir IV/IV-V	MW	-17.1	0.06	0.48
Sculptor		dSph	MW	-9.8	0.09	0.44
Pisces	LGS 3	dIr/dSph	M31	-10.4	0.81	0.42
IC 1613		Ir V	M31	-15.3	0.72	0.47
And V		dSph	M31	-9.1	0.81	0.37
And II		dSph	M31	-11.8	0.68	0.26
M33	NGC 598	Sc II-III	M31	-18.9	0.79	0.37
Milky Way		S(B)bc I-II	MW	-20.9	0.01	0.46
Phoenix		dIr/dSph	MW	-9.8	0.40	0.59
Fornax		dSph	MW	-13.1	0.14	0.45
LMC		Ir III-IV	MW	-18.5	0.05	0.48
Carina		dSph	MW	-9.4	0.10	0.51
Leo A	DDO 69	Ir V	MW	-11.5	0.69	0.88
Leo I	Regulus	dSph	MW	-11.9	0.25	0.61
Sextans		dSph	MW	-9.5	0.09	0.51
Leo II	DDO 93	dSph	MW	-10.1	0.21	0.57
Ursa Minor	DDO 199	dSph	MW	-8.9	0.06	0.43
Draco	DDO 208	dSph	MW	-8.6	0.08	0.43
Milky Way	Galaxy	S(B)bc I-II	MW	-20.9:	0.01	0.46
Sagittarius		dSph(t)	MW	-13.8	0.03	0.46
SagDIG		Ir V	LGC	-12.0	1.18	1.29
NGC 6822		Ir IV-V	LGC	-16.0	0.50	0.67
Aquarius	DDO 210	Ir V	LGC	-10.9	0.95	0.95
Tucanae		dSph	LGC	-9.6	0.87	1.10
Cassiopeia	And VII	dSph	M31	-12.0	0.69	0.29
Pegasus	DDO 216	Ir V	LGC	-12.3	0.76	0.44
Pegasus II	And VI	dSph	M31	-11.3	0.78	0.38

Table 1.1: Name, Hubble type, subgroup attribution, absolute  $V$ -band magnitude and distances to the Milky Way and the barycenter of the Local Group for the certain members of the Local Group. Data taken from Table 2 in [van den Bergh \(2000\)](#). The subgroup information was added using [Mateo \(1998\)](#). The acronyms used are MW for the Milky Way subgroup, M31 for the Andromeda subgroup, and LGC for the Local Group Cloud.

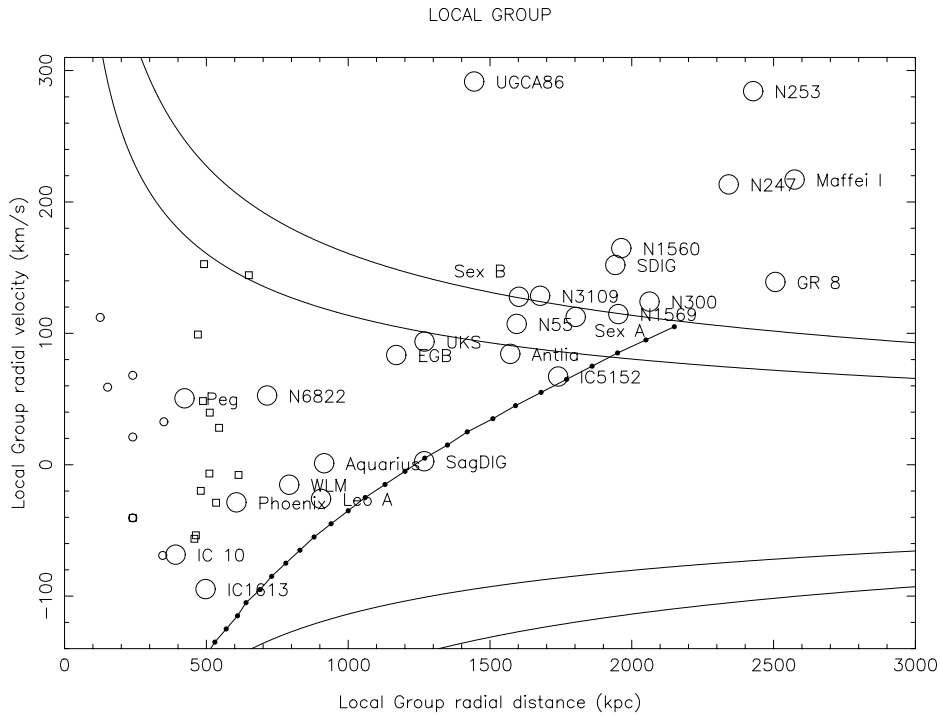


Figure 1.1: Radial velocity against distance from the barycenter of the Local Group, for members as well as nearby isolated galaxies. The upper and lower tracks show the Virial limits for Local Group masses of  $3 \times 10^{12}$  and  $4.5 \times 10^{12} M_{\odot}$  assuming pure radial motion. The knotted line shows a third membership criterion, the maximum distance an object could have traveled since the Big Bang. The small squares denote the members of the Milky Way subgroup, the small circles the members of the M31 subgroup. Their kinematics are specific to the dominant member, and cannot be used in this context. The graphic is reproduced from [Irwin \(1999\)](#).

### Distance measurements

To measure the distance to Local Group galaxies, various methods have been applied and documented in the literature. The most easily accessible is the measurement of the brightest blue and red giants, only requiring photometric measurement of a few bright stars. The largest source for error lies in the need for a clear identification of giants in the distant galaxy. A contamination by foreground stars or a blend of stars in the dwarf galaxy could lead to a severe misinterpretation of the distance. More robust methods are those based on well-understood physical processes, among them the period-luminosity relation of  $\delta$  Cephei variables, the magnitude of the tip of the red giant branch (TRGB) and the magnitude of the turnoff from the Main Sequence in the color-magnitude diagram.

Distances are often specified as the so called distance modulus, the logarithm of the

ratios of apparent and absolute brightness, defined as

$$m - M = 5 \log d - 5 \quad (1.1)$$

with the apparent magnitude  $m$ , the absolute magnitude  $M$  and the distance  $d$  measured in parsec (pc). The absolute magnitude is defined as the magnitude a lightsource would have if it were within 10 parsec distance from the observer.

The Cepheid distance measurement uses the relation between the period and the absolute average magnitude of the variable star (Leavitt & Pickering, 1912), for more recent discussions see, e.g. Madore & Freedman (1998) or Madore *et al.* (2000). The application of the method requires repeated observations stretched out over a sufficiently long timespan, preferably at least several weeks. The typical range of absolute magnitudes is  $-8.5$  to  $-3$ . The so derived distances can yield accuracies of 5 to 10% (Madore & Freedman, 1998).

The TRGB method requires sufficiently deep photometric data in the  $I$ -band and a second one to allow the calculation of colors of the stellar light, and following the identification of the red giant branch in the color magnitude diagram. The magnitude of the brightest stars populating the RGB (typically  $M_I = -4$  for low metallicity) can then be found in a histogram of the RGB. The distance is then derived using the absolute magnitude of the TRGB found in galactic globular clusters of similar metallicity (Lee *et al.*, 1993). Distance estimates obtained in this way are almost as good as those from the (young)  $\delta$  Cep stars.

For young systems with young stellar populations, the turn-off can be very bright ( $M_V = -5$ ) while for purely old dwarf galaxies it can be fainter than the sun ( $M_V = +5.5$ ). When applied to sufficiently deep data it can yield distances as accurate as the ones determined with the help of the  $\delta$  Cep and the TRGB method.

The same comparison technique is applied when using the turn-off from the Main Sequence. While this is probably the most stable and most versatile technique, allowing analysis of the stellar content as well, it is also one of the most observationally demanding ones. Its application needs very deep photometric measurements in at least two passbands with high resolution to circumvent crowding from neighboring stars.

### Velocity measurements

To measure the velocity, it would seem easiest to simply measure the proper motion of the galaxy corrected for the relative movement of the earth and the sun. Unfortunately even for satellites of the Galaxy the proper motion is too small to be measured in a simple way using galactic stars as reference. The reflex motion of the sun (Eddington, 1917) would completely dominate any signal stemming from the motion of the observed galaxy. Recently it has been possible to obtain direct proper motion measurements for a few members in the local group using distant galaxies as a reference frame.

Other methods to determine velocities are the analysis of the debris left behind by tidally disrupted galaxies as they move through the Local Group. The most common approach is the measurement of redshifts at the 21 cm line.

Fig. 1.1, reproduced from Irwin (1999), shows the location in the velocity distance plane for a number of certain Local Group members and nearby isolated systems. In addition the membership boundaries are plotted.

In general it should be obvious now that the confirmation of the membership to the Local Group of a given galaxy is a difficult task. But precise measurements of distances within the Local Group are of great importance. The distances of galaxies in the Local Group represent the first steps of the cosmic distance ladder, on which a lot of astronomical works - especially extragalactic works - rely. Membership classification helps to further determine the complete mass within the Local Group, which is relevant for analysis of the dark matter content therein.

### 1.1.3 A word on nomenclature

The nomenclature used in astronomy can often be rather confusing, and the zoo of different naming schemes used for dwarf galaxies is no exception. The most common forms are a mnemonic for the survey, and either a continuous index number or a position information. The mnemonics for the surveys used in this thesis are the Messier Catalog (e.g. M31), the DDO survey (van den Bergh, 1959), e.g. DDO 210, named after the David Dunlop Observatory, the EGB survey (Ellis *et al.*, 1984), e.g. EGB 0427+63, named after its creators, the ‘‘Catalog of Principal Galaxies’’ (Paturel *et al.*, 1989), e.g. PGC 003792 and the UGCA survey, the ‘‘Uppsala General Catalog Appendix’’ (Nilson, 1974).

## 1.2 Dwarf galaxies, your small stellar friend

When Hubble devised his tuning fork diagram, the Hubble Sequence (see Fig. 1.2), he believed that galaxies would start their evolution as elongated ellipticals, become spherical, build spiral arm structure and finally end up as irregular galaxies. Today, it has become accepted knowledge, that the evolution actually progresses the other way around, with (irregular) dwarf galaxies being the first building blocks.

The definition of dwarf galaxies is most unfortunately rather imprecise. In principle they cover the whole range from ‘‘normal galaxies’’ down to sizes comparable to the largest globular clusters.  $\omega$  Centauri, a globular cluster residing in the Milky Way with an approximate mass of  $5 \times 10^6$  solar masses ( $M_{\odot}$ ) has about the same mass as some dwarf galaxies. For this reason it is considered possible that it is actually not a globular cluster, but the remaining core of a dwarf galaxy, captured by the Milky Way.

The most common definition is by luminosity, classifying all galaxies with magnitudes below a fixed absolute magnitude in the V-Band (e.g.  $-18$  mag) as dwarf galax-

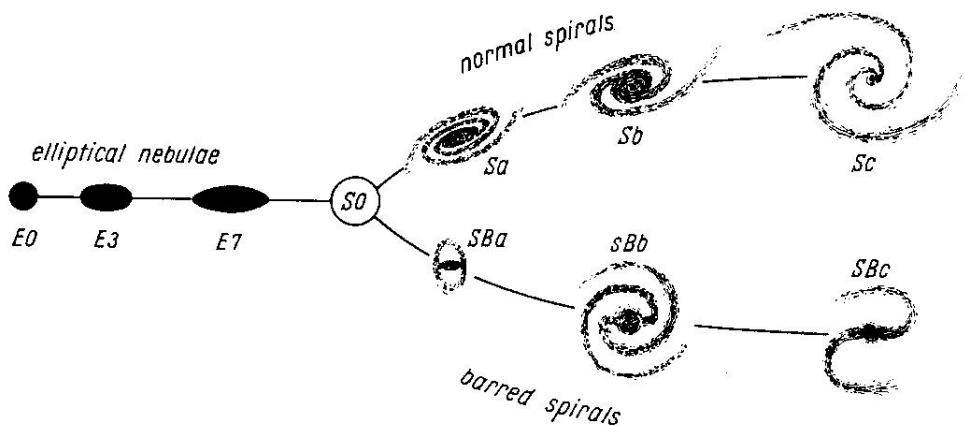


Figure 1.2: The tuning fork diagram of galaxy evolution as devised by [Hubble \(1936\)](#). He believed, that galaxies evolve from ellipticals to spirals and end as irregular dwarf galaxies.

ies. Dwarf galaxies show a wide range of mass-to-light ratios, so a classification by mass would seem more reliable, but the masses are unknown for most dwarf galaxies.

Like the normal galaxies dwarf galaxies are classified into different types by their morphology, i.e. their optical appearance. Dwarf galaxies are categorized into five groups: dwarf spiral galaxies, ellipticals, spheroidals, irregular galaxies and blue compact dwarf galaxies.

Dwarf irregular galaxies are, as the name suggests, irregular in shape and show a wide variety of different star formation histories and stellar populations. The Local Group contains several irregular dwarf galaxies. Many of them lack a precise distance measurement and an analysis of their star-formation history ([Mateo, 1998](#)).

The wide variety of dwarf galaxies in the Local Group might provide a way to shed some light on the relationship between dwarf irregulars and the other types of dwarf galaxies. There are some hints that very low mass dwarf irregulars might evolve into dwarf spheroidals ([Grebel, 2001](#)). [Van den Bergh \(1999\)](#) notes, that most dwarf irregular galaxies formed in the field, far from the larger galaxies, while the dwarf spheroidals in the Local Group formed in the potential wells of the larger spiral galaxies.

Dwarf galaxies provide us with unique astrophysical laboratories. They are usually very metal poor, thus they are still mostly composed of primordial material, i.e. matter that formed shortly after the big bang. The dwarf galaxies in the Local Group are close enough to study their stellar populations thoroughly and obtain detailed chemical abundances ([Mateo, 1998](#)).

Dwarf galaxies are by far the most numerous galaxies in the universe. Hierarchical models indicate that dwarf galaxies might have been the building blocks of the large galaxies we observe today (e.g. [Kauffmann & White, 1993](#); [Kauffmann \*et al.\*, 1993](#)).

Today numerous dwarf galaxies are known in nearby groups and clusters of galaxies, but the dwarf galaxies in the Local Group provide us with the richest and most diverse sample spanning a wide range of luminosities and masses (Mateo, 1998).

Another interesting point about dwarf galaxies is their connection to dark matter. They span a large range of masses, luminosities and mass-to-light ratios at the lower end of the mass scale of galaxies (Grebel, 2001).

## 1.3 Stellar evolution and stellar populations

Stars are the most commonly known and probably most thoroughly studied astronomical objects. Despite their often relatively complex composition, they can be regarded as simple gravitationally bound clumps of gas and plasma. The light they emit can tell us a lot about their internal physics. Its spectral composition tells us about the chemical composition of the stars as well as their environments. The spectral energy distribution can be used to draw conclusions on mass and temperature of the stars.

In the following an overview about stellar evolution and populations will be given. For a more thorough discussion the reader is referred to the works by Iben and Renzini (e.g. Iben, 1976; Iben & Renzini, 1981, 1983; Renzini & Fusi Pecci, 1988; Renzini & Buzzoni, 1986), or a textbook about stellar physics and evolution.

### 1.3.1 Stellar evolution

When plotting the luminosity of nearby stars against their effective temperatures, Henry Norris Russell and Ejnar Hertzsprung found independently that the stars do not fill up the whole plane smoothly, but seem to clump in specific parts. The so-called “Hertzsprung-Russell diagram” was discovered (e.g. Russell, 1933).

Fig. 1.3 shows a variation of the Hertzsprung-Russell diagram (HRD), the color-magnitude diagram. This adaption is more easily accessible using typical astronomical observation data. The absolute magnitude of a star is proportional to its luminosity, and its effective temperature can be approximated by its color (the magnitude difference between two spectrally distinct filter passbands) under the supposition, that the star radiates like a black body. For most cases the star could be considered to be hot and dense enough to approximate a black body. This assumption breaks down for cool stars where strong absorption of light by dust in the outer regions of the star can lead to significant reddening of the emitted light.

The structures found in the HRD can be explained by studying the evolution of a typical star. A star is born, when a cloud of gas contracts. During this contraction the density and temperature in the cloud increases, until the core of the protostar reaches a point hot and dense enough to set off the fusion of hydrogen into helium. The pressure of the heated gas stabilizes the contraction, and the star enters a stable phase on the Main Sequence (MS) shown in Fig. 1.3. Its position on the MS depends on the mass of

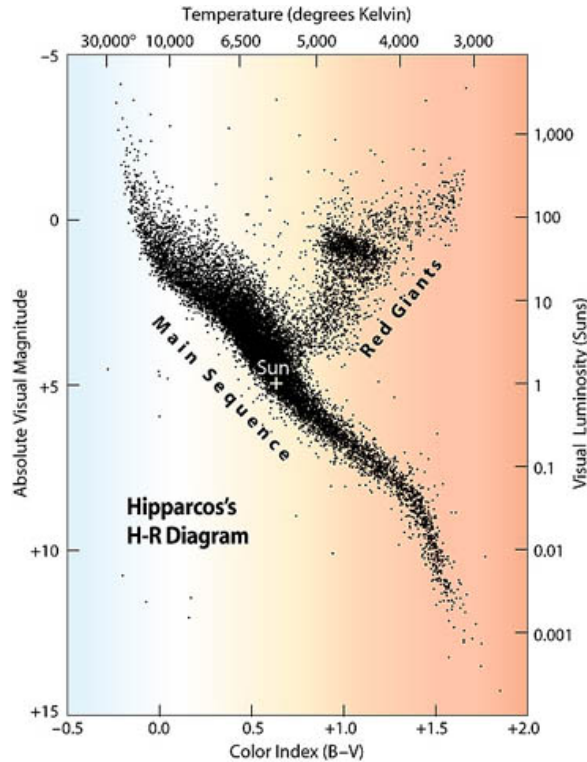


Figure 1.3: Color-magnitude diagram of nearby stars based on photometric data obtained by the Hipparcos astrometric satellite. Picture by [Perryman \*et al.\* \(1997\)](#)

the star, the more massive the hotter and more luminous the star will be. Its mass and temperature also decide about the further evolution of the star, the hotter, the faster it will use up its nuclear fuel.

After some time, ranging from  $10^7$  yrs for very massive stars to  $10^{11}$  yrs for the least massive ones, there is no hydrogen left in the core to maintain nuclear fusion. As the core contracts slowly, the region in which nuclear fusion occurs moves outward forming an hydrogen burning shell within in the star. During this phase the stars diameter will increase and the star moves up along the red giant branch (RGB).

At first the core continues to contract during this shell burning phase. When reaching the top of the RGB, the core of stars with masses  $M \lesssim 2.25 M_{\odot}$  the core silently starts to fuse helium into carbon. This leads to a second, much shorter, phase of tranquility. During this phase the star moves through the HRD on a so-called blue loop (see Fig. 1.4, as its luminosity and color changes with the energy production in the hydrogen shell. In less massive stars, the contracting core was stabilized by the development of an electron degeneracy. Reaching the tip of the red giant branch, the degeneracy is removed in a series of violent bursts of energy, the helium flashes. After these the star rests on the horizontal branch, visible as the clump of stars near the giant branch in Fig. 1.3, and denoted as “HB” in Fig. 1.4. For stars of low metallicity it is usually called the horizontal branch, for stars with high metallicity the red clump.



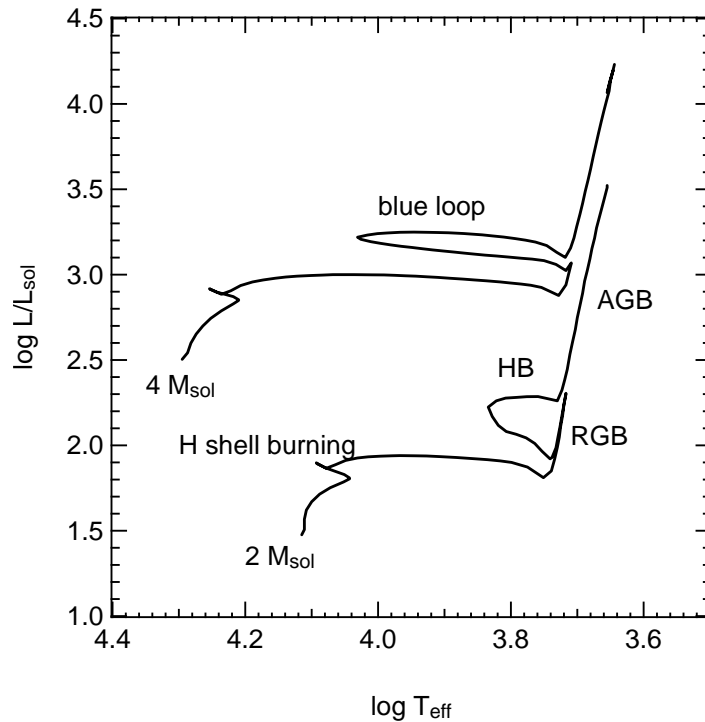


Figure 1.4: Evolutionary tracks from [Girardi \*et al.\* \(2000\)](#) for low metallicity ( $Z = 0.0004$ ) stars with two and four solar masses from the main sequence up to the asymptotic giant branch. Important evolutionary stages are noted on the low-mass track.

Once the helium in the core is depleted, the core starts contracting once more. The star's atmosphere cools and expands, moving upwards on the asymptotic giant branch (AGB), shown in Fig. 1.4. The helium once more in a shell can now reach a sufficient temperature to ignite fusion. This shell is thermally unstable. Due to its thin size, the shell cannot expand as the temperature increases with the onset of fusion. This leads to a further increase of temperature and fusion rate. This finally results in a rapid release of energy, a so-called thermal pulse. The AGB phase is often divided into two parts, the EAGB, the early AGB, the evolution up to the first thermal pulse, and the TPAGB, the thermally pulsing AGB.

A star on the AGB can go through several of these thermal pulses. In addition the stars can exhibit pulsating variations in their brightness (see Sec. 1.4). As the star cools, convective energy transport becomes more and more relevant, at the same time introducing significant mixing between the different layers of the star. The outer parts of the star cool so that abundant molecules (e.g. TiO) can form. This leads to an increase of dust in the outer regions of the star, resulting in a brightness decrease of several magnitudes in the optical part of the spectrum. During its AGB phase a star can lose a significant part of its initial mass due to strong stellar winds caused by radiation pressure on the dust particles. In some cases the formation of a gas shell surrounding the star can be observed.



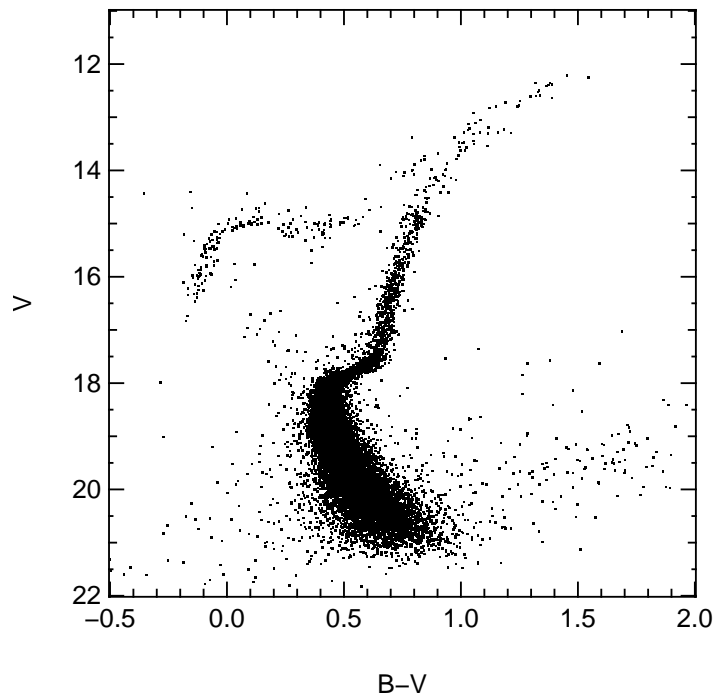


Figure 1.5: Color magnitude diagram for the globular cluster M5 from [Piotto \*et al.\* \(2002\)](#). Globular clusters provide an excellent example for simple stellar populations as all the stars in the cluster formed at the same time.

Once the He shell burning finally ceases, very massive stars can go through several similar cycles, burning ever more massive elements, up to iron, but these phases become increasingly shorter. At the end the remaining mass decides about the fate of the star. Sufficiently massive stars can explode in a supernova and end up as a neutron star, or a black hole. Less massive ones will blow away their outer shells and collapse to a white dwarf.

It should be noted that the theoretical simulation of stars during the AGB phase is a very difficult undertaking, as effects like the convective mixing of layers and the mass loss due to stellar winds have to be taken into account. A well defined sample of AGB stars could help to further our understanding of these late stages of stellar evolution.

### 1.3.2 Stellar populations

In the last section the evolution of a single star across the Hertzsprung-Russell diagram was explained. When studying the stellar content of galaxies, the evolution of whole stellar populations becomes relevant.

A simple stellar population (SSP) denotes a group of stars formed during a single burst of star formation. An example for such an SSP is a globular cluster, all stars therein formed at the same time, and evolved from thereon.

Fig. 1.5 shows the color-magnitude diagram for the globular cluster M5 from [Piotto \*et al.\* \(2002\)](#). It shows the main sequence up to the turn-off. In addition, both, the horizontal branch and the asymptotic giant branch are clearly distinguishable. As all stars in the cluster have approximately the same age, the more massive stars already stopped the hydrogen burning in their cores, and evolved away from the main sequence onto the well populated RGB.

A stellar population is characterized by three parameters: age, metallicity and initial mass function (IMF). The IMF describes the distribution of masses amongst the stars created during the burst. The role of the initial mass function is described in [Sec. 6.1](#). Metallicity is commonly specified as relations of the abundances of different elements, e.g. Fe/H, relative to solar metallicity. A second notation frequently used is the specification of the parameters (X,Y,Z) denoting the fractional abundances by weight of hydrogen, helium and sum of the other elements respectively. Throughout this thesis metallicities for stellar populations will be specified using the latter way.

## 1.4 Variable stars

The recorded observations of variable stars date back to 1596 when David Fabricius was the first to record the variability of  $\alpha$  Ceti, later named Mira (the wonderful) by Hevelius in 1662.

The variability in stars can come from different physical reasons, among others, occultations in binary stellar systems (eclipsing binaries), overflow of mass from one star to the other in close binary systems and pulsating stars showing intrinsic brightness variations. In the rest of this section only the last type will be discussed, as only this type is relevant for the work presented in this thesis.

For a theoretical treatment of stellar pulsation, the reader is referred to e.g. [Gautschy & Saio \(1995, 1996\)](#) and [Christensen-Dalsgaard & Dziembowski \(2000\)](#)

Fig. 1.6 shows a Hertzsprung-Russell diagram (HRD) with the regions where different types of variability occur. Looking at the diagram, it can be seen that several post-MS evolutionary stages show some form of pulsation. Many of these occur on very short time-scales and with small amplitudes. Some are only detectable in the stellar spectrum.

The pulsating variable stars most interesting in extragalactic astronomy are the RR Lyrae, the  $\delta$  Cephei stars, and the long period Mirae and semi regular variables SRA (generally referred to as long period variables, LPVs).

RR Lyrae stars are stars with masses below 0.75 solar masses ( $M_{\odot}$ ) that are lying on the horizontal branch burning helium at the core, show variations on a time-scale of 0.2 to 1.2 days and amplitudes smaller than 2 mag ([Becker, 1998](#); [Gautschy & Saio, 1996](#)). They can serve as tracers of a very old stellar population, as these low mass stars reach the horizontal branch only very late in the evolution of the population.

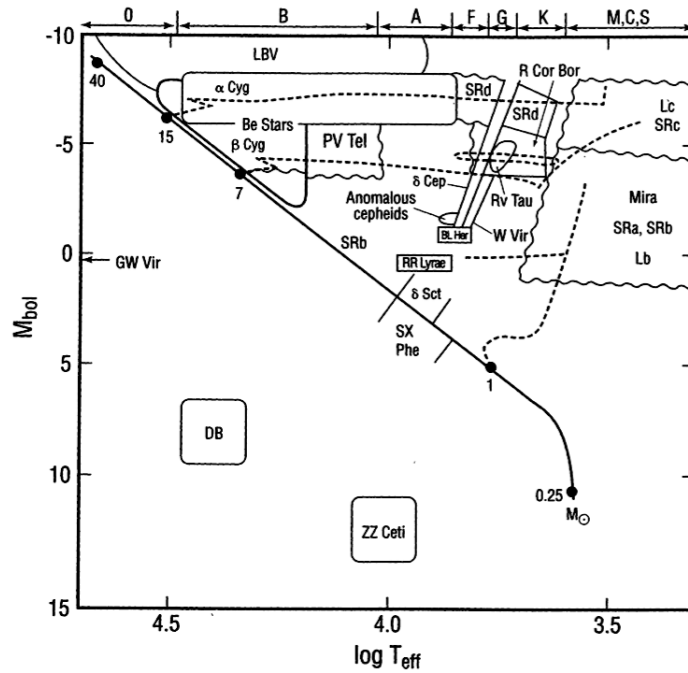


Figure 1.6: Positions of pulsating variable stars in the Hertzsprung-Russell diagram. The solid line shows the main sequence. The dashed lines represent the evolutionary tracks for stars with different initial masses. Graphic from [Becker \(1998\)](#)

$\delta$  Cephei stars are probably best known for their role as important distance indicators. They are typically stars with masses  $> 5 M_{\odot}$  and pulsate with periods between  $\sim 1$  and 135 days ([Becker, 1998](#); [Gautschy & Saio, 1996](#); [Groenewegen \*et al.\*, 2004](#)). They follow a strict relation between period and average absolute magnitude ([Madore & Freedman, 1998](#); [Madore \*et al.\*, 2000](#)) making them excellent distance indicators. From the period of the variable its mean absolute magnitude can be derived. The distance is then calculated from the difference between the absolute and the (measured) mean apparent magnitude.

These two types of variable stars lie on the so called instability strip, a relatively narrow region in the HRD. In Fig. 1.6 it runs from the the SX Phe stars upwards to the upper right, following the RR Lyrae and the  $\delta$  Cephei stars. The pulsation of all stars within this region is caused by the same reason, the  $\kappa$  mechanism. This mechanism rests on the fact, that in a compressed layer more energy is trapped by increasing opacity. The excessive energy can then drive large pulsations. This process is most efficient, when this driving layer is located within an ionization zone of the star, thus the form of the instability strip in the HRD.

On their way from the main sequence to the RGB, massive stars will cross the instability strip and show Cepheid behavior, but this phase is so short, that only few such stars can be observed. Most known Cepheids are in the loops massive stars exhibit in their post-MS evolution, while burning He in their core (see the blue loop for the

$4M_{\odot}$  track in Fig. 1.4). The tracks they follow through the HRD (see Fig. 1.4) lead them into the instability strip.

It should be noted in Fig. 1.6 that the realm of the long period variable Mira and SRa types lies to the right of the instability strip. Their pulsation cannot be explained by the  $\kappa$  mechanism alone.

Indeed, the reasons for the pulsation of the LPVs are not yet well understood. One explanation is a mechanism similar to the  $\kappa$  mechanism taking place in the He burning shells of a star on the TPAGB. Another theory explains the pulsation through the association and disassociation of TiO molecules in some parts of the star, changing the opacity in these layers leading to the brightness variations.

Any attempt of an explanation must be able to simultaneously explain the observed changes in radius that occur with the pulsations. The convective mixing of material between the different shells, the strong stellar winds and the influence of the strong dust absorption make it difficult to build a complete theoretical model of the mechanisms within such a star.

The long periodic variables are loosely classified in Mirae and semi-regular variables (SR), the latter ones subdivided into 4 subgroups, SRa to SRd. Mirae are defined as red giants with amplitudes larger than 2.5 magnitudes (Becker, 1998) and up to 6 or 8 mag and periods up to  $\sim 1000$  days. Mira itself shows an variation of  $\sim 6$  mag. The SRa still show relatively stable periods of up to 1200 days and a Mira-like behavior with amplitudes below 2.5 mag (Becker, 1998). The other semi-regular variables show no regular periodic variability.

The large amplitudes observed in the optical are caused by the increase of the opacity in the outer parts of the star due to large amounts of dust. The amplitudes in the near-infrared are much smaller ( $\sim 1$  mag). The darkening by the dust causes the star to shift to the right in the color-magnitude diagram, away from the AGB, as less light is absorbed at longer wavelengths.

The goal of this thesis is the search for LPVs of the Mira or SRa type. To find RR-Lyrae stars, the obtained data is generally too shallow. The Cepheid content is analyzed in the second work based on this data set, the thesis by Gössl (2006).

## 1.5 Outline of the thesis

This thesis is organized as follows. Chapter 2 details the selection of the candidate dwarf galaxies, the observational strategy and the data reduction. Chapter 3 describes the procedures used to obtain a photometric calibration for the reference images and compares the results obtained using two different approaches. The methods used to detect the variable sources and to establish the period solutions are outlined in Chapter 4, including the final catalog of variable stars. Chapter 5 lists procedures and results for the completeness simulations carried out to test the limits of the applied detection algorithms. Conclusions about the stellar content and star formation histories of the

analyzed dwarf galaxies is presented in Chapter 6, using both the obtained photometric data as well as the variable source catalog. In Chapter 7 the software developed for the control of the telescope on Mt. Wendelstein, developed for this thesis, is documented. The work and its major results are summarized in Chapter 8. The work concludes with an appendix listing the light-curves of the variable sources.



## Chapter 2

# Observations and data reduction

This chapter gives a motivation of the selection of candidate dwarf galaxies and the used selection criteria, the applied observing strategy and finally a summary of the reduction pipeline.

### 2.1 Object selection

For the VarStarDwarfs project a sample of Local Group irregular dwarf galaxies was selected for observation based on the data published in the compilation of Local Group dwarf galaxies by [Mateo \(1998\)](#). The applied selection criteria were:

- Evidence for young stars that might serve as indicators for the existence of a young or intermediate age stellar population. This criterion basically excluded dwarf ellipticals and dwarf spheroidals with their old populations, where one would expect to find primarily RR-Lyrae stars. Yet these would be too faint to be observed using the equipment available for the project.
- A celestial position that allows sufficient observations from Mt. Wendelstein, consequently no southern objects.
- Sufficient spacing in Right Ascension to avoid unwanted overlap of the individual observing campaigns,
- Sufficient distance from M31 to avoid collisions with the WeCAPP project ([Riffeser \*et al.\*, 2001](#)), the main concurrent project at the institutes observation site Mt. Wendelstein,
- A size of the object compatible with the field of view of the CCD camera on Mt. Wendelstein, and a brightness suitable for the typical observing conditions at the observatory.

Name	$\alpha_{2000}$	$\delta_{2000}$	d [Mpc]	$n_{\delta C}$	$n_{LPV}$
LGS 3	01:03:52.00	+21:53:06.0	$0.76 \pm 0.02$	2?	–
EGB 0427+63	04:32:01.00	+63:36:24.0	$1.3 \pm 0.7$	–	–
Leo A	09:59:26:46	+30:44:47.0	$0.69 \pm 0.1$	5?	–
GR 8	12:58:40.54	+14:13:02.2	$1.59 \pm 0.6$	1?	5?
DDO 210	20:46:51.90	-12:50:51.0	$0.8 \pm 0.25$	0	–
DDO 216	23:28:36.25	+14:44:34.5	$0.955 \pm 0.055$	7-10	–

Table 2.1: Parameters of the observed dwarf galaxies. Shown are the names as used in this work, commonly used alternative names are given in Table 2.2. The celestial coordinates for equinox J2000, their distance, and the number of known variable sources. Data taken from Mateo (1998) updated with newer more reliable data where appropriate, see Sec. 2.1.1 for the relevant references.

For dwarf galaxies matching these criteria first trial observations were obtained in 1999 to test the feasibility of the project. Finally six objects were selected for continued monitoring. Table 2.1 lists the coordinates, distances and number of known variables, Table 2.2 shows alternative names commonly used in the literature. The rejected galaxies, together with the reasons for the exclusion, are listed in Appendix A.

For most of these galaxies only few or no long period variables have been known so far. In most cases the given distances were obtained by analysis of observed color-magnitude diagram. Combined with the low numbers of known  $\delta$  Cep stars, it should be possible to support or improve the distance estimates using newly discovered Cepheids. The distance determination of said dwarf galaxies using  $\delta$  Cep stars is described in the work by Gössl (2006).

Up to now the observed data for four of the dwarf galaxies, Leo A, GR8, DDO 210 and DDO 216, have been reduced and analyzed. Only the results for these four galaxies are presented in this work.

### 2.1.1 The observed sample of galaxies

In the following is given a short overview over the literature concerning the observed dwarfs that is relevant to the work presented here. Fig. 2.1 gives an overview of the published distances.

#### LGS 3

The LGS 3 dwarf was discovered in a search for faint dwarf galaxies by Kowal *et al.* (1978). Schild (1980) used *R*-band data to obtain a total magnitude but derived no distance modulus. The distance was first determined by Christian & Tully (1983) putting the galaxy at a distance of 0.7 – 1.2 Mpc based on the magnitudes of red giants. Lee (1995) used the tip of the red giant branch (hereafter TRGB) from *VRI* photometry to



	Alternative names
LGS 3	PGC 003792, Pisces dwarf
EGB 0427+63	PGC 015439, UGCA 92
Leo A	PGC 028868, Leo III, UGC 05364, DDO 069
GR 8	PGC 044491, DDO 155
DDO 210	PGC 065367, Aquarius dwarf
DDO 216	PGC 071538, UGC 12613, Pegasus dwarf

Table 2.2: Alternative names of the observed dwarfs, often encountered in the literature. This list does not aim to be complete.

obtain a distance modulus of  $24.54 \pm 0.21$ , corresponding to a distance of  $0.81 \pm 0.080$  Mpc. [Tikhonov & Makarova \(1996\)](#) used *BVR* CCD photometry to derive a distance modulus of  $23.9 \pm 0.3$ , based on the magnitude of the tip of the red giant branch, positioning it a little closer. [Mould \(1997\)](#) studying its stellar populations found two populations, one with an age of  $10^8$  yrs and one with an age of  $10^{10}$  yrs. Furthermore he supported the distance estimate of [Lee \(1995\)](#) and found two candidates for  $\delta$  Cephei stars. In the same year [Aparicio \*et al.\* \(1997b\)](#) found similar result based on *VBI* data, deriving a distance of  $0.77 \pm 0.07$  Mpc or  $0.96 \pm 0.07$  Mpc depending on the assumed star formation history. Their data are consistent with star formation starting 12 – 15 Gyrs ago and a low metallicity of  $Z = 0.0007$  to  $Z = 0.002$ .

Using deep HST data [Miller \*et al.\* \(2001\)](#) were able to determine both distance and star formation history of LGS 3 at the same time. Using different indicators in the color-magnitude diagram they find a distance of  $0.62 \pm 0.02$  Mpc. Modeling the obtained color-magnitude diagram they received a star formation history dominated by a burst 13 – 15 Gyrs ago, and a relatively constant star formation from there on, a result similar to the findings by [Aparicio \*et al.\* \(1997b\)](#).

Most recently [McConnachie \*et al.\* \(2005\)](#) found a distance modulus of  $24.43 \pm 0.07$  corresponding to a distance of 0.769 Mpc based on the *I*-band magnitude of the TRGB.

### EGB0427+63

Little is known about the EGB 0427+63 dwarf galaxy, largely due to the strong extinction in its direction caused by its position within the plane of the Milky Way.

It was discovered by [Ellis \*et al.\* \(1984\)](#) as part of their planetary nebulae survey. [Hoessel \*et al.\* \(1988\)](#) were the first to study the system further, and found a distance modulus of at least 24.5, i.e. 0.8 Mpc, making it a likely member of the local group. [Karachentsev \*et al.\* \(1994\)](#) found a distance modulus of 26.72 (2.2 Gpc) based on photometry of red and blue supergiants. [Karachentsev \*et al.\* \(1997\)](#) obtained deeper data and corrected the distance modulus to 26.25 (1.8 Mpc) using the brightest red and blue giants as indicators.

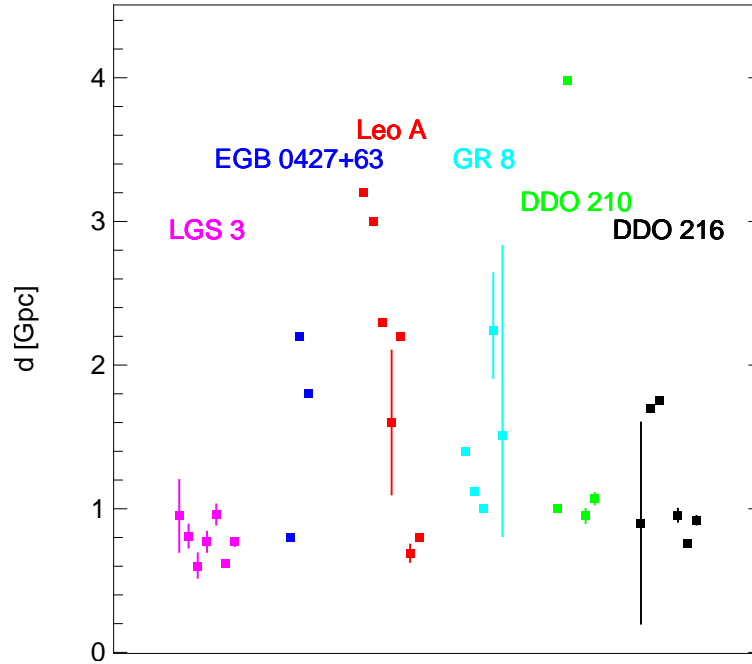


Figure 2.1: Distances to observed dwarf galaxies as published in the respective literature. Shown are the different measurements in Gpc. For the values without errorbars, no error estimate was given in the literature. See Sec. 2.1 for details.

### Leo A

Leo A is an isolated dwarf irregular galaxy. It is extremely gas-rich and exhibits a low stellar mass and metallicity.

Leo A was first mentioned as part of the DDO survey (van den Bergh, 1959, 1966). At first the actual membership of Leo A in the Local Group was uncertain, several works (de Vaucouleurs, 1975; Yahil *et al.*, 1977; de Vaucouleurs *et al.*, 1977) considered it to be part of the local group. Using planetary nebulae Jacoby & Lesser (1981) put an upper limit of the distance at 3.2 Mpc. Sandage & Tammann (1982) derived a distance of 3 Mpc based on the magnitudes of the brightest stars alone. Demers *et al.* (1984) were the first to obtain a calibrated color-magnitude diagram and found a distance of 2.3 Mpc. Sandage (1986) tried the same, and came up with a distance of  $1.6 \pm 0.5$  Mpc.

Hoessel *et al.* (1994) searched for  $\delta$  Cephei stars in Leo A. They found a distance of 2.2 Mpc based on four Cepheids, again questioning its membership to the local group. Tolstoy *et al.* (1998) used the Hubble Space Telescope to obtain deep photometric data, and derived a distance of  $0.69 \pm 0.06$  Mpc by analyzing the red clump. They also concluded that the Leo A is extremely metal-poor ( $Z=0.0004$ ) and predominantly young, but they could not exclude the presence of an old ( $> 10$  Gyr) population.

More recently, Schulte-Ladbeck *et al.* (2002), again using deep HST photometry

found a distance modulus of 24.5, i.e. 0.8 Mpc. They identified stars with extremely low metallicities and ages between 5 and 10 Gyrs. Their modeling of the color-magnitude diagram suggests a strong contribution (up to 50%) of an ancient (> 10 Gyr) population.

In a search for RR Lyrae stars [Dolphin \*et al.\* \(2002\)](#) independently found a distance modulus of 24.51 and evidence for an old (> 11 Gyr) population, the latter one based on the presence of RR Lyrae stars. The distribution they find suggests, that the old population of Leo A extends in a halo around the dominant young stellar population.

The presence of an old halo was supported by [Vansevičius \*et al.\* \(2004\)](#). Using wide-field imaging they found an extended old halo and a sharp stellar edge.

[Hopp \*et al.\* \(2006\)](#) searched Leo A for Cepheids, using the same dataset as described in this work and recovered several new Cepheids, further supporting the distance established by [Schulte-Ladbeck \*et al.\* \(2002\)](#) and [Dolphin \*et al.\* \(2002\)](#).

## GR 8

The GR 8 dwarf was first discovered by [Reaves \(1956\)](#) and like Leo A included in the DDO survey ([van den Bergh, 1959](#)). The blue colors observed by [Hodge \(1967\)](#) were a first indicator for a predominantly young dwarf galaxy. [Hoessel & Danielson \(1983\)](#) used photometric data to obtain a first distance modulus of 25.6 putting it at a distance of 1.4 Mpc at the edge of the local group. This was further supported by [de Vaucouleurs & Moss \(1983\)](#) deriving a distance of  $1.12 \pm 0.2$  Mpc and [Aparicio \*et al.\* \(1988\)](#) determining a distance modulus of 25.0

Using the first and so far only known Cepheid [Tolstoy \*et al.\* \(1995\)](#) derived a distance modulus of  $26.75 \pm 0.35$  placing it even further away at a distance of 2.24 Mpc beyond the borders of the Local Group. Using the first HST data [Dohm-Palmer \*et al.\* \(1998\)](#) found a TRGB distance modulus of 26.7 and adopted the distance modulus from [Tolstoy \*et al.\*](#) for their work. In the same year [Schulte-Ladbeck & Hopp \(1998\)](#) obtained a distance modulus of  $25.90 \pm 1.36$ , based on the magnitudes of the brightest blue and red giants, further supporting the other results.

## DDO 210

First discovered as part of the DDO survey ([van den Bergh, 1959](#)), the aquarius dwarf galaxy, DDO 210, was generally regarded to be a member of the local group, with a distance modulus of 25 (1 Mpc) set arbitrarily based on similarities with other members of the local group.

[Marconi \*et al.\* \(1990\)](#) obtained photometry for a color-magnitude diagram, but came to no definitive conclusion concerning the stellar populations found therein due to a strong contamination by fore- and background stars. Their findings point either towards a population of stars older than 1 Gyr or a young stellar content as young as

a few Myrs that would be affected by unusually strong reddening, given its celestial position. [Greggio \*et al.\* \(1993\)](#) modeled their observed color-magnitude diagram using synthetic data, and found that to be able to fully explain the observed diagrams they could not support the previously adopted distance modulus of 25, but suggested one of 28 ( $\sim 4$  Mpc), placing it significantly further away. The star formation history they derived is relatively constant over the last billion years, without significant bursts.

The open question regarding the membership of DDO 210 was finally solved by [Lee \*et al.\* \(1999\)](#) deriving a distance modulus of  $24.89 \pm 0.11$  corresponding to a distance of  $0.95 \pm 0.05$  Mpc. Further studying their color-magnitude diagrams, they derive a constant star formation history over most of the past with an increase in recent times.

Lately DDO 210 was revisited by [McConnachie \*et al.\* \(2005\)](#) again obtaining optical photometry for a color-magnitude diagram. They revised the distance modulus to  $25.15 \pm 0.08$  and the distance to  $1.071 \pm 0.039$  Mpc and find a metallicity of  $Z = 0.0003$ .

## DDO 216

The pegasus dwarf DDO 216 was discovered by [Holmberg \(1958\)](#) and included in the DDO survey ([van den Bergh, 1959](#)). A first estimate of its distance was obtained by [Jacoby & Lesser \(1981\)](#) in their survey for planetary nebulae. They specified an upper limit of its distance as  $6.4 \pm 1.2$  Mpc, and an estimate of  $0.2 - 1.6$  Mpc. The situation improved when [Hoessel & Mould \(1982\)](#) found a candidate for the TRGB in their color magnitude diagrams, with a corresponding distance of 1.7 Mpc. [Hoessel \*et al.\* \(1990\)](#) further supported these results with a determination of a distance modulus of  $26.22 \pm 0.2$  (1.75 Mpc) based on Cepheids, putting the dwarf at the edge of the local group.

These results were disputed by [Aparicio \(1994\)](#) deriving a distance modulus of  $24.9 \pm 0.1$  (0.95 Mpc) based on a clear identification of the TRGB. Studying the stellar content based on color-magnitude diagrams, [Aparicio & Gallart \(1995\)](#) proclaimed a significant old ( $> 10$  Gyr) population and a metallicity as low as  $Z = 0.008$ .

Revisiting the problem, [Aparicio \*et al.\* \(1997a\)](#) improved the results and found the oldest stars with an age of approximately 15 Gyrs, and several bursts of star formation in recent epochs. In addition they lowered the estimate of the metallicity to  $Z = 0.002$ . [Gallagher \*et al.\* \(1998\)](#) used HST imaging data to obtain a well-resolved color-magnitude diagram. The model with the youngest population they found to be compatible with the observed data contains stars with a metallicity of  $Z = 0.001$  formed mostly 2 – 4 Gyrs ago, but they can accommodate stellar ages of up to  $\sim 8$  Gyrs. Fitting self-consistent stellar population models they derived a distance of 0.76 Mpc.

Recently [McConnachie \*et al.\* \(2005\)](#) obtained a new distance estimate of  $0.919 \pm 0.03$  Mpc based on the TRGB in their optical photometry data, corresponding to a distance modulus of  $24.82 \pm 0.07$ .

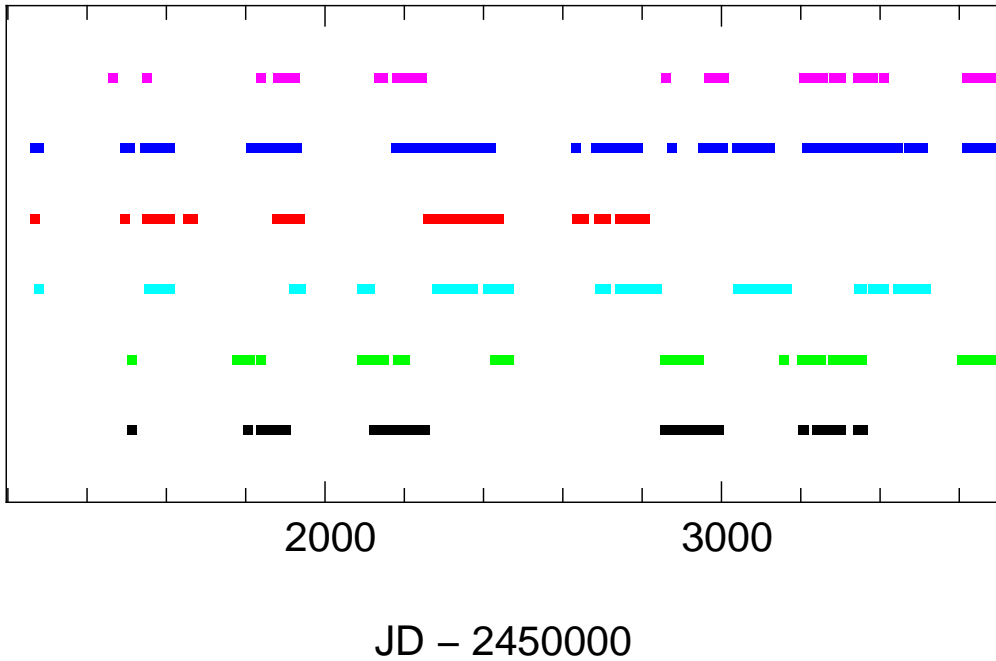


Figure 2.2: Timespand and spacing of the observations for the observed dwarf galaxies. Shown are the Julian Dates of the dates of observation for LGS 3 (magenta), EGB 0427+63 (blue), Leo A (red), GR 8 (cyan), DDO 210 (green) and DDO 216 (black).

## 2.2 Observing strategy

The observations for this project were conducted at the Ludwig Maximilians Universität's observatory on Mt. Wendelstein and with the on 1.23m telescope on Calar Alto in Spain.

### 2.2.1 The Wendelstein observations

The observations of the selected galaxies started in 1999 with early test observations, and are still continued, to further improve the timebase and thus the sampling of the light-curves.

The bulk of the observations were carried out at the 80cm telescope on Mt. Wendelstein. The fact that this telescope is at the institute's full disposal was a major driving factor behind the inauguration of the project in the first place. The observing conditions at the Wendelstein observatory usually provide excellent seeing ( $< 1''$ ) and  $\sim 130$  clear nights a year. The observations usually can not take full advantage of these conditions, but a seeing quality in the range of  $\sim 1''$  to  $\sim 1.5''$  is not unusual (Riffeser *et al.*, 2001). Despite these excellent conditions real photometric nights are very rare. The photometric stability is usually sufficient to derive relative photometry within the image, but

not to obtain absolute photometry using standard stars. This further supports a project in need of well resolved but not necessarily absolutely photometric observations.

The telescope is equipped with a  $1k \times 1k$  CCD camera with a field of view of  $8.5' \times 8.5'$ . As said above, this was one of the selection criteria applied. Due to the poor combination of the low resolution of the camera with the good seeing at the site, usually leading to undersampling in the images, work on a new camera was started. That new two-channel CCD camera to be commissioned in 2006 should greatly improve the efficiency for monitoring programs. See the work by Gössl (2006) for more details on the design and construction of the new camera.

In the years 2000 to 2003 the galaxies were observed every night visibility and weather conditions permitting and if there were no collisions with other observing campaigns. A typical observation consisted of 10 to 30 three minute observations to avoid saturation of bright stars in the image. Whenever possible the observations were done in the “Roeser-R2” filter available at the observatory. It is a broad-band filter comparable to the Johnson-*R* filter. When the conditions allowed additional observations were made using the Roeser *BV* Filter. This is a very broad filter covering approximately both the Johnson-*B* and *V* filters. Test observations using the Johnson *I*-Band filter proved to be too inefficient. In addition flat-field images in the used filters were taken at the beginning and at the end of the night

After this main observing run the frequency of the observations was reduced to once per month to further stabilize the obtained period solutions for the detected variables by adding more datapoints on a larger timebase. These data obtained after 2003 are not included in the analysis for the DDO 216 and GR 8 dwarf galaxies. The low number of additional epochs, and their little contribution to the final results compared with the work needed to reduce them made it an inefficient undertaking to add them to the project at this stage. In case of Leo A the additional data was only used to improve the period determination.

The maximum periods of the variables searched in this survey (Mirae and SRA) are below 1500 days (see Sec. 1.4, thus a limitation imposed by the length of the observations should have negligible impact.

### 2.2.2 The Calar Alto observations

During three observing runs in 2002 each spanning about two weeks additional data was acquired at the 1.23m telescope on Calar Alto. All three runs took place in spring, so data was only obtained for the Leo A, UGCA 92, DDO 210 and GR 8 dwarf galaxies.

The driving goal behind these observations was the assembly of densely sampled datablocks that can be used to securely identify the correct period especially for relatively short period variables like Cepheids. The observations in additional filters to the *R*-Band provide color information that can be used to confirm variables by their position in a color-magnitude diagram.

object	span [yrs]	WST		CA		
		BV	R	B	R	I
LGS 3	6.1	3	47	–	–	–
UGCA 92	6.6	40	182	14	48	29
Leo A	4.22 (6.6)	31	94 (43)	13	47	29
GR8	6.1	20	106	14	49	33
DDO 210	6.0	10	88	3	10	2
DDO 216	5.1	12	68	–	–	–

Table 2.3: Observations obtained for the candidate dwarf galaxies in the different filters. Shown are the span of the observations in years and the number of epochs in each filter for the two observing sites. The values in parenthesis for Leo A are the additional epochs only used for period determination.

The observation of a documented standard star field (Flaccomio *et al.*, 1999) during a photometric night furthermore provided a means to obtain an independent standard star calibration for four of the observed fields.

The images obtained with the available  $2k \times 2k$  CCD camera have a larger field of view but the same resolution as the ones observed on Wendelstein. This greatly simplifies the matching of the different observations. The variable source detection is done solely on the Wendelstein data, so the increased field remains unused. The observations were carried out in the Johnson *B*, *R* and *I* filters. A typical observation consisted of up to 30 individual images each with five minute exposure time (100s for Leo A, this was needed to avoid excessive saturation of a bright star in the field of view). Weather permitting, flat fields were observed in the evening and morning twilight. In addition a set of bias frames was taken each day to allow the bias correction using an averaged masterbias taken on the respective day.

Table 2.3 lists the number of epochs that were observed in the different filters used. In addition the maximum timespan covered by the observations is listed. Fig. 2.2 shows the Julian dates of the observations, illustrating the span and spacing of the individual observing blocks.

## 2.3 Data reduction

The observed data were reduced using the image reduction pipeline developed by Gössl & Riffeser (2002, 2003). In this section a summary of the procedure is given. For a more detailed description see the work by Gössl (2006). Gössl & Riffeser (2002, 2003) give an exhaustive discussion of the motivation and techniques used in this specific pipeline.

The most prominent feature of the reduction applied here is the propagation of the individual pixel error throughout the complete reduction.

### 2.3.1 The standard reduction

This subsection describes the different steps used in the reduction of the raw data up to the final stacked image for one night.

#### Bad-Pixel and bias correction

In the very first step saturated pixels and known pixel defects are masked. The saturated pixels are flagged in the error frame, the pixel defects are corrected by a linear approximation of the nearest neighbors after the cosmic-ray rejection.

For the Wendelstein data, the bias level was derived from the overscan and subtracted from the individual images. For the Calar Alto data a masterbias frame was constructed for each night, and this subtracted from the separate observations. This approach is unsuitable for the data obtained on Wendelstein. The bias patterns are highly unstable even on short timescales, due to strong interference caused by a nearby radio station.

#### Creation of initial error frame

Using the photon noise, the bias noise and the uncertainty of the bias determination an initial error estimate is calculated for each pixel in every observed image. These data are written into a new image, the corresponding error frame. All through the rest of the pipeline these errors frames are modified using Gaussian error propagation.

#### Flatfield calibration and cosmic-ray rejection

The flatfields observed during twilight time are combined into a flatfield with a high signal-to-noise ratio (see [Gössl \(2006\)](#) or [Gössl & Riffeser \(2002\)](#) for more details). The observed images are divided by the resulting flatfield, to eliminate side-effects introduced by pixel to pixel variations in the sensitivity of the CCD detector, intrinsic characteristics of the telescope optics or simply dust in the lightpath.

The so called cosmic-rays, or cosmics, are the results of particle events. These could either be cosmic-rays (or the radiation they create upon impact in the higher atmosphere) or the radiation caused by nuclear decay in the CCD chip itself. These particle events appear as single pixels or little streaks with relatively high counts. Finding and removing them is tricky, especially if several pixels are affected or the cosmic lies on-top of a real source.

The cosmic-rays were detected by fitting a five-parameter Gaussian against each local maximum found in the image. Where the resulting parameters fall within given thresholds, the peak is replaced by an individually fitted surface constant. For a more thorough description again see [Gössl \(2006\)](#) or [Gössl & Riffeser \(2002\)](#).



### Astrometric alignment and coaddition

The data produced by the instruments at the two sites are similar enough and show no significant field distortions, so that a linear translation between the different images is sufficient. To determine the necessary coordinate transformations a sample of well resolved stars was selected in the reference frame, and a single reference star manually identified in each frame observed during a given night. This reference star was used to find an initial offset, based on that the reference stars could be detected in the individual images, and the respective transformations be calculated. Using these transformation, the images were shifted in a flux- and point-spread function (PSF) preserving way onto the reference frame. The PSF describes how the light from a point-source (the star) is distributed over the seeing disk as a result from distortions in the atmosphere and the diffraction within the telescope.

The well-aligned images were summed up in a final step, each weighted by its individual errors, to produce a signal-to-noise optimized stacked image. See [Gössl \(2006\)](#) for more details.

#### 2.3.2 Reference frame creation

The coadded images from the nights with the best seeing and the highest signal were combined into a deep reference image for the difference imaging. Also serving as the photometric reference, an astrometric solution, a so called world coordinate system (WCS) and catalog with photometry of resolved stars were created.

To obtain the solution for the WCS, bright isolated stars were matched against the USNO catalog ([Monet, 1996, 1998](#)). These allowed the calculation of a transformation between the pixel-grid of the images and the actual celestial coordinates.

The detection of resolved stellar sources was done using DAOPHOT ([Stetson, 1987](#)). The main problem in the detection and photometry of stellar sources in galaxies is that the stars lie so close to one another in the observed images that they overlap each other. The normal approach would be aperture photometry, counting the flux within an aperture, and subtracting the contribution of the sky measured in a surrounding annulus. But on these sources this attempt is clearly prone to fail as the neighboring stars would contaminate both the flux from the star and the sky measurement.

In these cases a photometry package for crowded field photometry like DAOPHOT must be used. DAOPHOT individually fits the observed profiles with a semi-empirical PSF trained by isolated stars and eliminates the contamination by multiple deconvolution.

The resulting source catalog was photometrically calibrated (see Sec. 3) and served as a photometric reference for the light-curves of the variable stars as well as a source for conclusions about the stellar populations of the dwarf galaxies (see Sec. 6).

### 2.3.3 The difference imaging

To find sources with brightness variations between the different recorded epochs, an implementation of the Difference Image Analysis (DIA) algorithm (Tomaney & Crotts, 1996) was applied. The driving thought behind it being that variability can easily be detected by subtracting images from different epochs from a common reference frame as long as these images are geometrically and photometrically aligned to the reference frame. The resulting difference frame should be flat containing only noise, and the variable objects as positive or negative sources.

With the images already astrometrically aligned (see above) the exact matching of the PSF of the individual images remains an important factor. To accomplish this an implementation of the Optimal Image Subtraction (OIA) algorithm (Alard & Lupton, 1998) was used. The difference images were created by photometrically aligning the images against the reference frame. This is done by multiplying each image with an individual factor so that the fluxes of a set of stars in the individual image match the fluxes of the same stars in the reference frame. After that the PSF of the individual images is matched with the PSF of the reference image and the so prepared images subtracted from the reference frame.

In a final step the resulting difference images were convolved with a stellar PSF. This improves the detection of the variable sources, as they are more clearly distinguishable from the background noise.

The detection of the variable sources in the difference images is described in detail in Chapter 4.

## Chapter 3

# Photometric calibration

### 3.1 Why the effort?

The most fundamental parameters of an astronomical object that we can obtain are its position relative to other objects and the amount of emitted energy visible. The latter one can be measured using photomultipliers or CCD chips. In either case one obtains a quantity corresponding to the number of collected photons. This energy flux  $f$  is commonly converted into a logarithmic quantity, the magnitude  $m$ , defined as

$$m = -2.5 \times \log(f) + c \quad (3.1)$$

with a constant  $c$  defined by convention.

Unfortunately the observed magnitude is highly dependent on the circumstances of the observation, the detector used, the general transparency of the atmosphere at the site, and of course the weather conditions. In addition it varies with the height above the horizon as the amount of air that the light from the object travels through changes.

The effect of the atmosphere can be approximated as a plane parallel layer above the observatory. The light above the atmosphere  $I_{\nu,0}$  and the observed light  $I_{\nu}$  at a frequency  $\nu$  are then

$$I_{\nu} = I_{\nu,0} e^{-\tau_{\nu} \sec(z)} \quad (3.2)$$

with the optical thickness  $\tau_{\nu}$  and the zenith distance  $z$ . As  $\tau_{\nu}$  is generally not known,  $I_{\nu,0}$  is commonly approximated using measurements at different airmasses  $am$ , defined as:

$$am = \sec(z) \quad (3.3)$$

to extrapolate to airmass zero. The so obtained flux above the earth's atmosphere allows the comparison of observations obtained at different airmasses or from observatories with differing atmospheric transparency. The numerical factor needed for the extrapolation is defined as the extinction coefficient  $e$ .

$$m_0 = m + e \times am \quad (3.4)$$

with the magnitude of the object at airmass zero  $m_0$ . The extinction coefficient can be derived rather easily using observations of the same stars at different airmasses  $am_1$  and  $am_2$  and comparing the observed magnitudes  $m_1$  and  $m_2$ .

$$e = \frac{m_1 - m_2}{am_2 - am_1} \quad (3.5)$$

To compare the observations between different nights and data published in the literature, the observed magnitudes have to be corrected for these effects and translated into the standard magnitude system. In order to obtain such a calibration, standard stars with well-known magnitudes are observed several times during the night at different airmasses. The repetition of the observations is used to check the stability of the atmospheric conditions during the course of the observations and to obtain the extinction coefficient as shown above. The observed images are reduced in the same way as the science frames, normalized to one second exposure time and used to measure the instrumental magnitudes of the standard stars.

The thus obtained magnitudes  $m'$  are extinction corrected and can then be fitted against the standard magnitudes  $m$  with the magnitude zeropoint  $zp$  as

$$m = m' + zp \quad (3.6)$$

Equation (3.6) implicitly assumes that the calibration observations are obtained using the filters with the same transmission curves and CCD detectors with similar efficiencies as those used for the measurement of the standard magnitude. Often the used filters differ slightly in the exact shape of the transmission curve, even though the central wavelength and band width are the same. Such differences can, combined with the different colors of the standard stars utilized, lead to a color dependent deviation between the obtained and the actual magnitudes. To circumvent this problem, standard observations in additional filters can be applied to correct for these errors. First the color-term  $col_{std}$  and zeropoint  $zp_{std}$  are derived by fitting the standard color  $(m - m_1)$  between the primary magnitude  $m$  and the secondary magnitude  $m_1$  against the observed color  $(m' - m'_1)$

$$(m' - m'_1) = col_{std} (m - m_1) + zp_{std} \quad (3.7)$$

Using these parameters, the tabulated standard colors  $(m - m_1)$  can be translated into the observation system leading to the corresponding instrumental color  $(m - m_1)'$ . The observed magnitudes  $m'$ , the standard magnitude  $m$  and the transformed standard color  $(m - m_1)'$  are fitted with the zeropoint  $zp$  and the color-term  $col$  using a least squares fit.

$$m = m' + zp + col \cdot (m - m_1)' \quad (3.8)$$

In the unfortunate case that no standard star observations were obtained, published zeropoints of the observed field can be applied to calibrate stars as so called secondary standards and use these to obtain a zeropoint for the observations.

The atmospheric conditions on Mt. Wendelstein are only seldomly stable enough to allow precise photometric calibrations. As a consequence published calibrated catalogs of stars obtained through Hubble Space Telescope (HST) observations in the field of view of the dwarf galaxies were used as secondary standards. In addition to these, standard star observations were obtained during three photometric nights on Calar Alto. For the dwarf galaxies observed during these nights, the Calar Alto calibration serves as an independent comparison of the HST calibration. Unfortunately, not all dwarf galaxies were observable during these nights at Calar Alto. For these the HST calibration is applied.

### 3.2 Calibration using HST photometry

As laid out in the previous section, photometric calibrations using terrestrial telescopes are often limited by the occurrence of sufficiently stable conditions during the allocated observing time. The Hubble Space Telescope (HST), on its low orbit around earth is not affected by the contrarious effects of the atmosphere. Thus it provides a relatively stable and well-understood observational platform that can be calibrated absolutely.

Holtzman *et al.* (2003) used publicly available HST observations to create a catalog of stars for the galaxies in the local group. They calibrated these stars in the Johnson-Cousins *UBVRI* magnitude system using the cookbook provided by Holtzman *et al.* (1995). Depending on the availability of suitable observations, they provide calibrated catalogs for at least the *F555W* and *F814W* passbands and in some cases also for *F439W*, corresponding to the Johnson *V*, *I* and *B* filters. These catalogs served as secondary standards to deduce the zeropoint of the reference frames and subsequently of the light curves of the detected variable stars.

In the reference frames, catalogs of positions and instrumental magnitudes were created using DAOPHOT (Stetson, 1987, see Sec. 2.3.2 for a description of DAOPHOT). The stars from the DAOPHOT catalog were matched against the stars from the HST observations using their celestial coordinates, allowing a maximum distance of 2". In case of the Pegasus (DDO 216), the GR 8 and the DDO 210 dwarf galaxy the celestial coordinates supplied for the catalog were not accurate enough to allow a reliable match, so a direct transformation between the pixel coordinates of both observations was obtained. The transformed pixel coordinates were then matched with an accuracy better than 0.7 pixels. The greatest obstacle when using HST observations for the calibration of ground-based observations is its excellent optical performance. Unaffected by the atmosphere the imaging of the HST is diffraction-limited. In a rather dense stellar field like the observed dwarf galaxies, several stars resolved by the HST are smeared together into one PSF in the ground based observations. To avoid mismatching only stars from the ground-based observation with just one counterpart in the HST observation within a radius corresponding to the radius of the ground-based PSF were used for the calibration.

To address the lack of *R*-band observation from the HST we transformed the *V*-band magnitudes and *V - I* colors into Cousins *R*-band magnitudes using the color

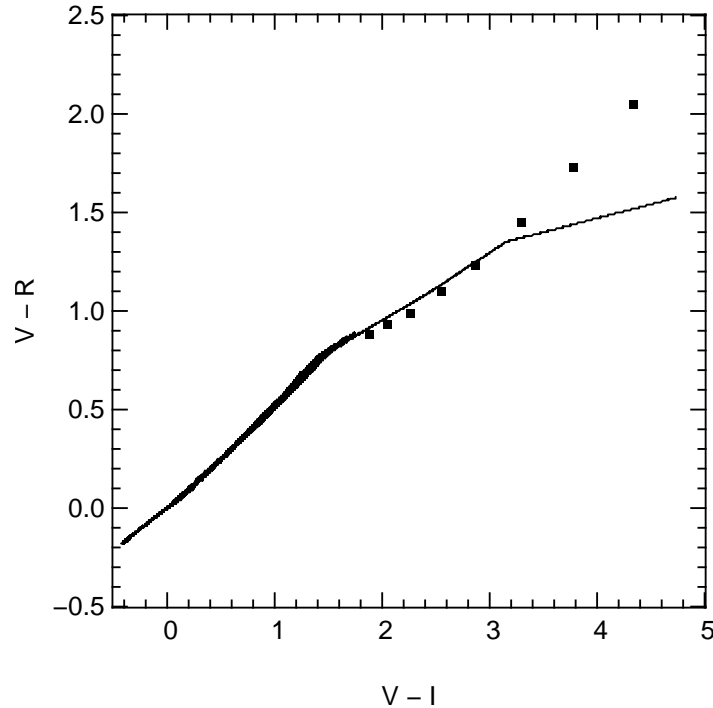


Figure 3.1:  $V - I$  versus  $V - R$  colors for the Bertelli *et al.* (1994) isochrones computed for different metallicities (lines) and the empirical data points from Thé *et al.* (1990)

transformation tables published by Thé *et al.* (1990). This transformation is only valid for stars with  $1 \leq V - I \leq 3$ , so we only selected stars from the HST data with colors in this range. The tables published by Thé *et al.* were derived from stars of solar metallicity. We used the Bertelli *et al.* (1994) isochrones to verify that the empirical data of Thé *et al.* perfectly agree with the theoretical predictions and that any dependence of the transformation on metallicity is marginal (Fig. 3.1).

This method was, where available, applied to both reference frames – Wendelstein and Calar Alto – and the results compared. Using the acquired zeropoints the DAOPHOT output source lists were calibrated and the object positions matched. The overall good agreement serves as a first indicator for the validity of the chosen approach. As an example the results for the Wendelstein (WST) and Calar Alto (CA)  $R$ -Bands are shown in Fig. 3.2. The results of the calibrations are listed in Table 3.1.

### 3.3 Calibration using observed standard stars

During three nights with sufficiently stable conditions on Calar Alto in March 2002 we obtained photometric measurements of the open star cluster NGC 2264. Flaccomio *et al.* (1999) published  $BVRI$  photometry in the Johnson-Cousins system for numerous stars in this field. Our observations were carried out in the  $B$ ,  $R$  and  $I$  filter

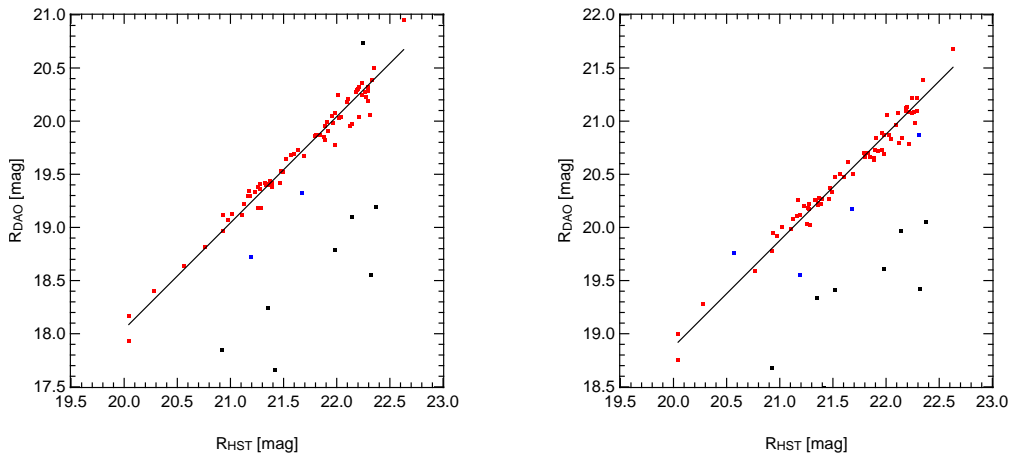


Figure 3.2: Zero-point fit for the Leo A  $R$ -Band against the photometry published by Holtzman *et al.* (2003). The left panel shows the Wendelstein observations, the right the Calar Alto data. In each case the instrumental magnitude is plotted against the published one, the solid line shows the best fit. The black points were rejected during the recursive fitting due to a too large deviation from the best fit.

Galaxy	$B$	$R_{WST}$	$R_{CA}$	$I$
Leo A	2.274	1.958	1.121	2.598
DDO 216	—	1.782	—	—
GR 8	3.003	1.839	3.192	2.765
DDO 210	—	4.391	4.006	4.354

Table 3.1: Zero-points obtained for the calibration using the calibrated photometry published by Holtzman *et al.* (2003). The typical standard deviation of the fit is in the order of 0.02 mag. The results shown are for the Calar Alto (CA)  $B$ ,  $R$  and  $I$ -band and the Wendelstein (WST)  $R$ -band.

and repeated two or three times with varying airmass of the observed field during each night. Comparison of the magnitudes in the different observations showed that the night of the 21st March was photometrically most stable.

The images were reduced applying the same techniques as to the science observations, see Sec. 2.3 for details. The final reduced images were registered to a common frame of reference. For the cross-identification with the tabulated standard stars a World Coordinate System solution (see Sec. 2.3.2) was constructed. In a final step stellar objects were detected.

The object fluxes were measured applying aperture photometry with a curve-of-growth method. For this procedure, the flux of each star is measured within a given radius and the background is subtracted using an annulus outside the measurement radius. This is repeated several times with increasing radii. The measured fluxes are plotted as a function of radius and the optimal radius for the photometric measurement can be obtained. At the same time adverse effects caused e.g. by blending with nearby

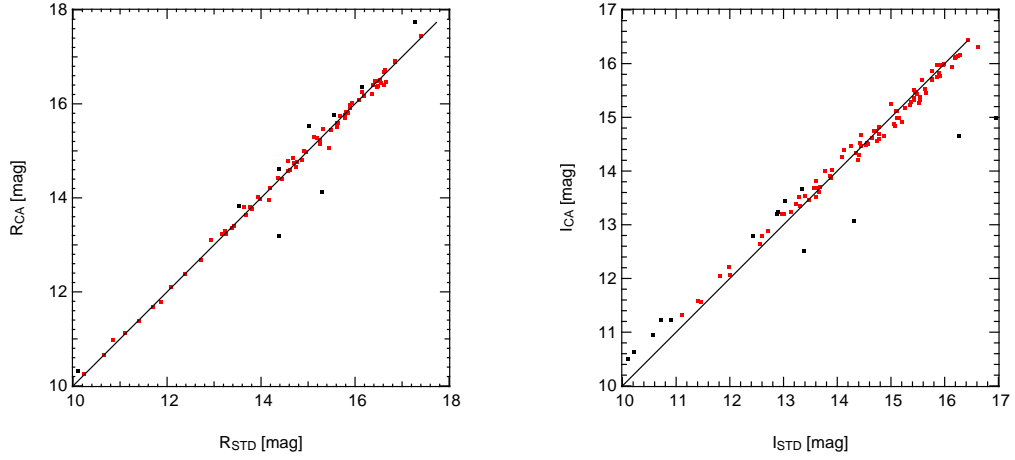


Figure 3.3: Examples for the zero-point fit of the observed standard star magnitudes in NGC 2264 against the values published by [Flaccomio \*et al.\* \(1999\)](#). The left panel shows the *R*-Band, the right one the *I*-Band, the red points contributed to the final fit, the black ones were rejected by sigma-clipping. The difference in the slope between the observations and the fit for the *I*-Band data stems from the different filters used and shows the need for a calibration with a color-term.

stars can be eliminated. The use of this technique is rather time-consuming and only feasible in fields where crowding is not a problem. In fields that are prone to stellar crowding PSF photometry with programs like DAOPHOT (see Sec. 2.3.2) provides better results.

The acquired instrumental magnitudes of the observed standard stars were fitted against the published values (see Fig. 3.3), using Equation. (3.6) for a fit without and Equation. (3.8) for a result with color-terms. Equations (3.9) show the results obtained from the fit without color-terms.

$$\begin{aligned}
 B &= b - 1.51 \pm 0.01 - 0.29 \pm 0.02 * am \\
 R &= r - 1.19 \pm 0.01 - 0.08 \pm 0.01 * am \\
 I &= i - 1.52 \pm 0.02 - 0.08 \pm 0.01 * am
 \end{aligned} \tag{3.9}$$

Equations (3.10) give the results for the fit with color-terms.

$$\begin{aligned}
 B &= b - 1.58 \pm 0.04 - 0.05 \pm 0.02 * (b - r) - 0.29 \pm 0.02 * am \\
 R &= r - 1.27 \pm 0.05 - 0.04 \pm 0.03 * (b - r) - 0.08 \pm 0.01 * am \\
 I &= i - 1.77 \pm 0.02 - 0.42 \pm 0.02 * (r - i) - 0.08 \pm 0.01 * am
 \end{aligned} \tag{3.10}$$

These calibrations were applied to the measured magnitudes of a list of well resolved stars in the summed image of every dwarf galaxy observed during the same night as the calibration stars. These stars then served as secondary standards to calibrate the deep reference images. The detailed results of the calibrations are listed in Table 3.2.



Galaxy	$B$	$R$	$I$
Leo A	2.027	1.177	2.238
GR 8	2.588	3.206	2.477

Table 3.2: Zeropoints obtained for the calibration using the zeropoints and color-terms listed in Equation. (3.10). The typical standard deviation of the fit is in the order of 0.04 mag.

### 3.4 Comparison of results

The main incentive to obtain the calibration at Calar Alto was, besides the need of a calibration for EGB 0427+63, the prospect of an independent comparison to the HST calibration. To achieve this we positionally matched sources from the calibrated WST DAOPHOT catalog and objects from the Calar Alto reference image and plotted the magnitudes against each other. The results are shown in Fig. 3.4.

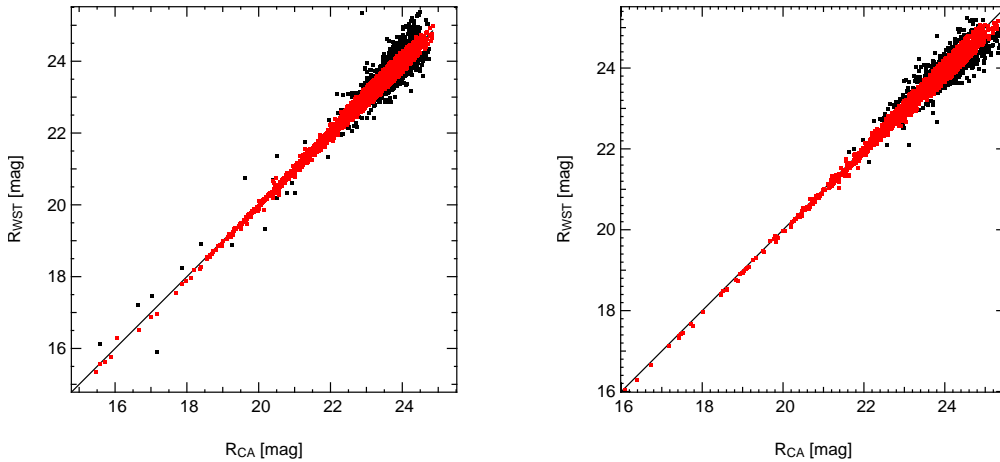


Figure 3.4: Comparison of the calibration in the  $R$ -Band between the HST calibrated Wendelstein data and the standard star calibrated Calar Alto observations using Table 3.2. The left panel shows the results for Leo A, the right one for GR 8. The black points are the matched objects, the red ones those remaining after the sigma-clipping.

The offset of the best fit for Leo A is 0.018 mag with a standard deviation of 0.002 mag and 0.062 with 0.003 mag standard deviation for GR 8. These results are in extremely good agreement, considering that two completely different datasets calibrated using independent calibration methods.

For the  $B$  and  $I$ -band the situation looks different. A comparison of the zeropoints for the Calar Alto reference image in Table 3.1 and Table 3.2 shows differences in the order of 0.3 mag. To solve this discrepancy several possible reasons have to be evaluated.

First of all, a possible source for problems could be an unsound selection of stars for the transfer of the calibration onto the reference image. The use of red stars for the

*B*-band calibration or blue stars for the *I*-band calibration presents a possible source for a deviation of the final calibration zeropoint.

In case of the *B*-band, the stars used to transfer the calibration from the HST data show suitable blue colors in the range of  $(B - I)$  of  $-1$  to  $1$ . The stars employed as secondary standards for the calibration of the Calar Alto *B*-band obtained on the NGC2264 field however have relatively red colors of around  $1$  to  $2$  in  $(B - I)$ . Unfortunately this is inevitable, as already all suitable stars (bright, isolated) are used.

The *I*-band data calibration suffers from a similar problem, with the stars used for the HST calibration having suitable colors in the  $B - I$  range from  $2$  to  $4$ . The stars available for the Calar Alto calibration have colors in between  $1$  and  $2$  in  $(B - I)$ . This color range could still be sufficient, but in this case it is aggravated by another problem. The observations were obtained using a Johnson *I* filter with a transmission curve significantly different from the Cousins filter used for the standard star observation by [Flaccomio et al. \(1999\)](#). The Johnson filter transmits flux beyond the red cutoff of the Cousins filter.

Given these results of the comparison and of different empirical tests like a comparison of the *I*-band magnitude of the tip of the red giant branch (see Sec. 6), we decided to use the HST based calibration in the *B* and *I*-bands.

## Chapter 4

# Catalog of variable sources

The reduced difference images produced by the reduction pipeline give the information about the relative variability of each pixel in the observed frame. From this vast amount of data candidates for periodic variability have to be selected. For these a period solution is derived at the same time further selecting sources with periodic variability. The remaining objects are assembled into a catalog of variable sources and form the basis for further scientific studies.

### 4.1 Detection of the variable sources

To select candidates for variability in the difference images it was assumed that the difference magnitude of a regularly variable star would exceed its respective error on a sizable number of epochs. Capitalizing on this alone, i.e. just searching for deviant pixels, would still produce a far too large number of candidate sources, as all the pixels lying within the PSF of a variable star would show up as individual sources. To circumvent this problem a means to reassemble the stars is needed. To attain this an image was assembled with each pixel holding the number of epochs for which the difference flux of this specific pixel is larger than the corresponding error. This image could then be searched for local maxima over a given threshold to select candidates for variability. The exact number of epochs applied as threshold for each dwarf galaxy are given with the catalog at the end of this chapter. This approach can still lead to multiple detections, yet a lot fewer. To deal with these, the resulting variability catalog is position-matched against the object catalog obtained on the deep reference image. From all the variable sources matching against the same stellar source only the one with the most significant period signal is kept.

## 4.2 Period determination

The detection technique outlined above still produces only a list with positions of possible candidates for periodic variability. All these data has to be assembled into light-curves and these checked for their credibility. Different approaches to determine the most relevant parameter of the light-curve, the period, are described in the applicable literature.

The data can be fitted with analytic forms of the expected light-curve. This procedure often used in the search for RR-Lyra stars, and in a lesser degree for Cepheids, demands well sampled data, as it introduces more parameters into the fit than just the basic two given above. The often, at least slightly, irregular shape of long period variables demotes the viability of this procedure even further. The resulting increase in complexity combined with the rather sparse sampling of the dataset this is not expected to be a worthwhile attempt.

The Lomb algorithm (Lomb, 1976; Scargle, 1982) provides means to reliably detect a periodic signal even in irregularly sampled data. This algorithm was used to detect the  $\delta$  Cephei stars and other short period variables, see Gössl (2006) for details on this part of the project. Tests on our dataset showed that it is unsuitable for the search for LPVs. It provides more stable results when many periods are sampled. For the long period content with only few periods observed, it often failed to produce usable results. Those detected serve as a cross check for the applied period determination method.

Empirical tests on our dataset showed that the Lafler-Kinman statistic (Lafler & Kinman, 1965) provides the best results given the peculiarities of our specific dataset. The Lafler-Kinman statistic provides a measurement of the smoothness of the curve in the phase diagram for a given trial period.

For this, the observed datapoints are first rearranged according to their phase for a given test period. The sum  $\Theta$  of the squared differences of magnitude differences between the then neighboring observations should be at a minimum for the correct period. The parameter  $\Theta$  is defined as

$$\Theta = \frac{\sum_i (m_i - m_{i+1})^2}{\sum_i (m_i - \bar{m})^2} \quad (4.1)$$

with the average magnitude  $\bar{m} = \frac{\sum_i m_i}{N}$  with the number of observations  $N$ . In a first step  $\Theta$  was calculated for a grid between 1 day and 1500 days. This period range was subdivided into  $n$

$$n = \log_2 \left( \frac{p_{max}}{p_{min}} \right) \cdot 1536 \quad (4.2)$$

steps and the test periods  $p_i$  chosen as

$$p_i = 2^{-\frac{(i-1)}{1536}} \cdot p_{max} \text{ for } i \text{ in } [1, n] \quad (4.3)$$

to create a grid with increasingly finer stepping for smaller periods. From these calculations the 100 lowest  $\Theta(P)$  were selected. For each corresponding period a regular grid is created consisting of 200 periods in a  $\pm 10\%$  range around that initial test period. The calculation of  $\Theta$  is repeated on each of these refined grids and the period with the now minimal  $\Theta$  written to a file.

The results can be culled according to the minimum  $\Theta$ . For a random distribution of magnitudes, the expected  $\Theta$  would be 2. Empiric tests showed that the best results were found for  $\Theta$  values lower than 1, but due to the sometimes irregular shape of the light-curves of LPVs  $\Theta$  values of up to 1.5 are considered.

As a last step the resulting light-curves, rearranged according to their phase given the respective trial period, were plotted for the test periods and the best fitting result selected by optical inspection.

### 4.3 Estimation of the average magnitude

The reference frame is composed of a rather large fraction of the epochs observed ( $\sim 30\%$ ) towards the respective dwarf galaxy. Naturally one would assume that averaging enough epochs spread over the light-curve, the resulting source in the combined reference frame should provide a stable estimate of the mean magnitude of the variable for those cases where the sampled time interval  $\Delta t$  is much larger than the intrinsic period  $P$  of the variable ( $\Delta t \gg P$ ) and where the average magnitude  $\langle m \rangle$  is safely above the limiting magnitude  $m_{lim}$  assuring that most of the variability can be recorded by the observations ( $\langle m \rangle < m_{lim}$  and  $\Delta \frac{m}{2} \leq m_{lim} - \langle m \rangle$ ). Another complication arises since the magnitude obtained from the reference frame is an average of fluxes, while the average magnitude for a variable usually is given as a magnitude average.

#### 4.3.1 The general case

To test this hypothesis and to investigate the influence introduced by the different averages at the same time, several artificial light-curves were created and the flux averages were calculated using our observed epochs. This was done using five different amplitudes in the range 0.2 to 1.8 mag peak to peak variation and periods between 0.1 and 1500 days. The phase was taken into account by averaging over 100 different values. Fig. 4.1 shows the results obtained for the Leo A dwarf galaxy using all available epochs. These results should be considered a best case scenario and serve as comparison for the simulations created using the subset of epochs used to create the actual reference frame.

The offset of the average deviation stems from the different ways to obtain the average magnitude, a sum over the fluxes or the magnitudes. While it can be neglected for small amplitudes, it must be reckoned with in the case of large amplitude variables. The overall large spread between the minimum and maximum deviation

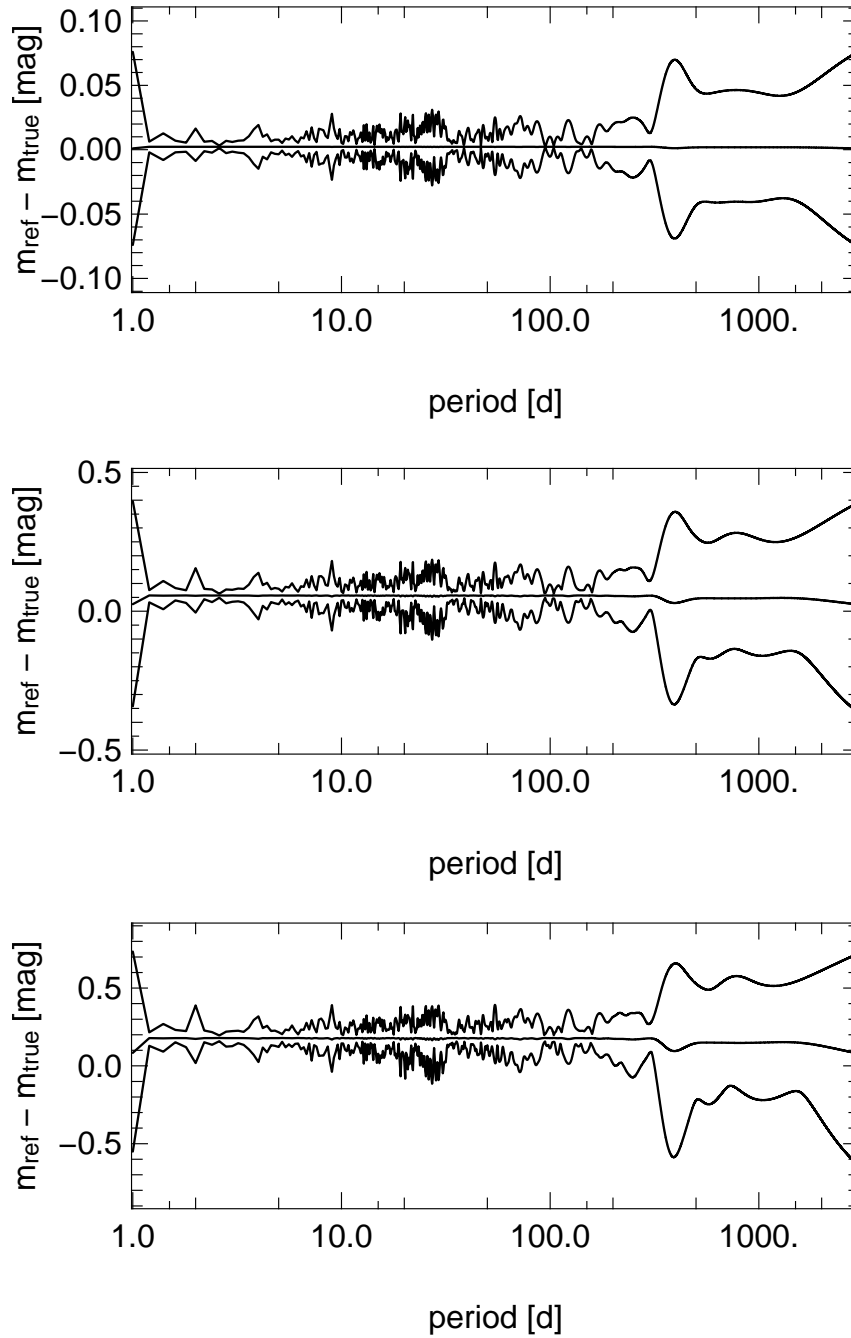


Figure 4.1: The deviation of the true average magnitude from the magnitude obtained from a flux averaged reference frame for the Leo A dwarf galaxy if all observed epochs would be used. Shown are the results for variables with a peak to peak variation of 0.2, 1 and 1.8 mag in the upper, middle and lower panel. The three curves plotted in each panel give the minimum, average and maximum deviation obtained during the test of 100 different phases in the light-curve generation.

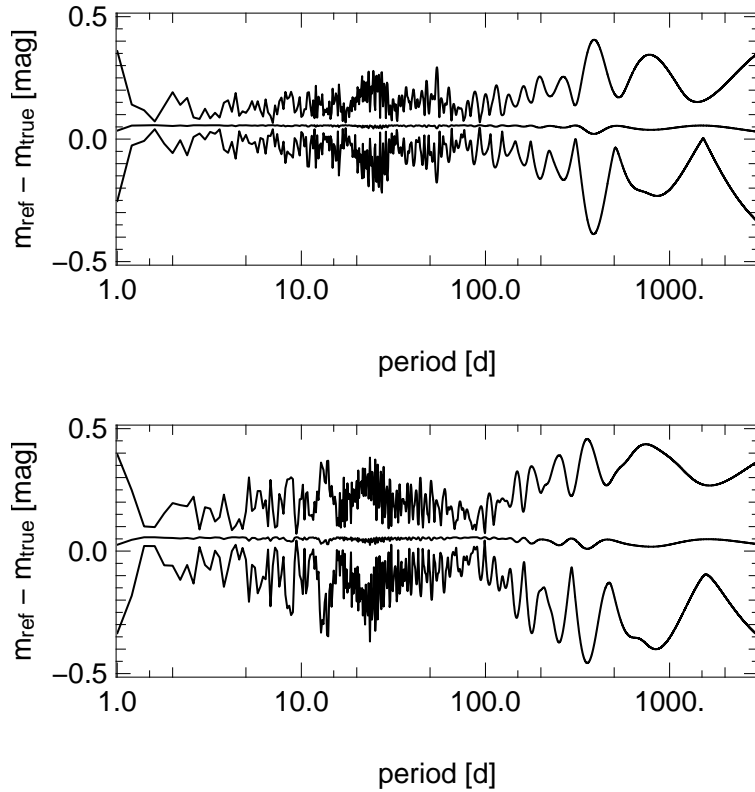


Figure 4.2: Deviation of the true average magnitude from the magnitude obtained from the flux averaged reference frame for the Leo A (upper panel) and Pegasus dwarf galaxy (lower panel) using the observed epochs of the respective reference frame. Shown in each panel are the results for variables with a peak to peak variation 1 mag. The three curves plotted each time give the minimum, average and maximum deviation obtained during the test of 100 different phases in the light-curve generation.

found arises from the shifting of the light-curve through the observed epochs as the test phase changes. Another interesting feature is the great maximal deviation for periods of about one year, here clearly the half-year observing window of our data becomes visible.

For small amplitude variables that fulfill the criteria outlined above, it can be assumed safely that the magnitude measured in the reference frame provides a good approximation of the true mean magnitude. For large amplitudes and especially for large periods, this assumptions does not hold any more in general.

### 4.3.2 The specific cases

To aggravate the situation even further, it has to be considered that the reference frame is not constructed from all available epochs but just a few selected ones. To test for

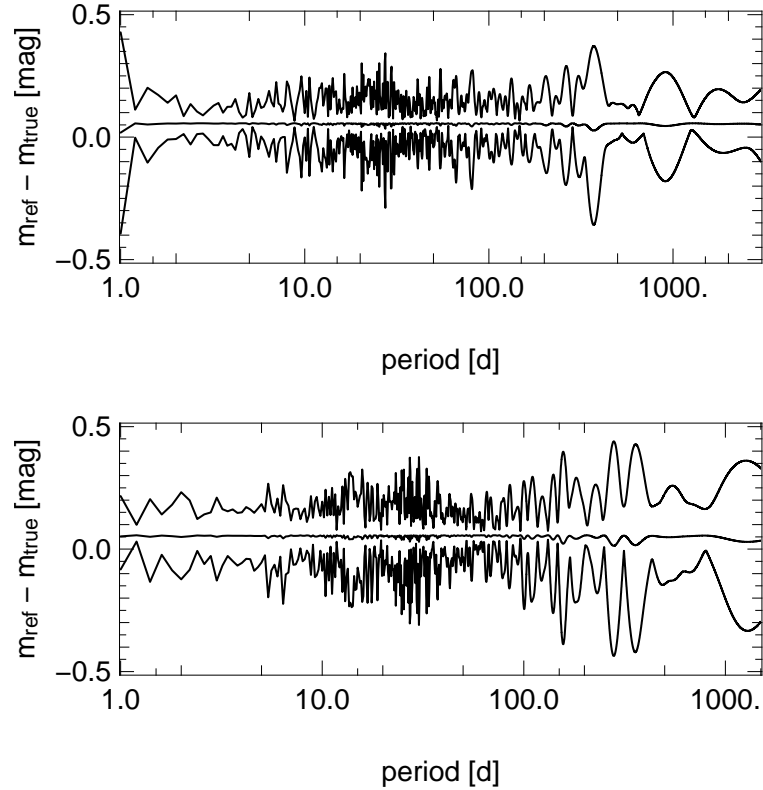


Figure 4.3: Deviation of the true average magnitude from the magnitude obtained from the flux averaged reference frame for the GR 8 (upper panel) and DDO 210 dwarf galaxy (lower panel) using the observed epochs of the respective reference frame. Shown in each panel are the results for variables with a peak to peak variation 1 mag. The three curves plotted each time give the minimum, average and maximum deviation obtained during the test of 100 different phases in the light-curve generation.

problems introduced by these limitations the simulations outlined above were conducted for each dwarf galaxy, using only the epoch actually used in the reference frame.

The obtained results are shown in Fig. 4.2 and Fig. 4.3. Due to the similarity in the shape of the resulting curves, only the results for variables with 1 mag amplitude are shown. The average deviation does not change in comparison with the results shown above. This is not surprising, as it originates from the different approaches used to calculate the magnitude average. The maximal offsets are, again as expected, larger due to the smaller number of contributing epochs. This is worst for the DDO 216 dwarf, where the fewest different epochs are used for the reference frame.

The results found in these simulations show that especially for variables with long periods the magnitude in the reference frame does not provide sufficiently reliable results. To bypass this problem, the magnitude averages shown in the table in Sec. 4.4 were obtained using a fit of a cosine against the phase reordered magnitudes.



## 4.4 The variable source catalog

In the following the resulting object catalogs for the analyzed dwarf galaxies are presented. The listed periods were derived using the Lafler-Kinman statistic as described above. The amplitudes and average magnitudes are the results of a fit of a cosine of the form

$$m(x) = A * \cos(2\pi x + ph) + \langle m \rangle \quad (4.4)$$

over the phase index  $x \in [0, 1]$  against the corresponding magnitudes  $m$  of the phase reordered light-curve. The fitted parameters were the amplitude  $A$ , the phase  $ph$  and the average magnitude  $\langle m \rangle$ . The amplitude listed in the table is twice the fitted one, thus giving the peak to peak amplitude. The other parameters listed are the celestial coordinates and the Lafler-Kinman  $\Theta$  parameter for the given period.

### 4.4.1 Leo A

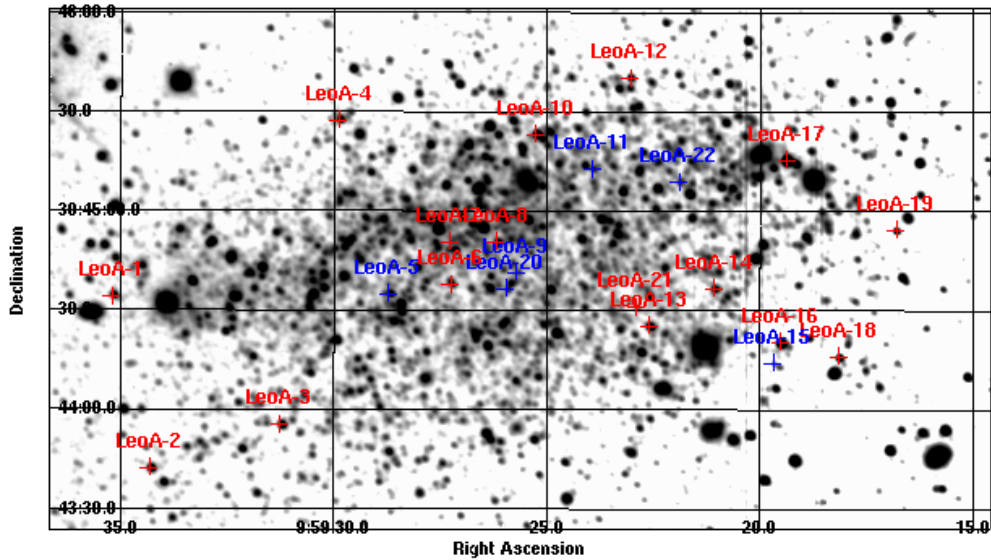


Figure 4.4: Finding chart for the detected variables sources in Leo A. Variables with periods longer than ten days are shown in red, those with shorter periods in blue.

For Leo A, the threshold applied for the detection on the variation mask were a minimum of 39 epochs with a value larger than the associated error. In total 22 variable sources were identified, see Table 4.1 for details and Appendix B.1 for plots of the light curves. Out of these six have periods smaller than ten days and can be considered to be Cepheids or other short period variables. The period of LeoA-21 with 27.5 days is too short to be a typical LPV. Given the period alone it could be a Cepheid as well, according to the compilation by [Groenewegen et al. \(2004\)](#) the longest period of Cepheid known is 130 days. Yet under this assumption the variable would be much

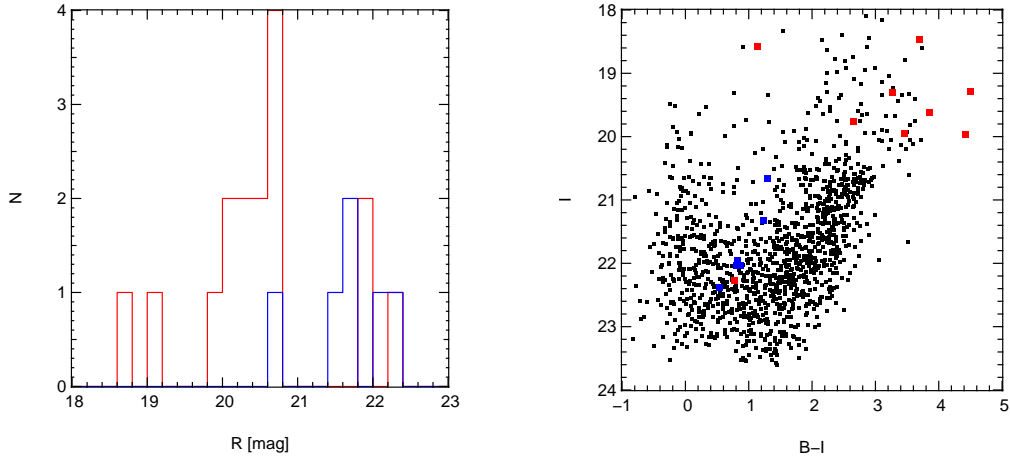


Figure 4.5: The left panel shows the luminosity function of the variables found in Leo A. The right panel shows the color-magnitude diagram for Leo A in the  $B$  and  $I$ -band, with the variables recovered in these bands over-plotted. In both cases the LPVs with periods longer than ten days are shown in red and the short period variables with shorter periods in blue. The color-magnitude diagram is generated from the  $B$  and  $I$ -band data obtained at Calar Alto.

too faint if it were part of Leo A. In addition, neither the light-curve shape nor the amplitude would be in agreement with a classical  $\delta$  Cephei star.

A finding chart of the variable sources is shown in Fig. 4.4. The variables with periods longer than ten days are plotted in red, those with shorter periods in blue. The spatial distribution of the variable sources shows no peculiarities with respect to the visible shape of the dwarf galaxy. It is interesting that all the detected variables lie within the Holmberg radius of Leo A (of old stars extending well outside the Holmberg radius). The paucity of variables in this area will be further investigated in chapter 6.2.

The left panel in Fig. 4.5 shows the luminosity function of the variable sources, again color-coded for variables with periods longer and shorter than ten days. All but three long period variables have magnitudes brighter than 21 mag in the  $R$ -Band, while all but one short period variables have periods fainter than 21 mag. Schulte-Ladbeck *et al.* (2002) find a distance modulus of Leo A based on a magnitude of the tip of the red giant branch (TRGB) of 20.5 in the  $I$ -Band. Typical LPVs on the thermally pulsing asymptotic giant branch are expected to show average magnitudes above the TRGB magnitudes. The candidate Cepheids all show average  $I$ -band magnitudes below the TRGB. Massive stars entering the Cepheid instability strip on their loops from the AGB, would be located above the TRGB. The average magnitudes below the TRGB can be explained by the typical bluer colors of Cepheids compared to LPVs, leading to fainter magnitudes in the  $R$ -band.

The right panel in Fig. 4.5 shows the color-magnitude diagram for Leo A with the variable sources recovered in the  $B$  and  $I$ -band over-plotted using the same color-coding as described above. Almost all long period variables fall into the expected

ID	RA (J2000)	Dec (J2000)	$p$ [d]	$A$ [mag]	$m$ [mag]	$\Theta$
LeoA-1	9:59:35.22	30:44:34.3	268.62	0.67	20.7	0.44
LeoA-2	9:59:34.35	30:43:42.4	432.91	1.09	20.1	0.23
LeoA-3	9:59:31.29	30:43:55.7	434.02	0.19	20.1	0.51
LeoA-4	9:59:29.91	30:45:27.6	182.45	0.06	20.5	0.97
LeoA-5	9:59:28.74	30:44:35.2	6.49	0.33	20.6	0.44
LeoA-6	9:59:27.27	30:44:37.9	311.06	1.50	21.9	0.55
LeoA-7	9:59:27.29	30:44:50.9	362.03	1.15	21.8	0.80
LeoA-8	9:59:26.21	30:44:50.8	331.04	0.14	20.7	0.66
LeoA-9	9:59:25.73	30:44:41.7	1.56	0.32	22.1	1.38
LeoA-10	9:59:25.28	30:45:23.3	919.28	0.16	20.0	0.77
LeoA-11	9:59:23.95	30:45:12.8	3.35	0.32	21.5	1.06
LeoA-12	9:59:23.07	30:45:40.3	268.42	0.10	20.7	1.12
LeoA-13	9:59:22.62	30:44:25.5	283.64	0.13	20.3	0.96
LeoA-14	9:59:21.10	30:44:36.9	170.70	0.41	20.6	0.47
LeoA-15	9:59:19.71	30:44:14.4	1.81	0.59	22.2	1.14
LeoA-16	9:59:19.54	30:44:20.6	273.86	0.07	19.1	0.95
LeoA-17	9:59:19.39	30:45:15.5	74.83	0.15	18.6	0.62
LeoA-18	9:59:18.16	30:44:16.3	299.05	0.34	20.4	0.56
LeoA-19	9:59:16.81	30:44:54.5	537.99	0.50	20.6	0.56
LeoA-20	9:59:25.98	30:44:36.6	1.61	0.18	21.7	1.09
LeoA-21	9:59:22.92	30:44:31.2	27.38	0.40	22.3	1.33
LeoA-22	9:59:21.91	30:45:09.0	1.52	0.10	21.7	1.29

Table 4.1: Catalog of the variables sources found in the Leo A dwarf galaxy. Shown is an ID, Right Ascension and Declination, the best fitting period, the fitted average magnitude and the  $\Theta$  parameter of the Lafler-Kinman statistic.

region above and right from the tip of the red-giant branch that can be clearly seen at an  $I$ -band magnitude of approximately 20.5. There are two LPVs not falling in this regime, LeoA-22 with an  $I$ -band magnitude of 22.27 was already discussed above. The second one, LeoA-18, with an  $I$ -band magnitude of 18.57 and an unusually blue color, could possibly be a type-II Cepheid or an RV-Tauri star, though both classifications are highly uncertain. With a period of 74.9 days and an amplitude of 0.16 mag it is anyway an unlikely candidate for a typical LPV. Excluding the remaining variables with magnitudes below the TRGB that are unlikely to be LPVs on the TPAGB, the final tally of classical LPVs in Leo A is eleven.

#### 4.4.2 DDO 216

Applying a threshold of 32 on the variation mask, a total of 55 variable sources were detected in the DDO 216 dwarf galaxy. Table 4.2 lists the details, the plots of the light-curves are shown in Appendix B.2. The positions of the sources with respect to the dwarf galaxy are shown in the finding chart in Fig. 4.6. It should be noted that

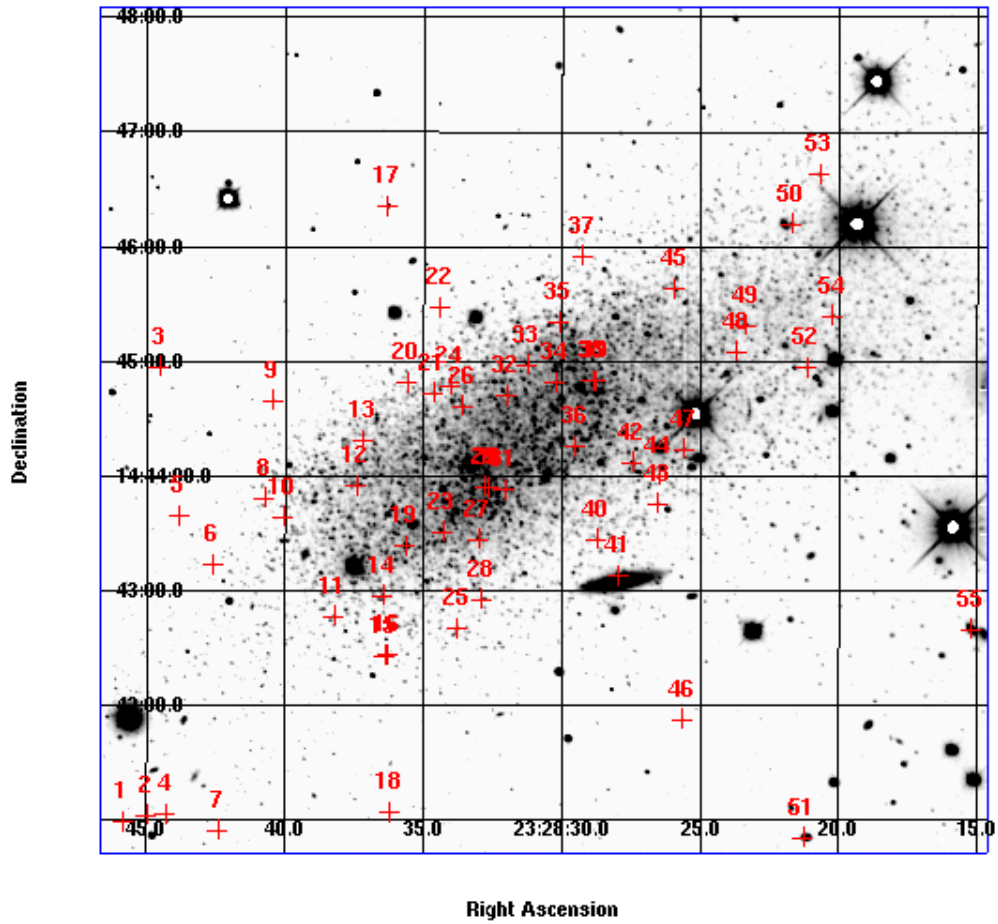


Figure 4.6: Finding chart for the detected variables sources in DDO 216.

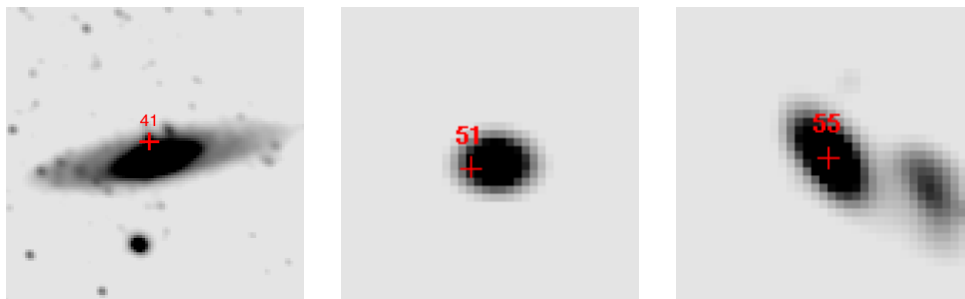


Figure 4.7: Postage stamps of the DDO 216 variable sources DDO216-41 (left panel), DDO216-51 (middle panel) and DDO216-55 (right panel).

the Laffer-Kinman algorithm finds no  $\delta$  Cephei variables in DDO 216 even though the Lomb algorithm detects some (see Gössl, 2006).

An optical inspection of the finding chart turns up three peculiar objects, DDO216-41, DDO216-51 and DDO216-55. Fig. 4.7 shows postage stamp images of the counterparts of the variable sources. DDO216-55 could be a variable galactic core of a background galaxy. DDO216-51 could be associated with the underlying galaxy as well, or be an super imposition of a variable star onto the distant galaxy. The photometry for both objects would in any case be influenced by the respective galaxies, so these two objects are excluded from the further analysis. In case of DDO216-41 the source of variability falls in front of a distant spiral galaxy, but a close inspection suggests that it is just a chance alignment between a variable star in DDO216 and a background galaxy.

The lack of *B* and *I*-band data makes the classification of the variables according to their location in the color-magnitude diagram impossible. The area covered by the HST observations is too small to be of help. The only remaining method is the use of their magnitude distribution. Fig. 4.8 shows the luminosity function of all the variable sources detected in DDO 216. As in the case of Leo A, the brightness of the tip of the red giant branch (TRGB) can be used as a discrimination of the classical LPVs. Gallagher *et al.* (1998) found for DDO 216 an *I*-band brightness of 20.85 mag for the TRGB using deep HST imaging. Again assuming that the LPVs would be brighter than that limit and that the corresponding magnitude in the *R*-band would be fainter, the variable with an average magnitude just above 23 mag (DDO216-13) is removed from the sample as well.

ID	RA (J2000)	Dec (J2000)	$p$ [d]	$A$ [mag]	$m$ [mag]	$\Theta$
DDO216-1	23:28:48.94	14:41:18.8	144.65	0.39	21.2	0.73
DDO216-2	23:28:48.08	14:41:22.0	499.24	0.41	21.2	0.50
DDO216-3	23:28:47.66	14:45:16.9	531.40	0.72	22.0	0.85
DDO216-4	23:28:47.38	14:41:22.7	124.19	0.59	21.6	0.76
DDO216-5	23:28:46.92	14:43:58.8	37.05	0.77	21.6	0.54
DDO216-6	23:28:45.71	14:43:33.6	420.35	0.25	21.2	0.72
DDO216-7	23:28:45.48	14:41:14.2	601.40	1.71	22.5	0.40
DDO216-8	23:28:43.84	14:44:08.1	216.53	0.57	21.6	0.59
DDO216-9	23:28:43.53	14:44:59.6	130.21	0.46	21.2	0.51
DDO216-10	23:28:43.15	14:43:58.3	204.91	0.50	21.8	0.66
DDO216-11	23:28:41.31	14:43:06.4	137.59	0.26	21.1	1.14
DDO216-12	23:28:40.51	14:44:14.6	97.44	0.42	21.6	0.68
DDO216-13	23:28:40.26	14:44:38.4	490.60	1.94	22.8	0.67
DDO216-14	23:28:39.56	14:43:17.2	253.05	0.34	21.2	0.71
DDO216-15	23:28:39.49	14:42:45.9	126.13	0.63	21.4	0.54
DDO216-16	23:28:39.38	14:42:46.5	126.92	0.43	21.6	0.74
DDO216-17	23:28:39.38	14:46:41.3	317.37	0.23	19.4	0.90
DDO216-18	23:28:39.28	14:41:23.8	276.92	0.19	20.8	0.77
DDO216-19	23:28:38.73	14:43:43.3	312.57	0.04	18.1	0.56

*continued on the next page*

*continued from the previous page*

ID	RA (J2000)	Dec (J2000)	$p$ [d]	$A$ [mag]	$m$ [mag]	$\Theta$
DDO216-20	23:28:38.67	14:45:09.0	163.92	0.74	22.2	0.93
DDO216-21	23:28:37.73	14:45:03.4	55.61	0.45	21.4	1.05
DDO216-22	23:28:37.50	14:45:48.0	317.41	0.56	21.7	0.90
DDO216-23	23:28:37.38	14:43:50.7	223.25	0.57	21.8	0.89
DDO216-24	23:28:37.13	14:45:07.4	403.97	1.16	21.6	0.26
DDO216-25	23:28:36.86	14:43:00.0	215.78	0.33	21.3	0.78
DDO216-26	23:28:36.68	14:44:56.3	317.47	0.47	21.5	0.89
DDO216-27	23:28:36.10	14:43:46.7	205.37	0.42	20.9	0.28
DDO216-28	23:28:36.01	14:43:15.2	116.72	0.32	21.3	1.07
DDO216-29	23:28:35.87	14:44:14.0	93.33	0.13	19.4	0.83
DDO216-30	23:28:35.73	14:44:13.4	125.38	0.42	21.9	0.79
DDO216-31	23:28:35.16	14:44:12.5	163.36	0.57	21.4	0.79
DDO216-32	23:28:35.10	14:45:01.8	114.83	0.48	21.2	0.79
DDO216-33	23:28:34.37	14:45:18.2	174.37	0.46	21.3	0.62
DDO216-34	23:28:33.34	14:45:08.5	160.32	0.64	21.1	0.39
DDO216-35	23:28:33.22	14:45:40.0	255.56	2.08	22.1	0.49
DDO216-36	23:28:32.64	14:44:35.2	188.55	0.76	21.9	0.79
DDO216-37	23:28:32.37	14:46:15.0	128.90	0.49	21.6	0.85
DDO216-38	23:28:31.99	14:45:09.6	146.30	0.73	22.2	0.68
DDO216-39	23:28:31.87	14:45:09.7	145.55	0.88	21.3	0.33
DDO216-40	23:28:31.83	14:43:46.5	663.94	0.49	20.9	0.42
DDO216-41	23:28:31.08	14:43:27.3	160.87	0.41	20.2	0.64
DDO216-42	23:28:30.57	14:44:26.8	33.92	0.18	20.7	1.03
DDO216-43	23:28:29.65	14:44:05.1	258.32	0.30	21.3	0.51
DDO216-44	23:28:29.62	14:44:20.0	233.05	0.44	21.5	0.81
DDO216-45	23:28:29.05	14:45:57.4	311.57	0.25	21.1	0.61
DDO216-46	23:28:28.75	14:42:12.2	308.32	0.43	21.1	0.52
DDO216-47	23:28:28.70	14:44:33.5	163.50	1.32	21.3	0.44
DDO216-48	23:28:26.83	14:45:24.5	442.33	1.24	22.3	0.53
DDO216-49	23:28:26.46	14:45:38.6	275.90	0.29	21.2	0.76
DDO216-50	23:28:24.82	14:46:31.6	249.94	0.23	20.7	0.66
DDO216-51	23:28:24.38	14:41:10.9	433.74	0.14	20.3	0.77
DDO216-52	23:28:24.28	14:45:16.5	233.29	0.38	21.8	1.01
DDO216-53	23:28:23.82	14:46:57.2	130.38	0.38	21.0	0.72
DDO216-54	23:28:23.34	14:45:43.3	275.30	0.28	21.3	0.84
DDO216-55	23:28:18.28	14:42:59.8	858.02	0.05	18.7	0.45

Table 4.2: Catalog of the variables sources found in the DDO 216 dwarf galaxy. Shown is an ID, Right Ascension and Declination, the best fitting period, the fitted average magnitude and the  $\Theta$  parameter of the Lafler-Kinman statistic.

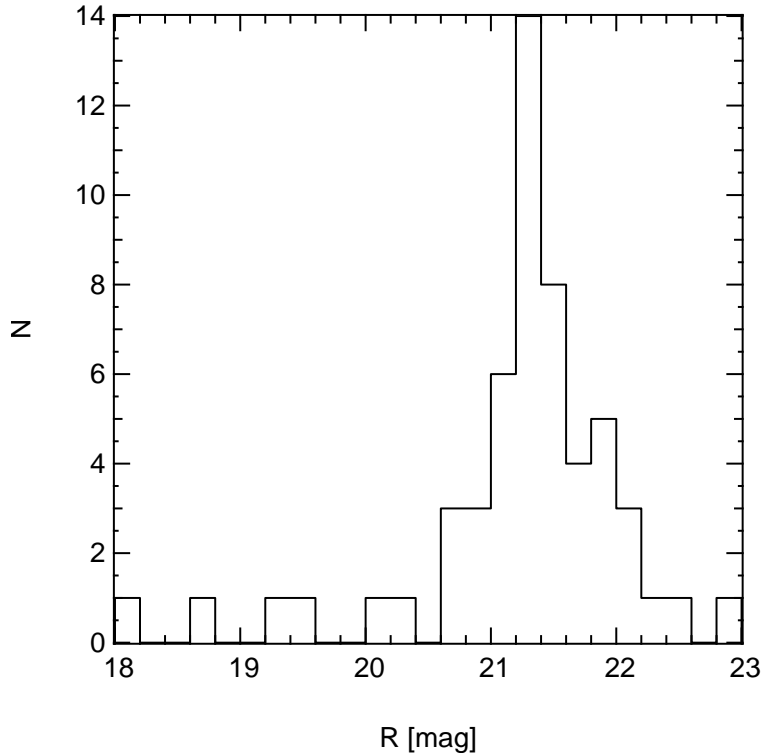


Figure 4.8: Luminosity function of the variable sources found in DDO 216

With these dubious candidates removed, the total sum of LPVs in the DDO 216 dwarf galaxy comes out as 52. The spatial distribution of the variables sources with respect to visually prominent part of the galaxy shows that the dwarf galaxy extends at least within the field of view of our observations.

#### 4.4.3 GR 8

In GR 8 a total of three securely identified variable sources were found, using the threshold of 46 in the variation mask. This low number roots in the large distance of the dwarf galaxy of 2.2 Mpc (Dohm-Palmer *et al.*, 1998) and a resulting distance modulus of 26.75. As a result most variable sources are located beyond our detection limit. An inspection of the candidates for variability produced by the Lafler-Kinman statistic shows some candidates with probable maximum peaks above the noise background, but in most cases the noise of the resulting light-curve is too high to make it credible.

The left panel in Fig. 4.9 shows the finding chart for the variables. One of the three variables, GR8-2, with a period of 15.4 days can be classified as a classical  $\delta$  Cephei star. This one is plotted in blue, the two remaining LPVs are shown in red. Due to their faint magnitudes, the three variables cannot be recovered in the the  $B$  and  $I$ -band observations obtained at Calar Alto. Instead the variables are over-plotted on the deep  $V$  and  $I$ -band color-magnitude diagram constructed from the HST data published by

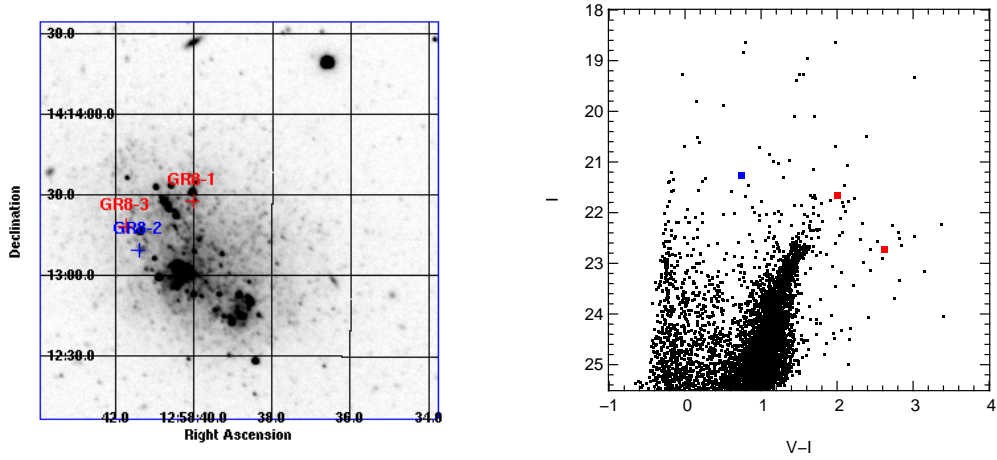


Figure 4.9: The left panel shows a finding chart for the detected variables sources in GR 8. The right panel shows the color-magnitude diagram based on the HST data from [Holtzman \*et al.\* \(2003\)](#), with the variables over-plotted. In both cases is the Cepheid plotted in blue, the two LPVs in red.

ID	RA (J2000)	Dec (J2000)	$p$ [d]	$A$ [mag]	$m$ [mag]	$\Theta$
GR8-1	12:58:40.03	14:13:27.8	183.21	0.26	21.4	1.16
GR8-2	12:58:41.41	14:13:09.6	15.42	0.34	21.5	1.14
GR8-3	12:58:41.75	14:13:18.5	223.95	0.98	22.7	1.12

Table 4.3: Catalog of the variables sources found in the GR 8 dwarf galaxy. Shown is an ID, Right Ascension and Declination, the best fitting period, the fitted average magnitude and the  $\Theta$  parameter of the Lafler-Kinman statistic.

[Holtzman \*et al.\* \(2003\)](#). The LPVs are, as expected, located near the red side of the AGB. The position of the Cepheid corresponds to a massive star crossing the instability strip on the blue loop.

Table 4.3 shows the details for all three detected variables, the accompanying plots of the light-curves are in Appendix B.3. The average magnitudes of the two LPVs are in agreement with the magnitude of the TRGB at  $I = 22.7$  found by [Dohm-Palmer \*et al.\* \(1998\)](#).

#### 4.4.4 DDO 210

In case of the DDO 210 dwarf galaxy a threshold of 44 was applied. Using this parameters and also testing other thresholds, no variables sources were found. This paucity will be further explored in Sec. 6.5.



# Chapter 5

## Completeness Simulations

### 5.1 Introduction

Astrophysical datasets can in the fewest cases be considered perfect, but suffer partly from severe side-effects of the analysis tools and mostly from limitations imposed by the available observations. To examine the data in a statistical manner, these first have to be assessed. A typical example of incompleteness in observational astronomy is the magnitude limit of observations. At some point faint objects are too faint to still be separated from the underlying background noise, leading to a cut-off in magnitude of the resulting dataset.

The common approach to measure this magnitude limit is to create artificial objects similar to the observed ones and distribute them randomly in the observed image. The detection algorithm is then applied to the modified image and the resulting catalog searched for the artificial objects. From the recovered and missing ones the limiting magnitude can be estimated. This procedure is iterated until a large enough sample of artificial objects has been evaluated and the result can be considered statistically stable. An example for this kind of approach is given in [Snigula \*et al.\* \(2002\)](#).

In case of the observations of variable sources the determination of the completeness of the dataset is much more complex, as the completeness of different parameters overlap. The relevant parameters characterizing the variable light-curves are:

- **Magnitude:** In case of variable sources, the single object has to be visible above the detection threshold during a minimum number of epochs, thus entangling the magnitude limit with the period and phase constraints.
- **Period:** Not all periods can be detected. These are on the one hand trivially limited by the length of the single observation at the short end and the length of the total observation campaign at the long end. Additionally the spacing of the observational epochs can influence the detection probability.

- **Amplitude:** The effects of magnitude and amplitude on the completeness are correlated. A faint variable with a large enough amplitude might still be detected, while a brighter one with a small amplitude fails to trigger a detection, as it is not above the threshold for a sufficient number of epochs. These effects are also entangled with the period. For faint variables it can be critical that the observation windows overlap with the maximum part of the light-curve.
- **Phase:** The relative position of the maximum brightness and the often limited observing window in the time domain are dependent on the phase of the light-curve. This leads to a dependency of the detection probability on the phase shift of the individual light-curve.
- **Position:** As an additional parameter special to our project the location of the variable star relative to their hosts is important. A star near the rim will be much less effected by crowding than those towards the center or near H II regions.

To estimate the completeness for a dataset comprised of variable sources, not only the parameters of the light-curves, but also the reduction and detection algorithms must be taken into account. This means that in the ideal case the artificial sources are placed in the raw images and the complete reduction and detection is repeated. Given the size of the parameter space and the number of different artificial variables needed, running such simulations is a very time-consuming undertaking.

## 5.2 The technical implementation

The main reason to calculate the completeness of our dataset is to study the possible star formation histories of the dwarf galaxies. In addition we decided to use it for a study of the characteristics of the algorithms used for the period search.

The simulations were carried out for 5 different amplitudes between 0.2 and 1.8 magnitudes peak to peak variation, 1500 periods with a constant spacing and 81 magnitudes in the range between 16 and 24 mag. Each variable was created with 10 different phases and the result were averaged. We decided not to treat the phase as a major parameter like period and magnitude. The phases of the real variables can safely assumed to be randomly distributed, so the analysis of their influence on the detection probability yields no scientific value. Using these parameters a large number of artificial variables were distributed over the image area.

Considering the massive amount of time needed to create the artificial sources for each combination of amplitude, period, magnitude and phase in each epochs image and then running the whole difference imaging and variability detection pipeline, using two different period search algorithms, we decided to use a different approach.

We apply three criteria to detect a variable source in our dataset, namely threshold in the variation mask, a positional coincidence with a detected source in the respective DAOPHOT catalog and, finally, the period detection algorithm.

To reduce the needed computational time and to avoid unneeded reiteration of identical detection checks on both period detection algorithms, the different criteria were tested independently. This approach allows an autonomous evaluation of the effects the different tests have on the total completeness of the dataset.

### 5.2.1 Generation of the light-curves

Instead of assembling the light-curves and then creating the artificial sources in all images we deemed it more efficient to first create a sample of stellar sources with varying brightnesses in all the images and later use this data to assemble the light-curves.

To accomplish this copies of the reference PSF star, with its flux scaled to the corresponding magnitude were placed in the individual images. These artificial sources were arranged on a set of four regular position grids and these grids were shifted with respect to each other. This process was done in several separate steps to avoid overlap between the different artificial sources. Each source was added onto the observed image to preserve the noise already present in the image. The difference imaging pipeline was run on the so prepared images and the values and errors extracted. The resulting three dimensional data-cube served as the basis for the different completeness simulations.

First the artificial light-curve was calculated assuming a cosine, as this provides a reasonable approximation of an LPV light-curve. Applying the relevant values for mean magnitude, amplitude, period and phase the magnitudes of the source at our dates of observation were derived. These magnitudes were then translated into their corresponding values after the application of the difference imaging pipeline using the artificial data-cube.

This approach allows the generation of arbitrary light-curves without the need to run the time-consuming difference imaging each time.

### 5.2.2 Variation mask completeness

As laid out in Sec. 4.1 the candidates for variable sources are selected using a threshold on a variation mask. This mask is created by summing, for each pixel, the number of epochs for which the pixel values in the difference image is larger than its error  $n$ -times. This selection criterion adds another possible source of incompleteness in the resulting catalog of variable sources.

To test the completeness of the detection on the variation mask, the different light-curves were assembled and the number of epochs with a value larger than the associated error  $n$ -times counted. This number was compared with the needed threshold and the completeness derived.

### 5.2.3 DAOPHOT completeness

The completeness of the DAOPHOT detections was determined by adding artificial sources to the reference image used for the actual DAOPHOT photometry, again copying the reference star PSF and rescaling it to the respective magnitude. `FIND`, `PHOT` and `ALLSTAR` were run on the resulting image and the artificial object searched in the output sourcelists. To consider an artificial source as recovered by DAOPHOT a positional coincidence within 1.5 pixel radius and a measured magnitude within 0.75 magnitudes of the magnitude of the artificial source were required. This procedure was repeated using the same positions and the same magnitude range as applied during the generation of the data-cube.

### 5.2.4 Period search completeness

The most critical as well as the most restrictive completeness is the the one of the algorithm to identify a periodic light-curve for the candidates. For the tests the difference image values corresponding to the magnitudes of the artificial light-curves were fed into the detection algorithm and the result compared with the respective thresholding parameters.

It should be kept in mind that this result gives only the probability that the detection algorithm flags the candidate as a source with a possible periodic signal. This test excludes the additional step applied in the standard pipeline, where the resulting light-curve is assessed for its credibility by eye. Considering the number of iteration needed for the simulation, applying this test would not be reasonable. It can be argued that this test is not needed, the simulations give a measurement of the percentage that can be recovered from the dataset in an ideal case.

## 5.3 Results

Even though all the simulations were carried out testing 5 different amplitudes for the artificial light-curves, we limit the plots presented in this chapter to the results obtained using 1 mag peak to peak amplitude. Tabulated results are given for the others.

### 5.3.1 Results for Leo A

For the completeness simulations of Leo A a total of nearly 900 artificial stars were created distributed on four different regular position grids overlapping the dwarf galaxy. These grids were shifted with respect to each other to avoid crowding of the artificial sources.

### Variation mask completeness

The upper and the middle left panels in Fig. 5.1 illustrate the results obtained for the completeness of the detection threshold applied on the variation mask. For 1 mag amplitude as shown, the average 50% completeness limit is approximately 24.1 mag. Table 5.1 lists these limits for all the five amplitudes analyzed.

	0.2 mag	0.6 mag	1 mag	1.4 mag	1.8 mag
Minimum	23.8	> 24	> 24	> 24	> 24
Average	> 24	> 24	> 24	> 24	> 24
Maximum	> 24	> 24	> 24	> 24	> 24

Table 5.1: Completeness limits for Leo A for the thresholding on the mask for variables as described Sec. 5.3.1. Shown are the minimum, average and maximum 50% completeness limits in magnitudes over the period dimension of the plot shown in the top panel of Fig. 5.1.

The degradation of the completeness limit for variables with periods around one year, reflected in the minimum limits in Table 5.2, is described in detail below in the discussion of the results for the Lafler-Kinman statistic that shows the same deficiency.

### DAOPHOT completeness

For this test the same sample of about 900 artificial stars was used. The simulation shows for the DAOPHOT detection a 50% completeness limit of 23.7 mag. The full results are shown in the lower panel of Fig. 5.2.

### Lafler-Kinman completeness

The middle right and the lower panel in Fig. 5.1 show the results for the completeness of the detection of variable sources with 1 mag amplitude using the Lafler-Kinman statistic. The average 50% completeness limit as shown, is approximately 21.8 mag. Table 5.2 lists these limits for all the five amplitudes analyzed.

The most interesting detail is the degradation of the achievable completeness for variables with a period length of about one year. The same phenomenon can be seen at periods of about 2 years, but to a lesser degree. This defect is a side-effect of the fact that the Lafler-Kinman statistic does not take into account the temporal distribution of the datapoints. For variables with periods in the range of one year only half of the light-curve is visible. This can either lead to perceived jumps (increasing the resulting  $\theta$ ) or to parts of the light-curve falling below the detection limit. This last effect is the reason for the incompleteness shown for the thresholding on the variation mask shown in Sec. 5.3.1.

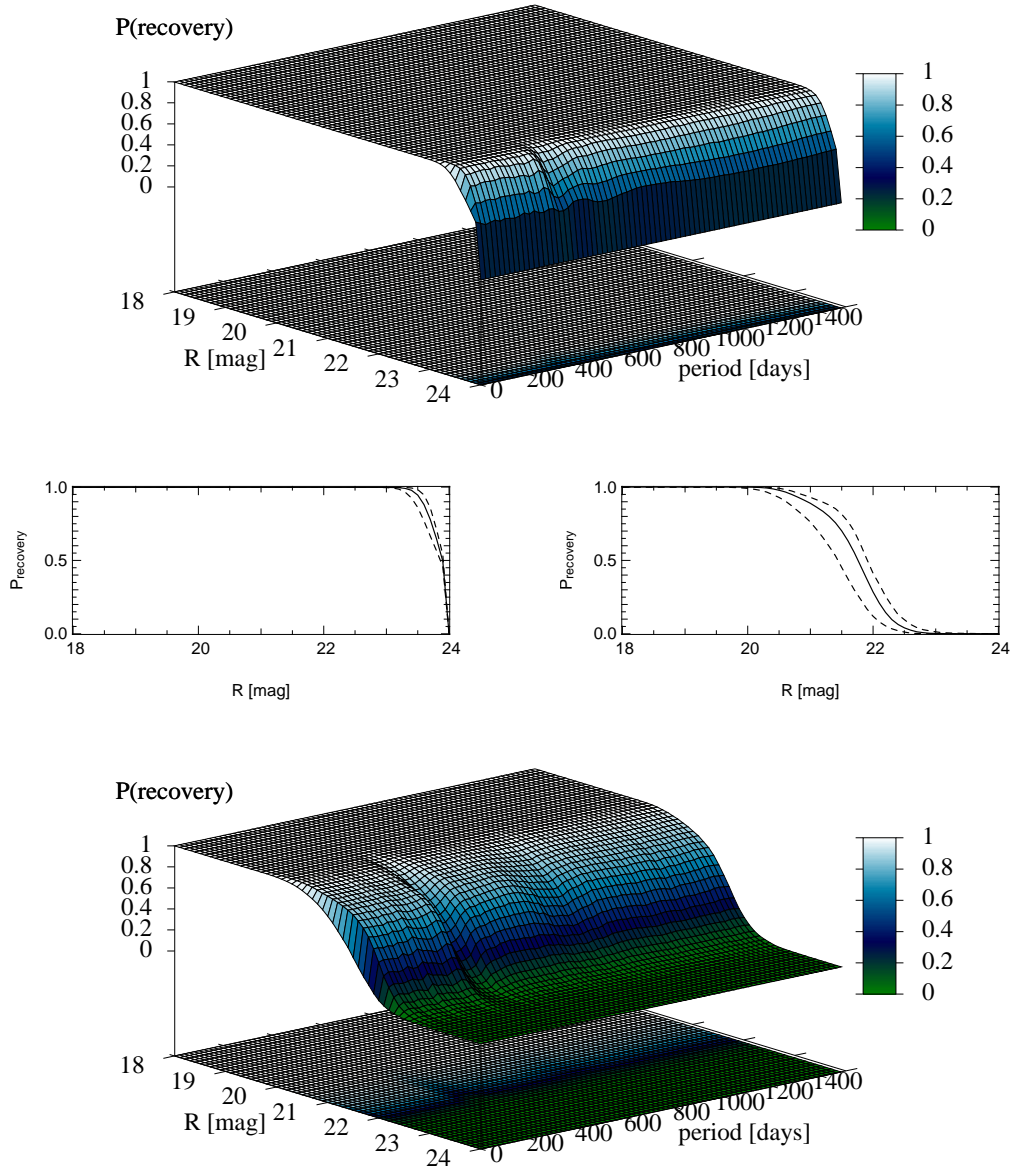


Figure 5.1: Results of the completeness simulations for the Leo A dwarf galaxy for artificial variables with 1 mag peak-to-peak amplitude. The upper and the middle left-hand panel show the results for completeness of the variation mask selection, the middle right-hand and the lower panel the results for the Lafler-Kinman statistic. The plots in the middle row give the minimum, average and maximum completeness as a function of magnitude, effectively collapsing the period dimension.

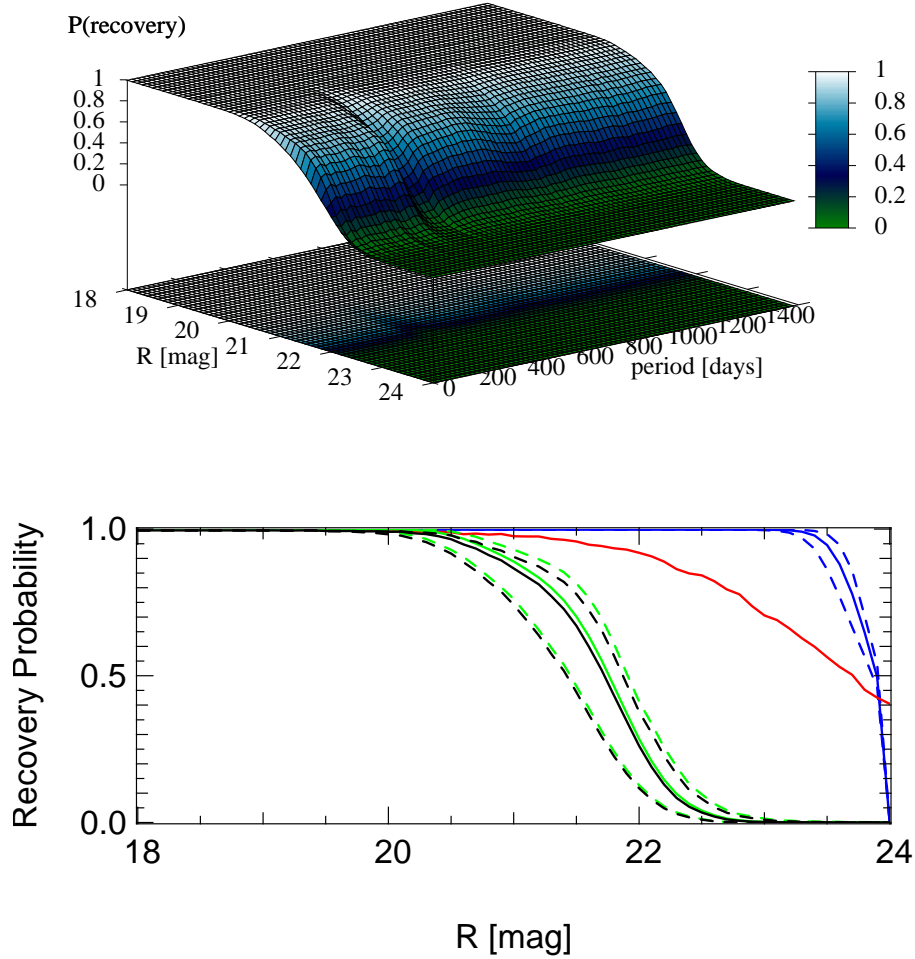


Figure 5.2: Results of the completeness simulations for the Leo A dwarf galaxy for artificial variables with 1 mag peak to peak amplitude. The upper panel shows the results for the cumulative completeness simulation, the lower one the minimum, average and maximum cumulative completeness (black) overlaid on the completeness of the variation mask (blue), the DAOPHOT detection (red) and the Lafler-Kinman statistic (green).

	0.2 mag	0.6 mag	1 mag	1.4 mag	1.8 mag
Minimum	20.3	21.0	21.4	21.8	22.1
Average	20.5	21.2	21.8	22.1	22.4
Maximum	20.6	21.4	21.9	22.3	22.6

Table 5.2: Completeness limits for Leo A for the detection using the Lafler-Kinman statistic. Shown are the minimum, average and maximum 50% completeness limits in magnitudes over the period dimension of Fig. 5.1.

### Summary

The upper panel of Fig. 5.2 shows the cumulative detection completeness for Leo A. It is obtained by multiplying the three different completenesses explored (variation mask, DAOPHOT and Lafler-Kinman statistic). The lower panel of Fig. 5.2 shows an overlay of the completeness of the different detection criteria applied in case of Leo A with the cumulative completeness. The given example for amplitudes of 1 mag peak to peak show that the overall detection probability is dominated by the period search algorithm.

From the lower plot in Fig. 5.2 it is evident that the cumulative completeness is, as expected, dominated by the completeness of the Lafler-Kinman statistic. The other steps applied in the detection procedure do show a noticeable effect on the total completeness.

### 5.3.2 Results for DDO 216

For the completeness simulations of the DDO 216 dwarf galaxy a total of more than 3300 artificial stars were created, arranged on two different regular position grids overlapping the dwarf galaxy. Due to the larger apparent size of the dwarf the objects were distributed over the full field of view, the larger area used allowed for the use of only two different grids. Again these were shifted with respect to each other to avoid crowding of the artificial sources.

#### Variation mask completeness

Shown in the upper and the middle left panel of Fig. 5.3 are the results obtained for the completeness of the detection threshold applied on the variation mask. For 1 mag amplitude as shown, the average 50% completeness limit is approximately 23.5 mag. Table 5.3 lists the limits for all the five amplitudes analyzed.

	0.2 mag	0.6 mag	1 mag	1.4 mag	1.8 mag
Minimum	23.5	23.5	23.5	23.5	23.4
Average	23.5	23.5	23.5	23.5	23.5
Maximum	23.5	23.5	23.5	23.5	23.6

Table 5.3: Completeness limits for DDO 216 for the thresholding on the mask for variables as described in Sec. 5.3.2. Shown are the minimum, average and maximum 50% completeness limits in magnitudes over the period dimension of Fig. 5.3.

#### DAOPHOT completeness

Using the same sample of more than 3300 artificial stars the completeness of the DAOPHOT detection was tested. The 50% completeness limit lies at 23.9 mag. The full results are shown in the lower panel of Fig. 5.4.



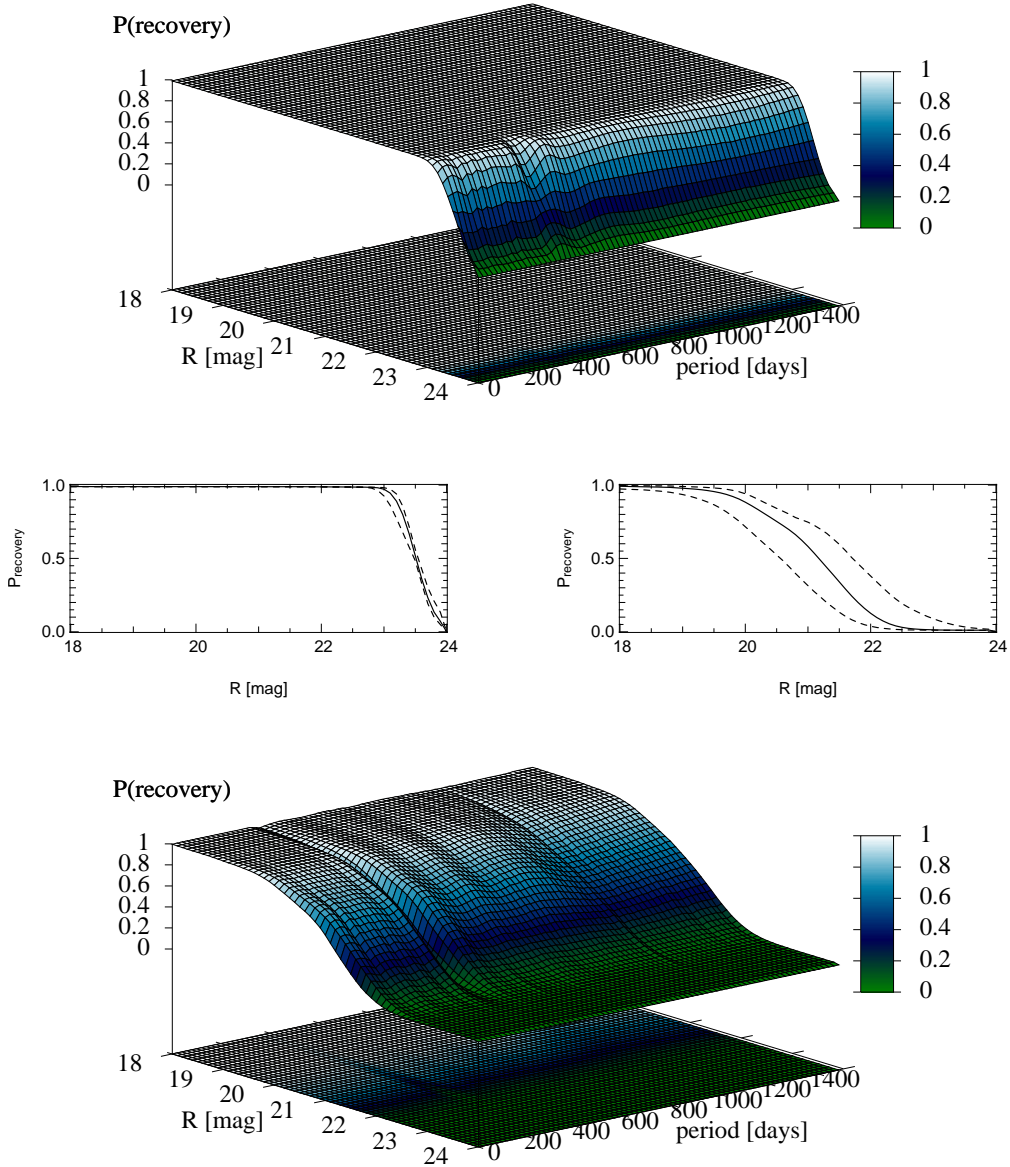


Figure 5.3: Results of the completeness simulations for the DDO 216 dwarf galaxy for artificial variables with 1 mag peak-to-peak amplitude. The upper, and the middle left-hand panel show the results for completeness of the variation mask selection, the middle right-hand and the lower panel the results for the Lafler-Kinman statistic. The plots in the middle row give the minimum, average and maximum completeness as a function of magnitude.

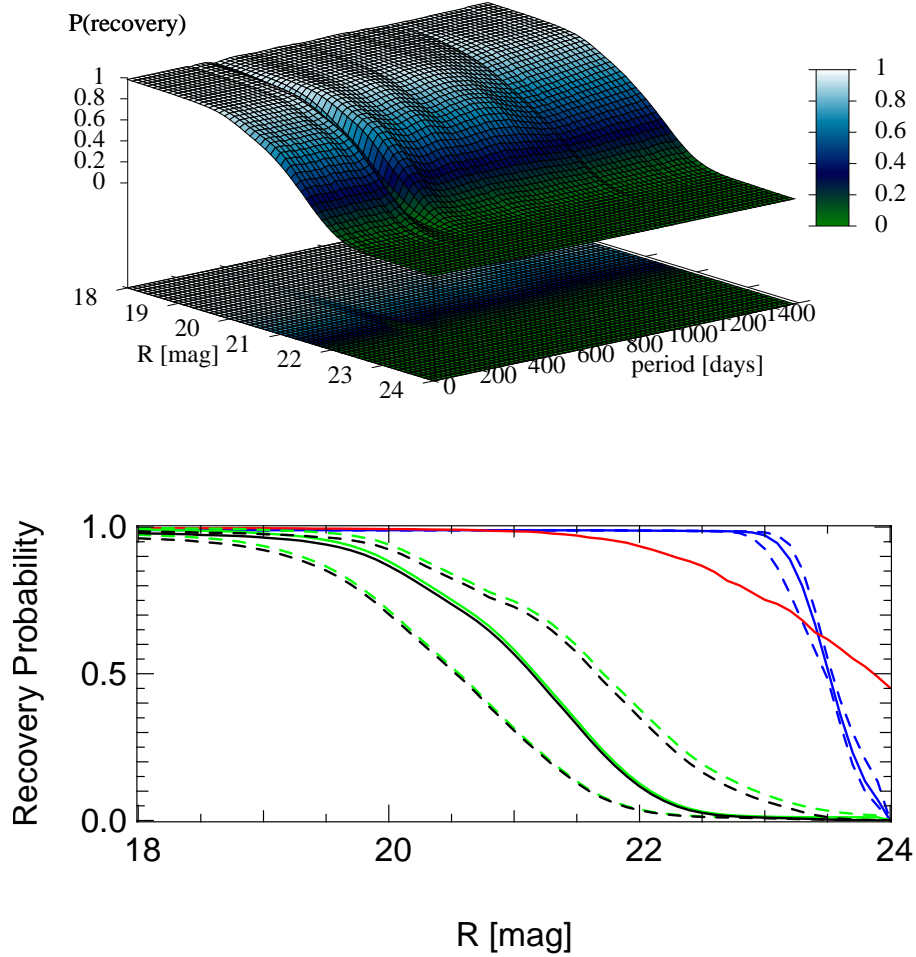


Figure 5.4: Results of the completeness simulations for the DDO 216 dwarf galaxy for artificial variables with 1 mag peak to peak amplitude. The upper panel shows the results for the cumulative completeness simulation, the lower one the minimum, average and maximum cumulative completeness (black) overlaid on the completeness of the variation mask (blue), the DAOPHOT detection (red) and the Lafler-Kinman statistic (green).

	0.2 mag	0.6 mag	1 mag	1.4 mag	1.8 mag
Minimum	18.9	19.9	20.6	21.1	21.5
Average	19.3	20.4	21.2	21.7	22.1
Maximum	19.6	20.9	21.7	22.3	22.7

Table 5.4: Completeness limits for the DDO 216 dwarf for the detection using the Lafler-Kinman statistic. Shown are the minimum, average and maximum 50% completeness limits in magnitudes over the period dimension of Fig. 5.3.

### **Lafler-Kinman completeness**

The middle right-hand and the lower panel in Fig. 5.3 show the completeness of the detection of artificial variable stars with 1 mag amplitude using the Lafler-Kinman statistic. The average 50% completeness limit as shown is approximately 21.2 mag. Table 5.4 lists these limits for all the five amplitudes analyzed.

The incompleteness for variables with periods around one year can be ascribed to the same reasons as described above. The lower overall completeness magnitude compared to Leo A stems from the smaller number of observed epochs.

### **Summary**

Like for Leo A a cumulative completeness of the three different completeness simulations was calculated by multiplying the different simulation results. The results are shown in Fig. 5.4. The top panel shows the cumulative completeness as a function of average variable magnitude and period, the lower one an overlay of the results from the different simulations with the cumulative results, collapsing the period dimension.

Again, the results are dominated by the completeness of the Lafler-Kinman statistic, with the variation mask and the DAOPHOT detection criterion not influencing the final results.

### **5.3.3 Results for GR 8**

The completeness simulations of the GR 8 dwarf galaxy were created applying a total of more than 800 artificial stars. These were arranged on two different regular position grids overlapping the visible dwarf galaxy. Again these were shifted with respect to each other to avoid unwanted crowding of the artificial sources.

### **Variation mask completeness**

Shown in the upper and the middle left panel of Fig. 5.5 are the results obtained for the completeness of the detection threshold applied on the variation mask. For 1 mag amplitude as shown, the average 50% completeness limit is larger than the maximum tested magnitude of 24.0. Table 5.5 lists the limits for all the five amplitudes analyzed.

### **DAOPHOT completeness**

Again using the same sample of artificial stars the completeness of the DAOPHOT detection was tested. The 50% completeness limit was found at 24.2 mag. The full results are shown in Fig. 5.6.

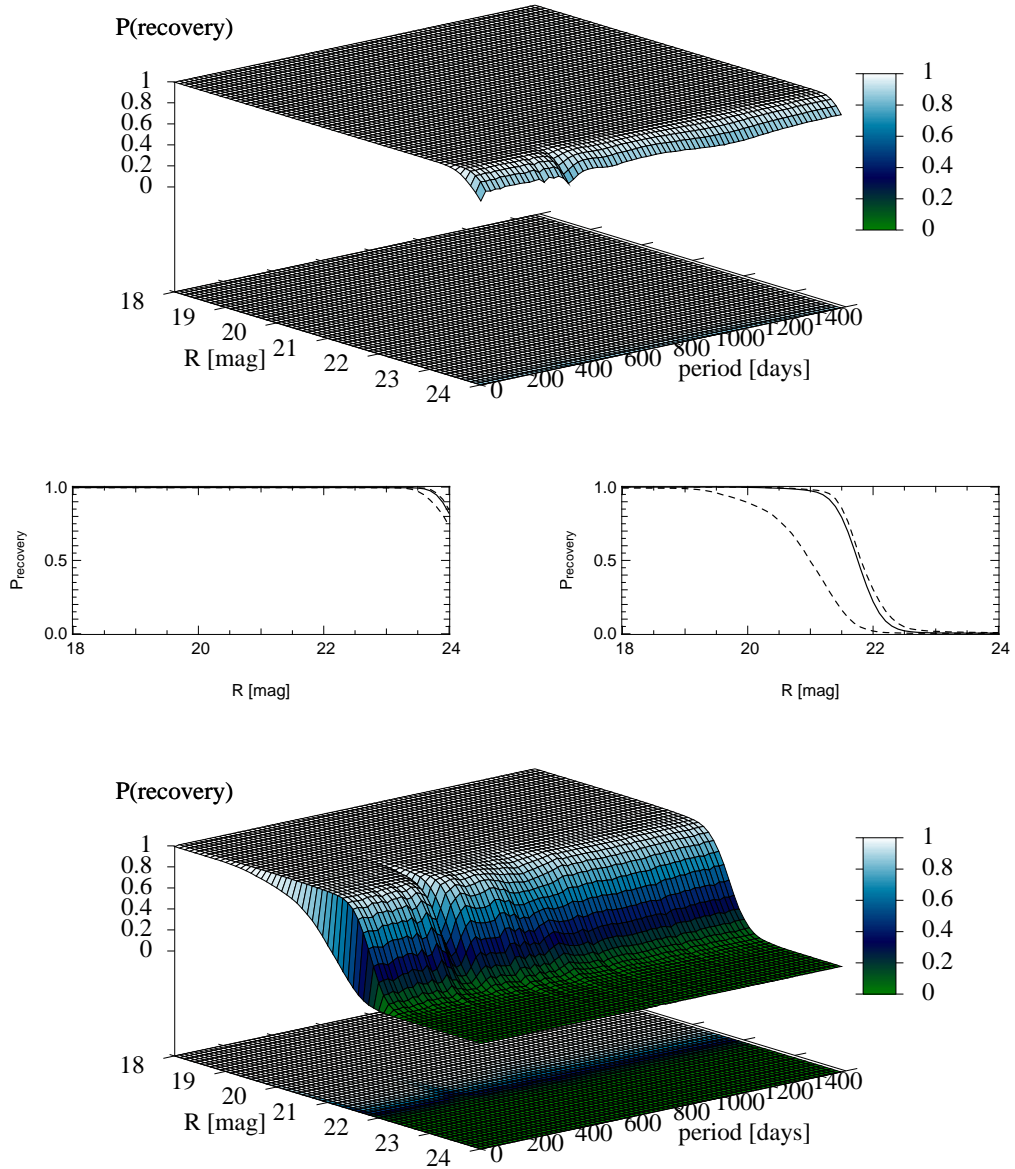


Figure 5.5: Results of the completeness simulations for the GR 8 dwarf galaxy for artificial variables with 1 mag peak-to-peak amplitude. The upper and the middle left-hand panel show the results for completeness of the variation mask selection, the middle right-hand and the lower panel the results for the Lafler-Kinman statistic. The plots in the middle row give the minimum, average and maximum completeness as a function of magnitude.

	0.2 mag	0.6 mag	1 mag	1.4 mag	1.8 mag
Minimum	> 24	> 24	> 24	> 24	> 24
Average	> 24	> 24	> 24	> 24	> 24
Maximum	> 24	> 24	> 24	> 24	> 24

Table 5.5: Completeness limits for GR 8 for the thresholding on the mask for variables as described in the caption of Fig. 5.5. Shown are the minimum, average and maximum 50% completeness limits in magnitudes over the period dimension of Fig. 5.5.

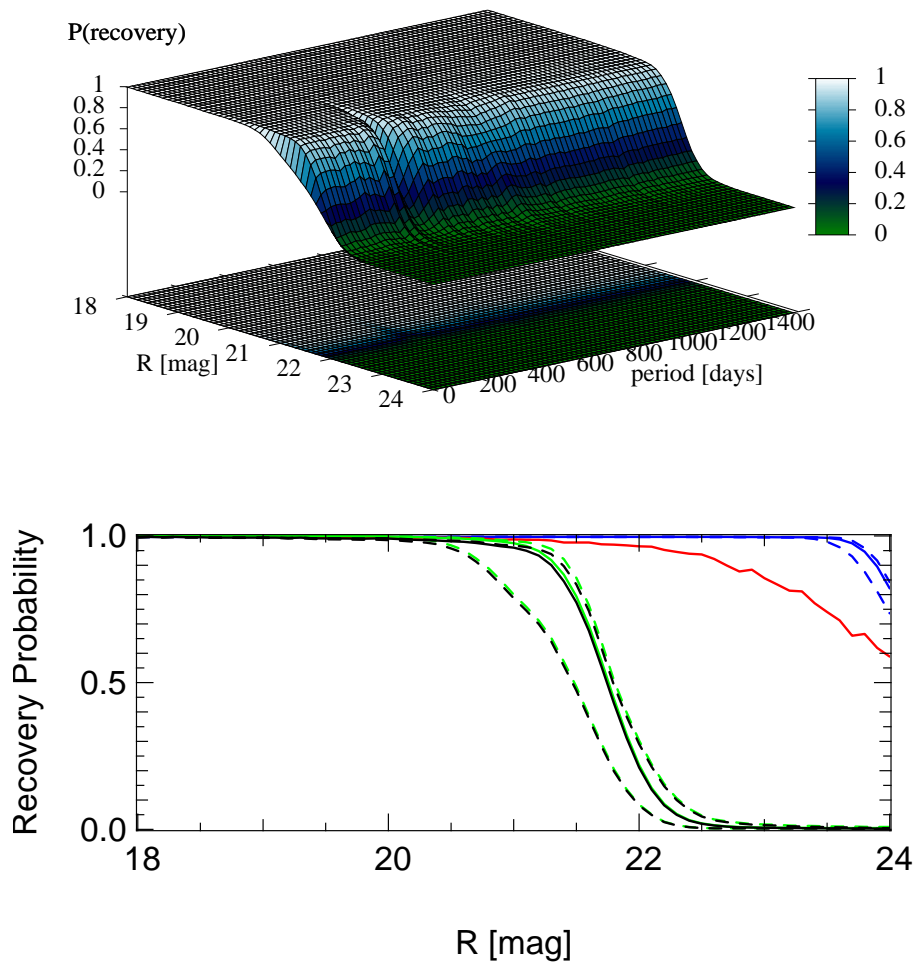


Figure 5.6: Results of the completeness simulations for the GR 8 dwarf galaxy for artificial variables with 1 mag peak to peak amplitude. The upper panel shows the results for the cumulative completeness simulation, the lower one the minimum, average and maximum cumulative completeness (black) overlaid on the completeness of the variation mask (blue), the DAOPHOT detection (red) and the Lafler-Kinman statistic (green).

	0.2 mag	0.6 mag	1 mag	1.4 mag	1.8 mag
Minimum	19.4	20.4	21.0	21.4	21.8
Average	20.1	21.2	21.8	22.1	22.4
Maximum	20.2	21.3	21.8	22.2	22.5

Table 5.6: Completeness limits for GR 8 for the detection using the Lafler-Kinman statistic. Shown are the minimum, average and maximum 50% completeness limits in magnitudes over the period dimension of Fig. 5.5.

### Lafler-Kinman completeness

The middle right and the lower panel in Fig. 5.5 show the completeness derived for the detection of artificial variable stars with 1 mag amplitude using the Lafler-Kinman statistic. The average 50% completeness limit as shown is approximately 21.8 mag. Table 5.6 lists these limits for all the five amplitudes analyzed.

The incompleteness for variables with periods around one year can be ascribed to the same reasons as described above.

### Summary

Applying the same methods as described above, the cumulative completeness was derived. The results are shown in Fig. 5.6. The top panel shows the cumulative completeness as a function of average variable magnitude and period, the lower one an overlay of the results from the different simulations with the cumulative results, collapsing the period dimension.

Again, the results are dominated by the completeness of the Lafler-Kinman statistic, with the variation mask and the DAOPHOT detection criterion not influencing the final results.

### 5.3.4 Results for DDO 210

For the completeness simulations of the DDO 210 dwarf galaxy a total of more than 1500 artificial stars were applied. These were arranged on two different regular position grids overlapping the visible dwarf galaxy. To avoid crowding of the artificial sources the two grids were shifted with respect to each other.

### Variation mask completeness

The results obtained for the completeness of the detection threshold applied on the variation mask are shown in the upper and the middle left panel of Fig. 5.7. The completeness limits for all five analyzed amplitudes are listed in Table 5.5. For 1 mag amplitude as shown in Fig. 5.7 the average 50% completeness limit is approximately 23.4 mag.



	0.2 mag	0.6 mag	1 mag	1.4 mag	1.8 mag
Minimum	23.4	23.4	23.4	23.4	23.5
Average	23.4	23.4	23.4	23.5	23.5
Maximum	23.4	23.4	23.5	23.5	23.6

Table 5.7: Completeness limits for DDO 210 for the thresholding on the mask for variables as described in the caption of Fig. 5.7. Shown are the minimum, average and maximum 50% completeness limits in magnitudes over the period dimension of Fig. 5.7.

### DAOPHOT completeness

The completeness of the DAOPHOT detection was tested using the same sample of artificial stars. The 50% completeness limit was found at 23.5 mag. The full results are shown in Fig. 5.6.

### Lafler-Kinman completeness

The middle right and the lower panel in Fig. 5.7 show the completeness derived for the detection of artificial variable stars with 1 mag amplitude using the Lafler-Kinman statistic. The average 50% completeness limit as shown is approximately 20.3 mag. Table 5.8 lists these limits for all the five amplitudes analyzed.

The prominent incompleteness for variables with periods with approximately one year and two years can be attributed to the Lafler-Kinman statistic and is further explained in the next section.

### Summary

Applying the same methods as described above, the cumulative completeness was derived. The results are shown in Fig. 5.8. The top panel shows the cumulative completeness as a function of average variable magnitude and period, the lower one an overlay of the results from the different simulations with the cumulative results, collapsing the period dimension.

The overall low achievable completeness limit, dominated by the results for the Lafler-Kinman statistic, might be surprising at first. Even though the number of available periods is larger than in case of the DDO 216 dwarf, the resulting completeness limit for DDO 210 is less faint. This and the strong occurrence of the incompleteness at periods of approximately one and two years has to be attributed to the spacing of the observed data and a peculiarity of the Lafler-Kinman statistic.

Even though more epochs are available, they are distributed over a larger timespan resulting in a larger spacing of the individual epochs. As the Lafler-Kinman statistic does not take into account the temporal spacing of the datapoints. With a larger spacing

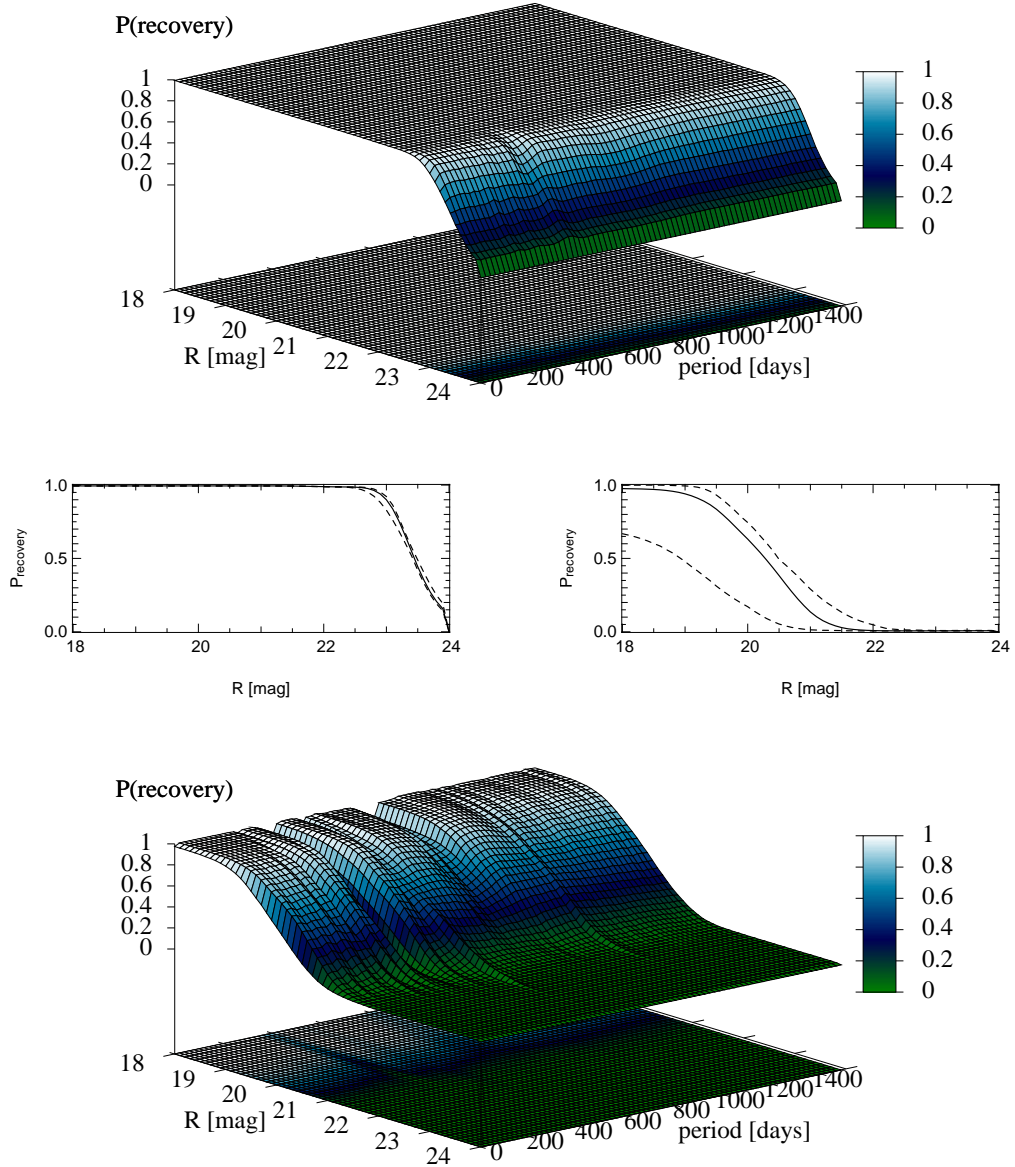


Figure 5.7: Results of the completeness simulations for the DDO 210 dwarf galaxy for artificial variables with 1 mag peak-to-peak amplitude. The upper and the middle left-hand panel show the results for completeness of the variation mask selection, the middle right-hand and the lower panel the results for the Lafler-Kinman statistic. The plots in the middle row give the minimum, average and maximum completeness as a function of magnitude.



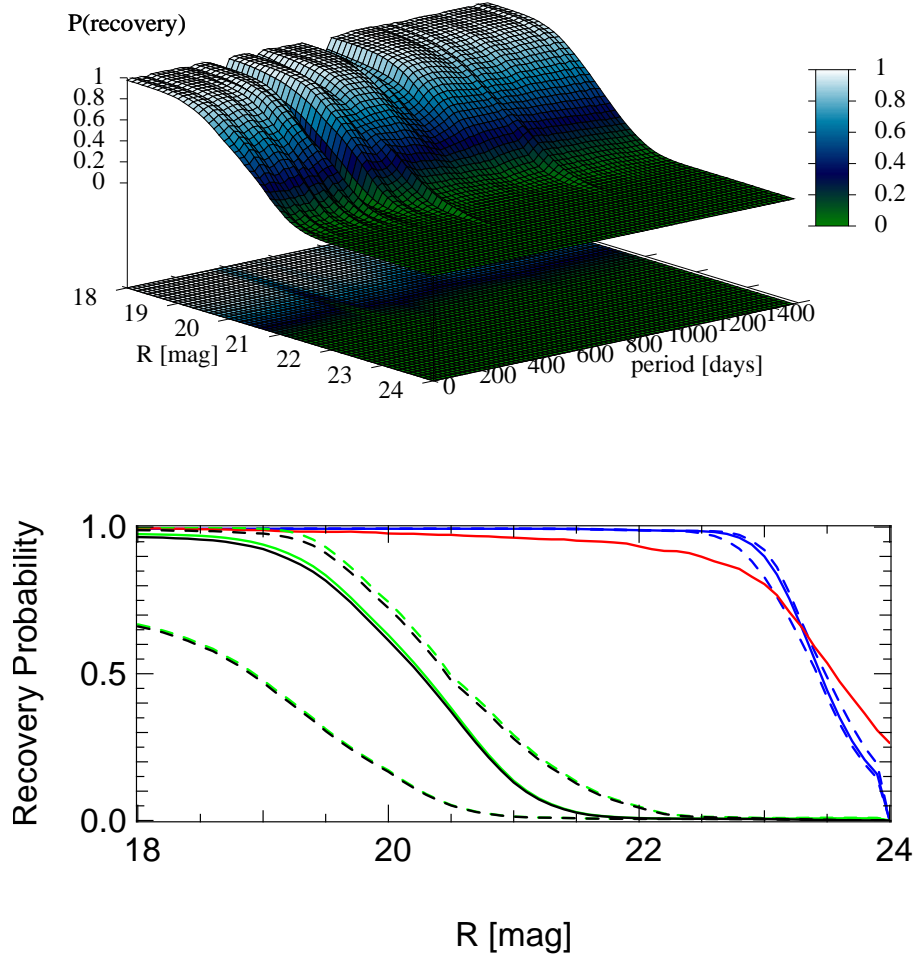


Figure 5.8: Results of the completeness simulations for the DDO 210 dwarf galaxy for artificial variables with 1 mag peak to peak amplitude. The upper panel shows the results for the cumulative completeness simulation, the lower one the minimum, average and maximum cumulative completeness (black) overlaid on the completeness of the variation mask (blue), the DAOPHOT detection (red) and the Lafler-Kinman statistic (green).

	0.2 mag	0.6 mag	1 mag	1.4 mag	1.8 mag
Minimum	18.1	18.6	18.9	19.9	20.5
Average	18.1	19.2	20.3	20.9	21.3
Maximum	18.8	19.5	20.5	21.1	21.6

Table 5.8: Completeness limits for DDO 210 for the detection using the Lafler-Kinman statistic. Shown are the minimum, average and maximum 50% completeness limits in magnitudes over the period dimension of Fig. 5.7.

the jumps between the datapoints perceived by the algorithm increase, finally resulting in a larger  $\Theta$  value. Combined with the  $\Theta$  limit of one used in the completeness simulations this leads to the observed decrease in the completeness limit.

The completeness of the thresholding on the variation mask, is less affected by the spacing of the datapoints, the results are comparable with those for the DDO 216 dwarf galaxy. Once more both, the variation mask and the DAOPHOT detection criterion are not influencing the final results.

Another reason for the low achievable completeness limit can be found in the celestial of DDO 210 with a declination of  $-12^\circ$  all the observations are obtained at relatively large airmasses  $> 1.5$ . The resulting loss of light affects the completeness limits as well.

## 5.4 Summary

The simulations have shown that the completeness to recover an artificial variable from the data is completely dominated by the Lafler-Kinman statistic. The influence from two other selection criteria applied, the thresholding on the variation mask and the need for a source detection in the reference image using DAOPHOT, can be considered negligible.

The limiting magnitude of the Lafler-Kinman statistic itself is, as expected, dominated by the number of available epochs, and as shown for the DDO 210 dwarf, by the spacing of the observations. It should be noted that the completeness along the period axis of the tested parameter space shows no deficiencies in the tested range. Apart from a small weakness in the detection of variables with a period of about one year, the Lafler-Kinman statistic proves to be a very useful tool in the search for long period variables.

The differences found in the depth of the different completenesses for the different dwarf galaxies might be puzzling at first, the completeness for the variation mask for Leo A is deeper than the one found for DDO 216, yet for the DAOPHOT completeness the two results are the other way around. This behavior can be explained easily. The variation mask completeness depends on the number of observed epochs (94 for Leo A and 69 for DDO 216). The DAOPHOT completeness on the other hand is a function of the depth and the quality of the reference image.

Recapitulating it should be noted that completeness of our sample of variable sources is not limited by the period. The amplitude of the variability on the other hand could have a much broader impact on the final results. The limit varies up to  $\sim 3$  mag between the smallest and the largest amplitudes tested. The types of variables searched for in the context of this work, Mirae and SRa, both show typically large amplitudes of at least 1 mag peak to peak variation. The degradation of the results when going towards smaller amplitudes should not affect the results presented here significantly. But when studying the variety of the different classes of period variables found, one would need to take this incompleteness carefully into account.

## Chapter 6

# Conclusions about the stellar populations

Long period variables can be used as a valuable tool to derive clues about the composition of the stellar populations of a galaxy. In this chapter the LPV content of the analyzed dwarf galaxies is used to procure hints about the the stellar populations of the dwarfs and their corresponding star formation histories. These results will be compared with the relevant published literature.

### 6.1 LPVs and AGB stars as tracers of the stellar populations

In the introduction the stellar evolution from the main sequence onto the thermally pulsing AGB (TPAGB) was described. A significant portion of these AGB stars starts to pulsate on long timescales. The lifetime of the star spent on both the AGB and the LPV phase is relatively short, in the order of  $10^5$  years (Vassiliadis & Wood, 1993; Renzini & Fusi Pecci, 1988). This makes them excellent age tracers for stellar populations.

#### 6.1.1 LPVs as tracers of the relative contribution of the population, the fuel consumption theorem

The presence of numerous blue stars can be considered a sign of a relatively young population or still ongoing star formation. The occurrence of LPVs on the other hand is commonly regarded as a tracer of an intermediate age population of approximately 1 – 10 Gyrs (e.g. Caldwell *et al.*, 1998). The stars still remaining from even older populations are not massive enough to reach the TPAGB and enter the Mira phase. This distinct characteristic makes it possible to trace the underlying stellar population. Once the complete number of long period variables is known (hence the need for completeness simulations), it can serve as a measure of the proportion this intermediate age

population has on the total stellar mass of the galaxy. This can be achieved following the procedure developed by [Renzini \(1998\)](#).

The originating stellar population of the LPVs can be described simplest as a simple stellar population (SSP). An SSP, describes a group of stars of same age created during a single burst of stellar formation.

Such an SSP is fully described by three parameters, age, chemical composition and the initial mass function (IMF). The IMF  $\xi(M)$  describes the distribution of the different masses amongst the created stars. After the burst there will be

$$dN = A\xi(M)dM \quad (6.1)$$

stars created in the mass range  $[M, M + dM]$  with normalization constant  $A$  depending on the actual  $\xi(M)$  used and the magnitude of the burst, often expressed by the bursts star formation rate in  $M_{\odot} \text{ yr}^{-1}$ .

The IMF can be described as a power-law

$$\xi(M) \propto M^{-\alpha}. \quad (6.2)$$

The slope parameter  $\alpha$  is commonly adopted as 2.35 following the classic study by [Salpeter \(1955\)](#).

Starting with the initial burst, the created stars will evolve according to their mass and with increasing age more and more stars evolve away from the main sequence (MS) onto the various post-MS phases and finally die as white dwarfs or supernovae.

The mass of a star at the turn-off (TO) from the main sequence  $M_{TO}(t)$  for a given time can be derived from analytic models of stellar evolution. Setting the time spent on the post-MS phases as  $t_{PMS}$ , the mass of a star just ceasing its thermonuclear burning is  $M_D \simeq M_{TO}(t - t_{PMS})$ . At any time stars with masses less than  $M_{TO}$  will be still burning hydrogen in the core, stars with masses between  $M_{TO}$  and  $M_D$  evolve through the post-MS phases and the stars with masses larger  $M_D$  are dead stellar remnants.

[Renzini \(1994\)](#) showed that the masses of all evolved stars can be assumed to be approximately the same, i.e.  $M_i \simeq M_{TO} \simeq M_D$  and that the rate at which stars leave the main sequence and evolve onward is defined by the *evolutionary flux*  $b(t)$  of the population

$$b(t) = \xi(M_{TO})|\dot{M}_{TO}| \quad (6.3)$$

in stars per years. The IMF represents the pool of stars still remaining,  $|\dot{M}_{TO}|$  is the *evolutionary clock* of the stellar population denoting the rate at which the pool drains. Following [Renzini \(1994\)](#) the number of stars in a given post-MS phase  $i$ ,  $N_i$  is proportional to the time spent in that specific phase  $t_i$ :

$$N_i = b(t)t_i. \quad (6.4)$$

The total luminosity  $L_T$  of the observed stellar population can be estimated as

$$L_T(t) \simeq 10^{11} k' b(t) F_T(M_{TO}) \quad (6.5)$$

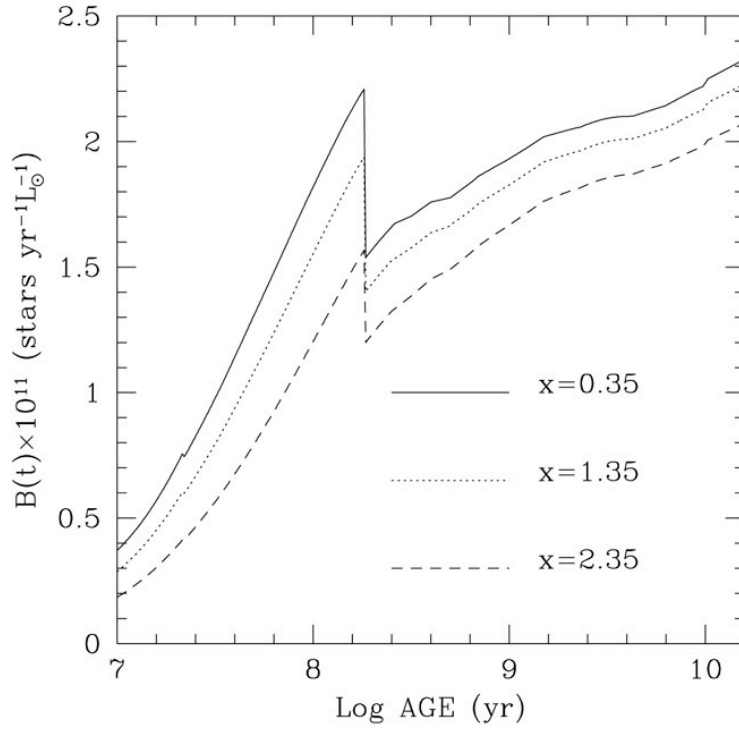


Figure 6.1: Graphic from [Renzini \(1998\)](#). “Specific evolutionary flux (i.e. the number of stars evolving off the main sequence per year and per unit [solar] luminosity of the parent stellar population) for three values of the slope of the initial mass function, as indicated. The sharp discontinuity at  $\sim 10^6$  yr is caused by the appearance of an extended TP-AGB phase.”

with the coefficient  $k' = \frac{L_T}{L_{PMS}}$  and the total *fuel consumption*  $F_T = \sum_i F_i(M_{TO})$ . The inverse of the relative contribution of the post-MS stars  $k'$  is a slow function of age.  $F_i$ , the fuel consumption, is a measure of the nuclear fuel burned in the  $i$ -th phase after the main sequence.

Dividing the evolutionary flux from Equation (6.3) by the total luminosity (Equation (6.5)) one gets the *specific evolutionary flux* ([Renzini, 1994, 1998](#); [Renzini & Buzzoni, 1986](#); [Renzini & Fusi Pecci, 1988](#))

$$B(t) = \frac{b(t)}{L_T(t)} \simeq \frac{10^{-11}}{k' F_T} \quad (6.6)$$

The second part of Equation (6.6) shows that the specific evolutionary flux is independent of the IMF and furthermore almost independent of the age, as  $F_T$  does not change much with the stellar mass.

Applying Equation (6.6) to Equation (6.4) one gets

$$N_i = B(t) L_T t_i. \quad (6.7)$$

This equation proves to be extraordinarily useful for the analysis of observational data. It allows to predict the number of stars in a given post-MS evolutionary phase expected for an actually observed sample, giving the number relative to the total observed luminosity.  $L_T$  can be acquired directly from the data. The observed flux is summed up and the apparent magnitude  $m_i$  in the filter band  $i$  calculated. Given that the distance is known, the absolute magnitude  $M_i$  can be derived and using published bolometric corrections (e.g. [Maraston, 1998](#)) transformed into the bolometric magnitude  $M_{bol}$ . From this the absolute bolometric luminosity can then be calculated. A comparison of the observed numbers of e.g. LPVs with the predicted number yields the relative contribution of the stellar population to the total galaxy.

### 6.1.2 Application to the data

To obtain the total luminosity of the respective dwarf galaxy first a zero-one mask is applied to the reference frame to mask out the surroundings of the dwarf galaxy. The remaining flux is assumed to come from the dwarf galaxy and the total apparent flux of the dwarf can simply be calculated by summing up the fluxes  $f_i$  of individual pixels  $i$ . This combined flux is then converted into the absolute magnitude  $M_F$  in the filter band  $F$  by applying the respective calibration zeropoint  $zp_F$ , the distance modulus  $dmod$  and correcting for the galactic extinction  $e_{gal}$  following [Schlegel et al. \(1998\)](#).

$$M_F = -2.5 \log \left( \sum_i f_i \right) + zp_F + dmod + e_{gal} \quad (6.8)$$

This is then translated into the absolute bolometric magnitude  $M_{bol}(t)$  using the bolometric correction  $BC_F(t)$  for the filter band  $F$  using the data published by [Maraston \(1998\)](#).

$$M_{bol}(t) = M_F + BC_F(t) \quad (6.9)$$

It should be noted that the bolometric correction already is a function of the age of the assumed stellar population. Adopting an absolute bolometric magnitude of the sun  $M_{\odot,bol}$  of 4.72 the total luminosity of the dwarf galaxy  $L_T(t)$  is

$$\frac{L_T(t)}{L_{\odot}} = 10^{-0.4(M_{bol}(t)-4.72)} \quad (6.10)$$

To obtain an upper limit for the contribution of the stellar population to which the LPVs belong,  $L_T$  is applied to Equation (6.7). For  $t_i$  the values published by [Vassiliadis & Wood \(1993\)](#) are used. Unfortunately the lowest metallicity for which they specify the ages for their complete range of masses is  $Z = 0.004$ . For the calculations this  $Z$  will be used even though the actual metallicities of the analyzed dwarfs are lower than this value. In the following the predicted number of TPAGB stars will be given for discreet ages, as the [Vassiliadis & Wood \(1993\)](#) published their results only for a couple of ages. This could be deemed sufficient for estimating the ages of the different contributing populations.

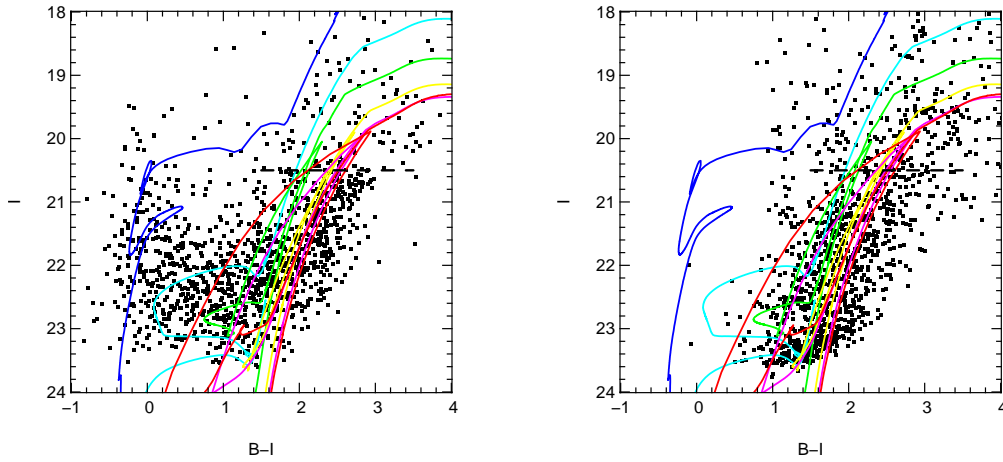


Figure 6.2: Color magnitude diagrams for Leo A constructed from the  $B$  and  $I$ -band data obtained at Calar Alto. The left panel shows the results for the visible dwarf galaxy, the right one the stars in the surrounding field. Over-plotted are the isochrones for ages between 0.1 and 14 Gyrs (0.1 - blue, 0.5 - cyan, 1.0 - green, 5.0 - yellow, 10 - magenta, 14 - red) using the tracks by Pietrinferni *et al.* (2004). The  $I$ -band magnitude of TRGB at  $I = 20.5$  from Schulte-Ladbeck *et al.* (2002) is indicated by the dashed line.

The remaining problem in the estimating the relative contribution of the originating population of the LPVs is the lack of a prediction for a percentage of the stars on the TPAGB which are visible LPVs at a given time. Renzini (1998) and Renzini & Fusi Pecci (1988) found for the 15 Gyr old population of solar metallicity in the globular cluster 47 Tuc the number of LPVs to be approximately  $\frac{1}{4}$  of the number of TPAGB stars. Rejkuba *et al.* (2003) conclude that from their sample of near-IR selected AGB stars in NGC 5128 26 – 70% are variable. For M32, Davidge & Rigaut (2004) found 60% of the bright AGB stars to be variable. In the following the  $\frac{1}{4}$  from Renzini will be used and in addition an empirically chosen upper limit of  $\frac{1}{2}$ . It should be kept in mind that a part of the LPVs can be lost from the sample by excessive dust extinction in the stars themselves. This dust can reduce the light emitted in the optical so far that the stars drop below the achieved detection limits.

## 6.2 Leo A

In the case of Leo A, the mask image (see the left panel of Fig 6.3) can be used as well to compare the stellar populations found within the optically prominent part of the dwarf galaxy and the surrounding area. The elliptical mask used traces approximately the Holmberg radius. To select the surrounding area the bright foreground star was masked out in addition to the use of the inverse mask.

Fig. 6.2 shows the  $I$ -band against  $(B - I)$  color-magnitude diagrams for Leo A. Over-plotted are isochrones (Pietrinferni *et al.*, 2004) for simple stellar populations

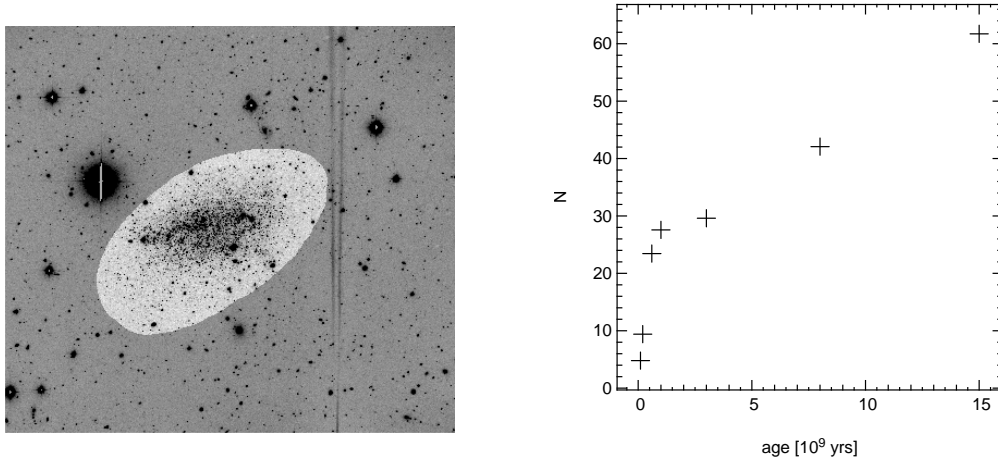


Figure 6.3: *Left panel:* The mask used to select flux from the Leo A dwarf galaxy overlaid on the Calar Alto reference frame. *Right panel:* The number of stars on the TPAGB as predicted by the fuel consumption theorem.

with a metallicity  $Z = 0.0003$  and ages between 0.1 and 14 Gyrs.

The left panel shows the stars within the mask, i.e. those part of the prominent part of the dwarf. It shows a significant young, blue population. Comparison with the [Pietrinferni \*et al.\* \(2004\)](#) isochrones suggest an age of that population within a range between 0.3 and 1 Gyr. In addition the clearly visible red-giant branch points toward an intermediate-age population with an age older than two Gyrs. The tip of the red-giant branch at  $I = 20.5$  seen in this diagram nicely agrees with the results found by [Schulte-Ladbeck \*et al.\* \(2002\)](#).

These findings are in agreement with the work by [Schulte-Ladbeck \*et al.\*](#) They used to deep HST imaging to obtain a deep color-magnitude diagram and compared these with different synthetic CMDs created using theoretical isochrones to reconstruct the star-formation history of Leo A. Their best fitting SFH shows the different epochs of star-formation resulting in a young population formed 0.2 to 0.8 Gyrs ago, an intermediate age population approximately 2 to 4 Gyrs old and an old 10 Gyr old one.

As shown above, the comparison with the theoretical isochrones presented here finds the young population and an older one, compatible with the results of [Schulte-Ladbeck \*et al.\*](#) The simple comparison method used here is not sensitive enough to discern between the two old populations or limit the age of the young population further. The depth and resolution of the obtained color-magnitude diagram are not sufficient to make a comparison with a synthetic one a viable attempt.

To reconstruct the age of the population traced by the LPVs the fuel consumption theorem (Sec. 6.1) can be applied. Summing up all the flux within the mask shown in the left panel of Fig. 6.3 applying the respective zeropoint calibration and adopting the distance modulus of 24.5 from [Schulte-Ladbeck \*et al.\* \(2002\)](#), the total luminosity  $L_T$  can be calculated using Equation (6.10). Depending on the age of the stellar population the total luminosity of Leo A is in the range  $1.7 \times 10^5 L_\odot$  to  $3.2 \times 10^5 L_\odot$ . In the right



panel of Fig. 6.3 we show the resulting numbers of stars on the TPAGB obtained by applying Equation (6.7) and the ages of stars with a metallicity of  $Z = 0.004$  on the TPAGB from Vassiliadis & Wood (1993).

The 11 LPVs found (see Sec. 4.4.1) can be adopted to be the full content. This is a reasonable attempt, assuming that all LPVs are brighter than the TRGB, since the completeness simulation (Sec. 5.3.1) show that the detection is complete to magnitudes well below the TRGB.

Comparing this with the results shown in the right panel of Fig. 6.3 (taking into account the  $\frac{1}{4}$  assumption described above) it is clear that a young population with an age up to 3 Gyrs can not be dominant in Leo A. On the other hand the number of LPVs can be explained either by a pure 15 Gyr old population or a combination with a younger one. Schulte-Ladbeck *et al.* (2002) proposed a  $\simeq 50\%$  contribution by a very old ( $> 10$  Gyr) population. The findings shown here are in excellent agreement with this. A combination of a 50% contribution from an very old population, combined with a  $\sim 3$  to 5 Gyr old one and a small contribution (in terms of LPVs) from a young one can in fact be used to explain the number of LPVs found in this project.

Vansevičius *et al.* (2004) found in deep wide field imaging data of Leo A clues for the presence of an extended old stellar halo extending beyond the Holmberg radius of Leo A. They find their result supported by Dolphin *et al.* (2002) whose “suspected Leo A RR Lyr variable C1-V01 [...] is located just outside the ellipse marking the galaxy size, confirming the old age and large extend of the discovered stellar halo” (Vansevičius *et al.*, 2004). The distribution of stars in the color-magnitude diagram constructed from the Calar Alto  $B$  and  $I$ -band data for the field surrounding Leo A, shown in the right panel of Fig. 6.2 could support an old ( $> 10$  Gyr) population in the outer fields of Leo A. The complete lack of LPVs in that region, as noted in Sec. 4.4.1 puts further constraints on the age of the population, defining it as a very old one, assuming Poisson error statistics for the LPV counts.

## 6.3 DDO 216

In the case of DDO 216 the lack of images in the  $B$  and  $I$ -band makes it impossible to use our data to create a color-magnitude diagram. Instead an  $I$  against  $(V - I)$  color-magnitude diagram constructed from the HST data published by Holtzman *et al.* (2003). This CMD is shown in Fig. 6.4. Over-plotted are the tracks from Pietrinferni *et al.* (2004) for stellar population with ages between 0.15 and 14 Gyrs and a metallicity of  $Z = 0.004$ .

Aparicio & Gallart (1995) proposed a metallicity of  $Z = 0.008$  and later refined the value to  $Z = 0.002$  (Aparicio *et al.*, 1997a). Gallagher *et al.* (1998) found their observations to be compatible with a metallicity as low as  $Z = 0.001$ . In a comparison of the color-magnitude diagram with the isochrones for different metallicities the isochrones with a metallicity of  $Z = 0.004$  showed the best agreement with the features present in the CMD. It shows the main sequence from a 0.15 Gyr old population (see the left

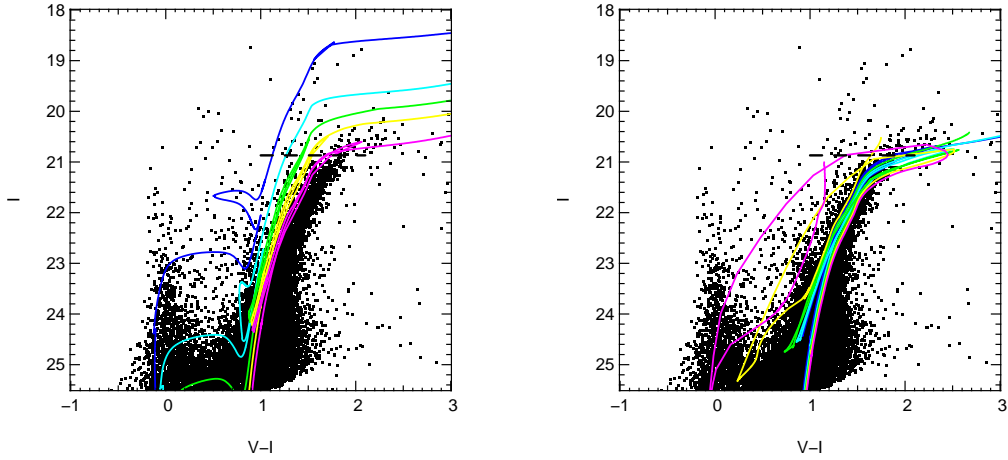


Figure 6.4: Color magnitude diagrams for DDO 216 constructed from the  $V$  and  $I$ -band HST data published by Holtzman *et al.* (2003). Over-plotted are isochrones for ages between 0.15 and 14 Gyrs using the tracks from Pietrinferni *et al.* (2004) for a metallicity of  $Z = 0.001$ . Shown in the left panel are isochrones for stellar populations with ages of 0.15 (blue), 0.5 (cyan), 1 (green), 2 (yellow), and 4 Gyrs (magenta), in the right one for ages 6 (blue), 8 (cyan), 10 (green), 12 (yellow) and 14 Gyrs (magenta). The  $I$ -band magnitude of the TRGB at  $I = 20.87$  from McConnachie *et al.* (2005) is indicated by the dashed line.

panel of Fig. 6.4). The age of the population linked to the well populated red giant branch cannot be determined with certainty. The RGB can most probably be attributed to an intermediate age population with an age in the range between 6 and 10 Gyrs (see the right panel of Fig. 6.4).

To compare these results with the variable star content, the fuel consumption theorem was applied once more. To minimize the contamination by bright foreground stars, these were masked out, as shown in the left panel of Fig. 6.5. Summing up all the remaining flux and applying the respective zeropoint calibration and adopting the distance modulus of 24.85 from McConnachie *et al.* (2005) the total luminosity  $L_T$  can be calculated following Equation (6.10). Taking the age of the stellar population as a variable the total luminosity ranges from  $4.7 \times 10^5 L_\odot$  to  $8.7 \times 10^5 L_\odot$ . Applying Equation (6.7) and the ages of stars with a metallicity of  $Z = 0.004$  on the TPAGB from Vassiliadis & Wood (1993) the numbers of stars expected on the TPAGB can be calculated and are shown in the right panel of Fig. 6.5.

Gallagher *et al.* (1998) found a prominent red giant branch (RGB) and a well-populated red clump (RC) using deep HST imaging. Using these data they constructed artificial color-magnitude diagrams and concluded that the majority of the stars visible were formed 2 – 6 Gyrs ago. They excluded the option of a dominant young population with an age  $< 1$  Gyr, but they cannot exclude a contribution from an old  $> 10$  Gyr population.

Comparing this with the results shown in the right panel of Fig. 6.5, it is obvious

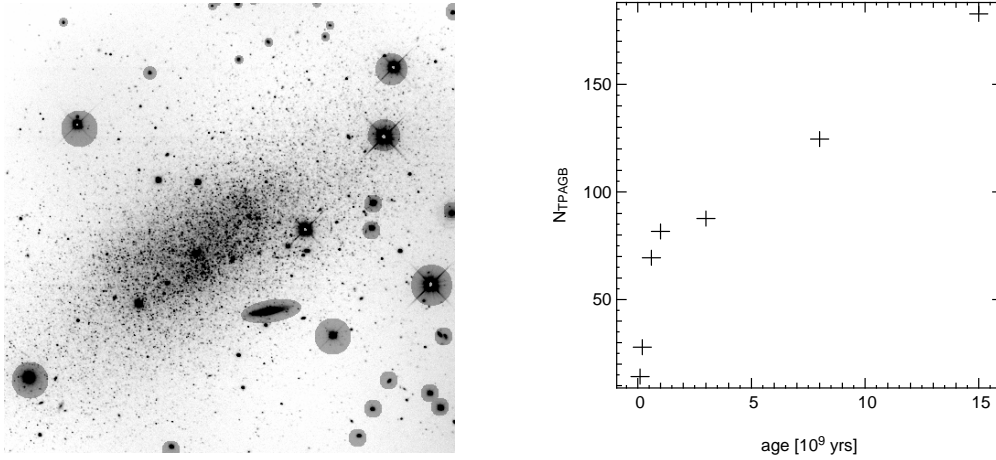


Figure 6.5: *Left panel:* The mask used to mask foreground stars from the field of view of the DDO 216 dwarf galaxy overlaid on the reference frame. *Right panel:* The number of stars on the TPAGB as predicted by the fuel consumption theorem.

that the data shown here exclude a dominant young population as well, given that a total of 52 LPVs were found. Again assuming the ratio between LPVs and TPAGB stars from [Renzini \(1998\)](#) and [Renzini & Fusi Pecci \(1988\)](#) used above, an intermediate age population in the range 2 – 8 Gyrs can explain the number of LPVs, yet a small contribution from an even older population cannot be excluded.

The comparison of the HST color-magnitude diagrams with the isochrones from [Pietrinferni \*et al.\*](#) shows a strong intermediate age population and a small contribution by a young one. The numbers of LPV stars predicted for DDO 216, again assuming a ratio of  $\frac{1}{4}$ , are compatible with a 15 Gyr old population combined with a 0.5 and a 1 Gyr one as well, but such a combination would be in disagreement with the results obtained from the color-magnitude diagrams.

## 6.4 GR 8

In case of GR 8 the low number of variable sources, only two LPVs were found, makes judgments about the stellar populations difficult. This low number can be explained by the large distance of the galaxy (2.2 Mpc) and the resulting large distance modulus. As a result, the resulting catalog of variable sources has to be considered incomplete, a finding supported by the completeness simulations.

Fig. 6.6 shows the color-magnitude based on HST data published by [Holtzman \*et al.\*](#) (2003). Over-plotted are isochrones for a metallicity of  $Z = 0.001$  from [Pietrinferni \*et al.\*](#) (2004) for ages in the range from 0.05 to 14 Gyrs. The color magnitude diagram of the stars in the dwarf galaxy shows a young population possibly as young as 50 Myrs and traces of an RGB with an age of about 5 to 10 Gyrs. The dashed line at an *I*-band magnitude of 22.7 shows the TRGB magnitude found by [Dohm-Palmer \*et al.\*](#)

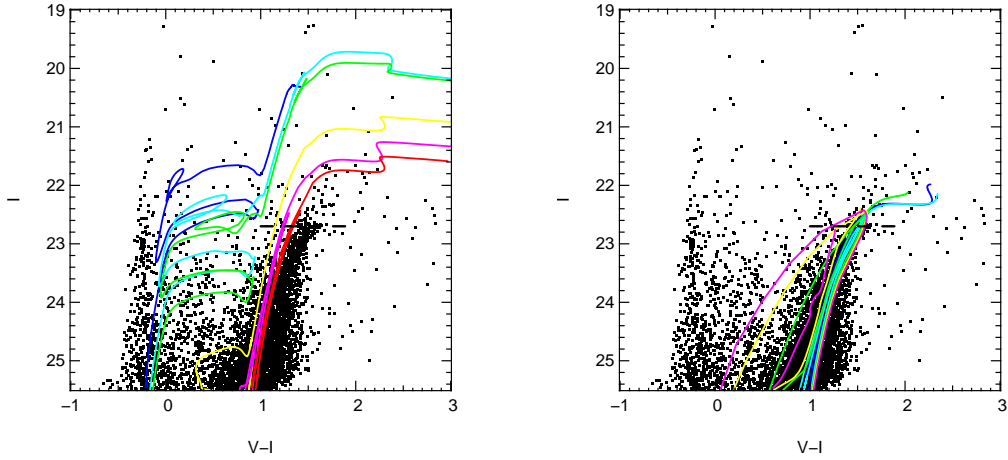


Figure 6.6: Color magnitude diagrams for GR 8 constructed from HST data published by Holtzman *et al.* (2003). Over-plotted are isochrones for ages between 0.05 and 14 Gyrs using the tracks from Pietrinferni *et al.* (2004). The left panel shows the isochrones for populations with ages of 0.05 (blue), 0.08 (cyan), 0.11 (green), 0.5 (yellow), and 1 Gyrs (magenta), the right one for ages of 5 (blue), 8 (cyan), 10 (green), 12 (yellow) and 14 Gyrs (magenta). The  $I$ -band magnitude of the TRGB at  $I = 22.7$  from Dohm-Palmer *et al.* (1998) is indicated by the dashed line.

(1998) which is in good agreement with the data presented here. These conclusions about the recent star formation history are in agreement with the results Dohm-Palmer *et al.* (1998) obtained from HST data.

The results for the application of the fuel consumption theorem are shown in the right panel of Fig. 6.7. The left panel shows the mask used to select the light originating from the galaxy overlaid on the Wendelstein reference frame.

Even accounting for the incompleteness of the catalog of variable stars, it is obvious that the light recorded cannot originate from an old population. The finding of just two LPVs in the dataset supports the result from the analysis of the color-magnitude diagram presented above that the galaxy is dominated by a young population. These results are in good agreement with Dohm-Palmer *et al.* (1998) who found a young population with an age of up to 0.5 Gyrs using synthetic models of their well-resolved color-magnitude diagram. Unfortunately they did not specify relative contributions for the various populations.

## 6.5 DDO 210

In the DDO 210 dwarf galaxy no variable sources were found at all. Considering the distance modulus of  $m - M = 25.15$  from McConnachie *et al.* (2005) and the calculated completeness limit, this paucity is surprising. While the achievable completeness limit is not as deep as one would hope, but it should still be sufficient to detect at least some long period variables.

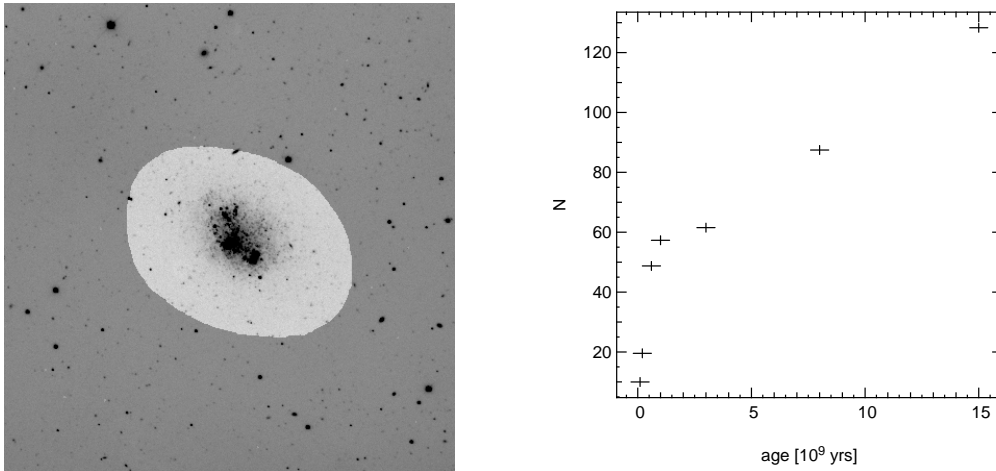


Figure 6.7: *Left panel:* The mask used to select flux from the GR 8 dwarf galaxy overlaid on the Wendelstein reference frame. *Right panel:* The number of stars on the TPAGB as predicted by the fuel consumption theorem.

Fig. 6.8 shows the color-magnitude diagrams based on the HST data published by Holtzman *et al.* (2003) with theoretical isochrones from Pietrinferni *et al.* (2004) for two different metallicities ( $Z = 0.008$  in the left panel,  $Z = 0.0003$  in the right panel) overplotted. The color-magnitude diagrams for this dwarf galaxy show an excellent example of the age-metallicity degeneracy sometimes plaguing the study of stellar populations with color-magnitude diagrams. The red giant branch could either be explained by a 0.5 Gyr old population with a metallicity of  $Z = 0.008$ , a 10 Gyr old population with a metallicity of  $Z = 0.001$  (not shown) or a 12 to 14 Gyr population with a metallicity as low as  $Z = 0.0003$ . The last one would be in agreement with McConnachie *et al.* (2005) who found a metallicity of  $Z = 0.0003$ . The color-magnitude diagram shows in addition a small contribution from a very young population.

The results for the application of the fuel consumption theorem are shown in the right panel of Fig. 6.9. The left panel shows the mask used to select the light originating from the galaxy overlaid on the Wendelstein reference frame.

The complete lack of variable sources can be brought into agreement with the predictions from the fuel consumption theorem and the study of the color-magnitude diagrams by assuming a dominant very old population and a low metallicity. A very old population could be so old that all sufficiently massive stars already evolved past the AGB phase. The contribution by the young population is too small to produce a detectable amount of LPVs. An old population with low metallicity would be in agreement with McConnachie *et al.* (2005).

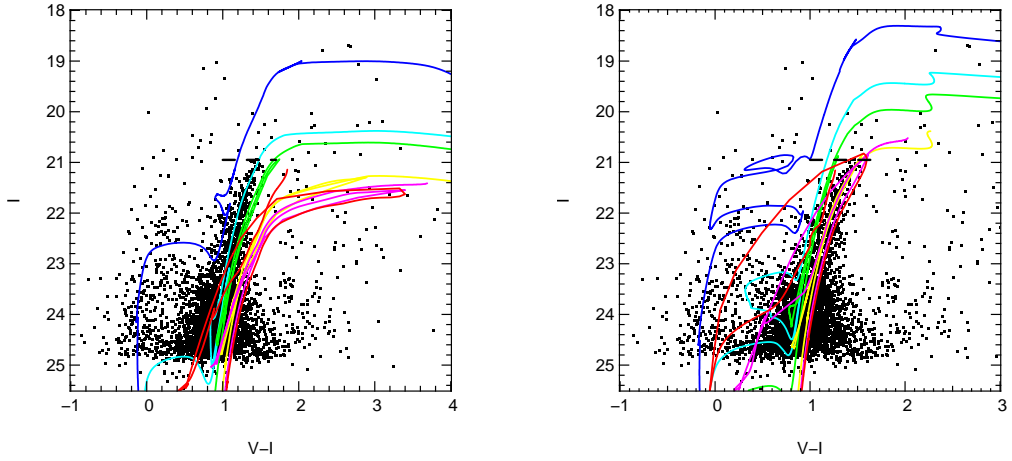


Figure 6.8: Color magnitude diagrams for DDO 210 constructed from HST data published by Holtzman *et al.* (2003). The left panel shows overplotted the isochrones from Pietrinferni *et al.* (2004) for a metallicity of  $Z = 0.008$ , the right one for  $Z = 0.0003$ . The ages of the plotted isochrones are 0.1 (blue), 0.5 (cyan), 1, (green), 5, (yellow), 10 (magenta) and 14 Gyrs (red). The  $I$ -band magnitude of the TRGB at  $I = 20.95$  from Lee *et al.* (1999) is indicated by the dashed line.

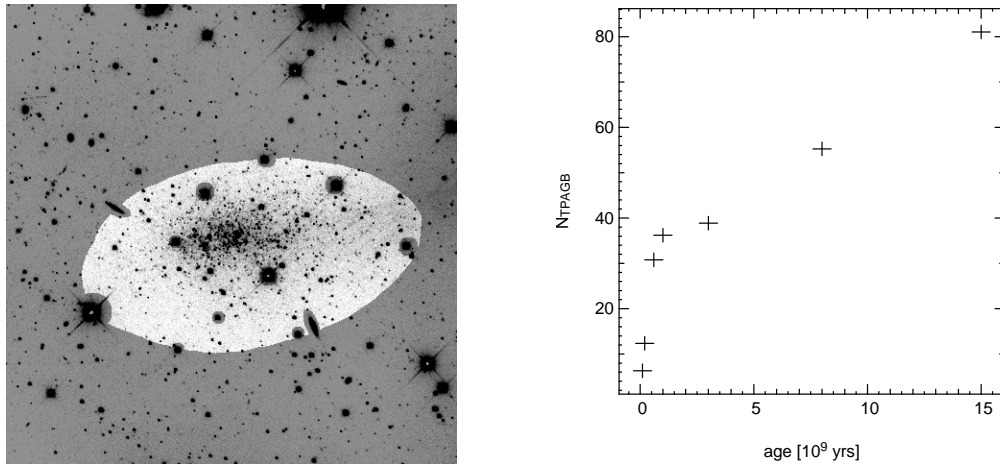


Figure 6.9: *Left panel:* The mask used to select flux from the DDO 210 dwarf galaxy overlaid on the Wendelstein reference frame. *Right panel:* The number of stars on the TPAGB as predicted by the fuel consumption theorem.

## Chapter 7

# Telescope control software

As described in the previous chapters, the obtainable image quality is essential for the project described in this thesis. A major reason for the degradation of the image quality of a given telescope is the so-called local seeing. Heat produced by the telescope or its supporting structure introduces turbulences into the optical light path degrading the image quality. During the course of the project, major investments and activities were started to improve the local seeing quality, which then consequently required new software for the 80cm telescope on Mt. Wendelstein to allow the usage of a newly built observing room and to prepare the telescope for remote observations. The developed software is documented in this chapter.

### 7.1 Motivation

During the last years the telescope was controlled using a terminal connected directly to the telescope control system (TCS) unit. This unit cannot be placed far from the telescope itself. As a consequence a room directly beneath the dome was used as observing room. Especially during winter time the need for heating and the heat emitted from the computers led to a degradation of the achievable seeing. During a major rebuild of the observatory a new observing room in the main building was constructed. To move the main telescope control unit there proved to be infeasible, simply for the length of available cabling. It would, in addition, be unwise to run copper cables of this length in the observatory. By its exposed position the site is prone to toast electronics connected to long cables with high voltages induced by thunderstorms. As a result, it was decided to construct the new telescope control software as a network based client-server architecture. This holds the advantage that the needed network cabling is already present and laid out using fiber cables, thus being save from thunderstorms.



## 7.2 Integration with existing structure

To combine the new software with the existing infrastructure, some additional preparatory work was needed. So far, the main TCS unit was controlled using a directly attached console for telescope positioning and hardware switches on the front panel for e.g. the control of the telescope drives and the dome. The TCS could additionally be controlled over a standard serial port. To facilitate this, a small program was developed for the IPC@CHIP<sup>®</sup>, a small embedded computer with a network interface, two serial ports and seven controllable pins. For these two small programs were written. One would redirect incoming data from a specific Ethernet port to one of the serial ports and vice versa. The second serial port remains unused and can be utilized as a console for the configuration of the computer. The second program would accept simple commands (e.g. set 2 on, set 4 off) on a second network port to control the output pins. With the pins connected to the hardware switches on the TCS with gap switches and one serial port connect to the TCS, this computer acts as a network relay for the TCS.

The great amount of work needed to develop from ground up a new telescope control software led to the notion to use the project as a case study for remote control of the telescope. This goal in mind, the system was designed as a client-server model. The server runs as an autonomous background task (a so called daemon) on an arbitrary Linux computer at the observatory. The client programs run on the locally on the computer of the observer – on Wendelstein or at the University in Munich 100km away. The client software then connects to the server over the local network or the Internet respectively.

## 7.3 Server design

The new TCS server was designed to be easily expandable, adding new relay connections or adding additional command functionality. The second design goal was to create a clean framework that could be adopted for other similar tasks, like the control for new instruments or a new telescope on Mt. Wendelstein.

The server program, from here on called TCSD, uses a multi-threaded layout to transfer the logical separation and simultaneity onto the object oriented program structure. The basic layout is shown in Fig. 7.1.

After startup three main threads are created. The TCSDaemon thread represents the running program and controls the client connections. For each established connection a new sub-thread is spawned that is terminated once the connection is closed. Sec. 7.3.1 gives a more detailed description of the client connections and the used clear text protocol.

The Scheduler thread manages the execution of the commands received from the clients. Due to the parallel multi-threaded layout, commands from different clients can



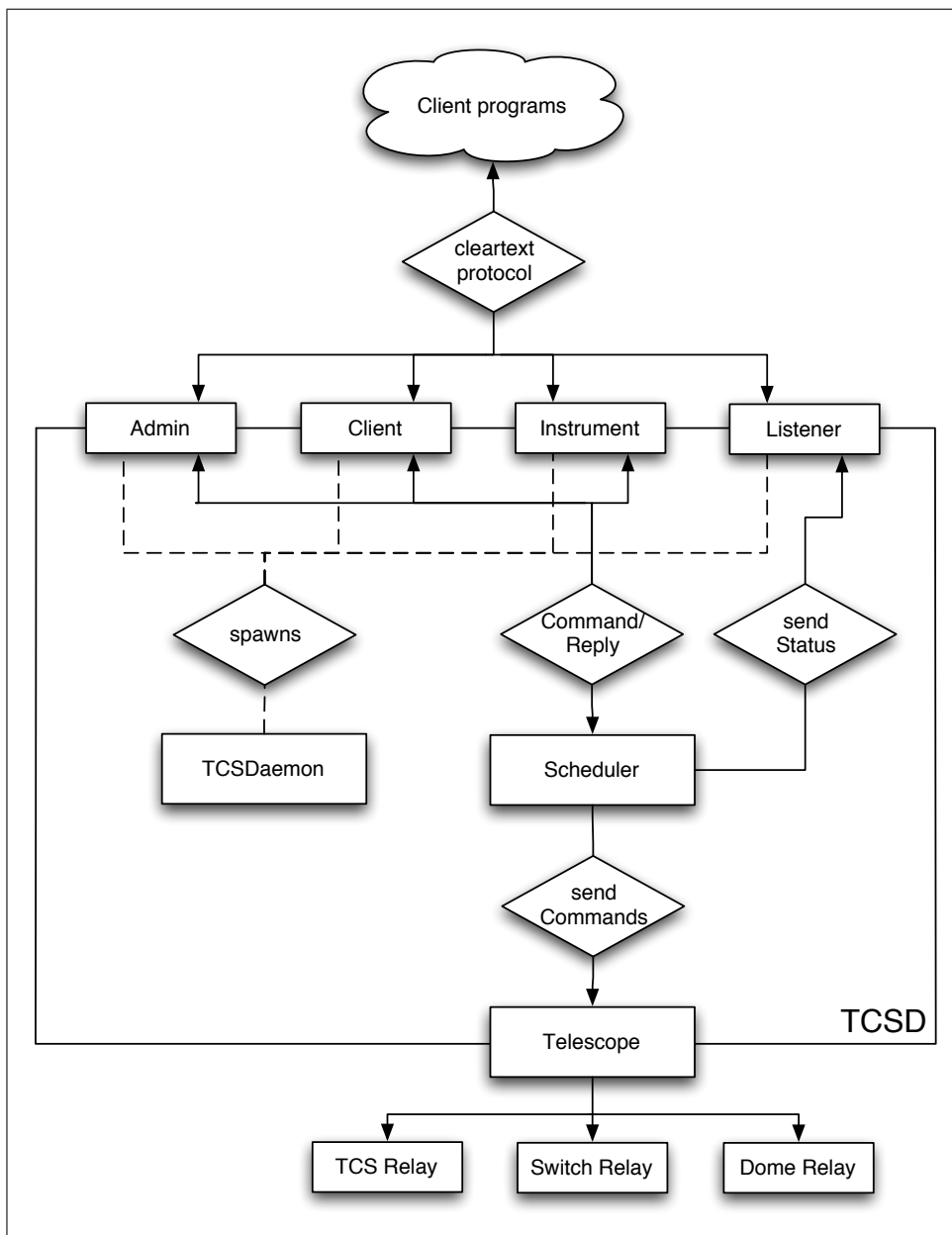


Figure 7.1: Schematic layout of the TCSD telescope control server. At startup the three main threads, TCSDaemon, Scheduler and Telescope are created. The TCSDaemon then spawns as needed the threads controlling the connections to the client software. These threads accept commands and hand them to the Scheduler. This then moves the commands on to the Telescope thread, where they are executed and sent via the relays to the telescope itself.

arrive (in principle) simultaneously and have to be executed in order without surcharging the main telescope control. The design and the internally used command objects

are thoroughly discussed in Sec. 7.3.3.

The third, the Telescope thread, represents the connections to the embedded controllers, translating the internal command structures into the low level commands used to drive the telescope. See Sec. 7.3.4 for a discussion of the connection between the Telescope thread, the Scheduler and the embedded controllers.

These threads share a common structure, the TCSState structure, which holds information about the current state of the telescope, e.g. coordinates and operational mode.

### 7.3.1 The client interface

The client interface is split into four different classes, providing different subsets of the available command set. These are accessed over four internet ports. These are defined in the configuration file and can be read and changed in the running daemon using a set of supplied commands. The config file will then be updated during shutdown of the daemon. The four different classes are:

**Admin** All the telescope commands, as well as commands to control the daemon itself are available. Access on this level could and should be reserved to a limited group of computers and possibly password protected. Only one connection is allowed at a time. A subsequent connection attempt terminates the existing connection.

**Client** All telescope commands are available. This is the connection used for normal observations. The daemon allows only one connection on this port, subsequent connection attempts are blocked. The open connection can be reset, through the `reset client` command on the Admin port.

**Instrument** A limited subset of the telescope commands are supported, additionally the legacy TCSC and TCSF commands for backward compatibility with an existing instrument of the observatory. On this port only one connection is allowed at a time. A new connection request disconnects the existing connection.

**Listener** No commands are accepted at all, instead once every second the status of the telescope and switches and the telescope coordinates are sent out to every connected client. On this port an unlimited amount of connections is allowed.

The connection procedure for the controlling connections (Admin, Client or Instrument) is shown in the left panel of Fig. 7.2. The client software attempts a connection to the daemon. After an optional check of the clients IP address the connection is established. The TCSDaemon then spawns a new thread that serves the client connection, accepting commands and sending replies. An connection attempt on the client port while an existing connection is open is blocked by the server to prevent accidental or intentional disconnection of the client used by the observer. On the admin port an

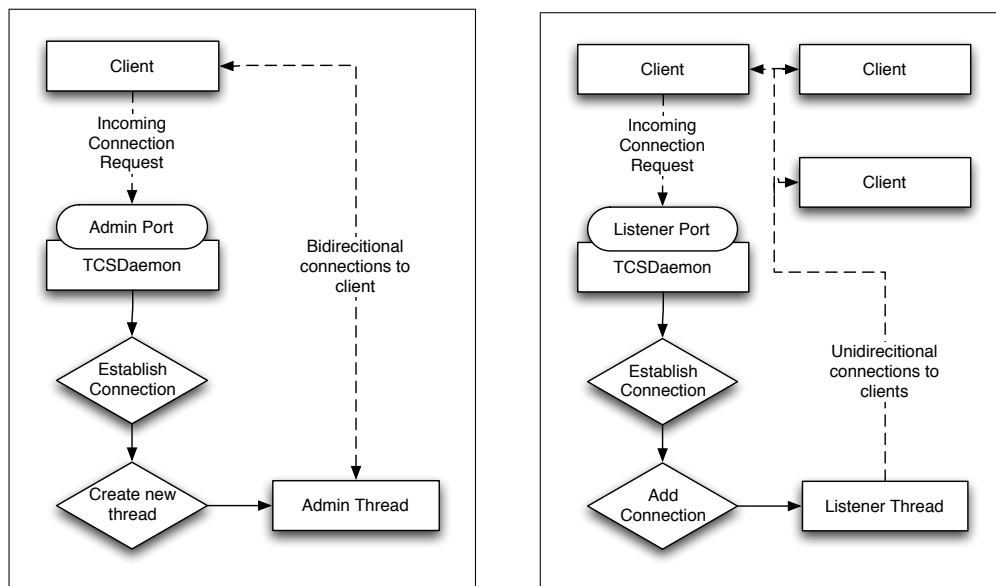


Figure 7.2: Schematic layout of the connection procedure between the clients and the server. The left panel depicts the case of the controlling connections (Admin, Client and Instrument) where only one connection at a time is allowed. The right panel shows the special case of the Listener connections where several unidirectional connections are allowed at the same time.

existing connection is terminated, once a valid connection request is accepted. This assures that an admin connection is always possible. This is important in the case that the peer of client connection crashed without a proper disconnection and blocks new connections on the port. In this case the client connection can be closed on the server-side using the `tcsd reset client` command the admin port.

The control commands are sent as clear text by the client. The thread governing the connection tries to parse the received string and creates a command object if successful. Otherwise a parse error is logged and the input buffer cleared. The created command is added to a command queue held by the scheduler. After execution `Ready $command`, `Failed $command` or `Aborted $command` (with `$command` replaced by the respective command, e.g. `set focus`) is sent back to the client if the command execution was successful, failed for some reason, or the command was aborted by a `stop` by the user. See Table C.1 in Appendix C for the complete list of commands.

### 7.3.2 The TCSState

This globally accessible structure holds a currently valid snapshot of the telescope state. This is a combination of information provided by the telescope control system, e.g. coordinates, slewing, etc. and derived states, e.g. focusing. The data held in this

structure are sent out to the connected listeners regularly. After the execution of a command, this snapshot has to be updated, as a change in the state could affect subsequent commands. For example, a `set focus` command blocks other commands till the telescope finishes focusing.

### 7.3.3 The scheduler

The Scheduler thread takes a central role in the organization of the TCS daemon, storing the command queue, executing the commands in order and keeping track of changes in the state of the telescope.

Fig. 7.3 gives a schematic overview over the logical layout of the main loop of the scheduler. This loop runs endlessly during the program execution. First if new status data was read from the telescope, the `TCSState` structure is updated, which is crucial for the tests performed in the rest of the loop. Some commands can affect the state of the telescope and thus the execution of following commands, e.g. a `go` command would block a following `set focus`. To take this into account, the boolean `stop` variable is set to `false` at the beginning of the loop and set to `true` after the execution of the first command. Once this variable is `true`, no more commands from the queue are executed, only already executed commands are checked if they finished. In the case that a command failed to execute, or a command finished normally, the respective response is sent to the client which sent the command and the command is removed from the queue. After the the last command in the queue was checked, the thread sleeps for 0.1 seconds and starts the next iteration.

The `stop` command takes a special role. When it is added, for each command already in the queue an abort message is sent to the respective client and the command deleted. After the queue was emptied, the `stop` command itself is added to the queue and processed like a normal command.

### 7.3.4 The telescope connection

The Telescope thread represents the connection to the telescope and controls the connections to the different relays. Currently three are supported, two controlling switches and one for the serial connection to the telescope control system. Another one is planned to map the functionality of the handset controls. The system is designed to make it easy to incorporate another relay connection.

The connection to the serial relay is considered indispensable and its disconnection or a connection failure during startup results in a shutdown of the daemon. A connection loss or failure of the other two relays does not lead to a shutdown, but the respective commands are disabled and return appropriate error messages.

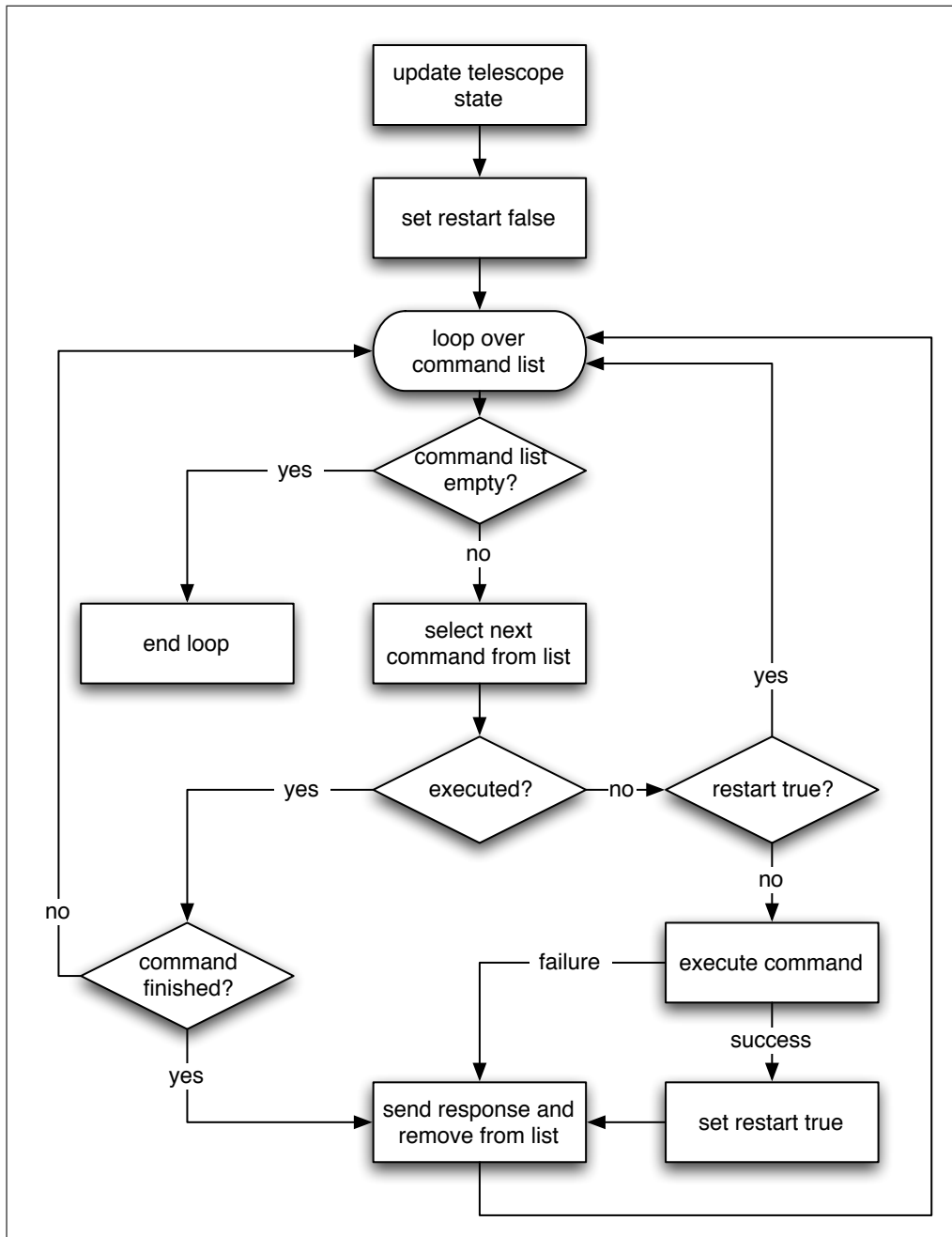


Figure 7.3: Schematic layout of the central scheduler loop. See Sec. 7.3.3 for a detailed description.

## 7.4 Client software

The use of a clear text protocol for the communication with the server makes it possible to use simple telnet for the control of the telescope. Even though this is very useful

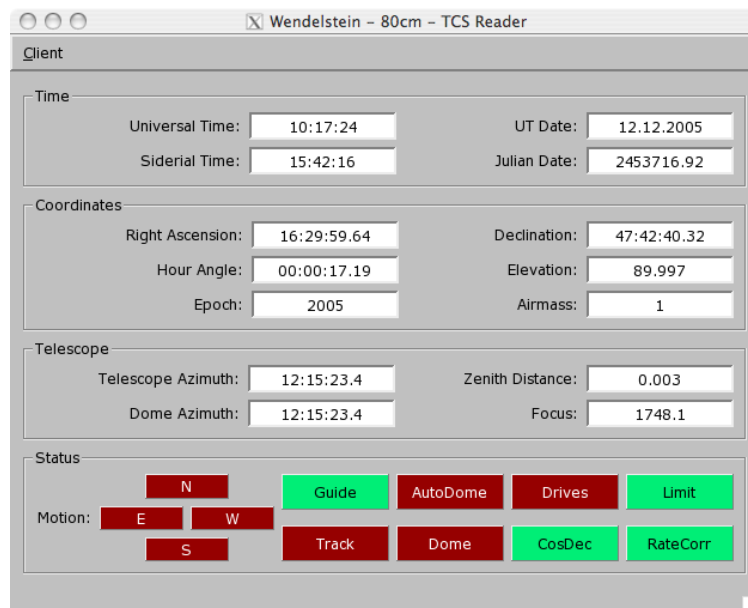


Figure 7.4: Screenshot of the reader GUI

for debugging and testing, it is clearly not an interface to be used every night by the observers. So, in addition client software was developed to provide a clean graphical user interface for the control of the TCS.

### 7.4.1 The reader GUI

The reader GUI is a rather simple graphical interface to the output on the listener port. It gives the user an overview over the current universal and sidereal time, the coordinates of the telescope in the equatorial coordinate and in the horizon system, the current airmass, the telescope focus and the state of important telescope switches. Following the server design, the reader GUI was designed with the goal in mind to support several parallel connections to the server, so it can be used to monitor the telescope status from different client computers concurrently. Fig. 7.4 shows a screenshot of the reader GUI.

### 7.4.2 The control GUI

The control GUI provides a user interface for the client port of the TCS daemon and thus serves as the main control panel. It allows the user to select the coordinates of the telescope and initiate the slew to the position as well as to manually set the telescope focus. A screen shot of the main window is shown in Fig. 7.5. The coordinate selection dialog provides the users with additional information about the selected coordinates including the airmass and rise, set and transit times. Fig. 7.6 shows a screenshot.

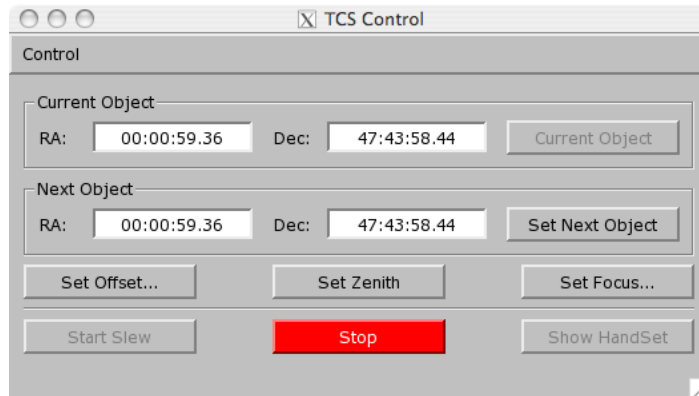


Figure 7.5: Screenshot of the main window of the control GUI

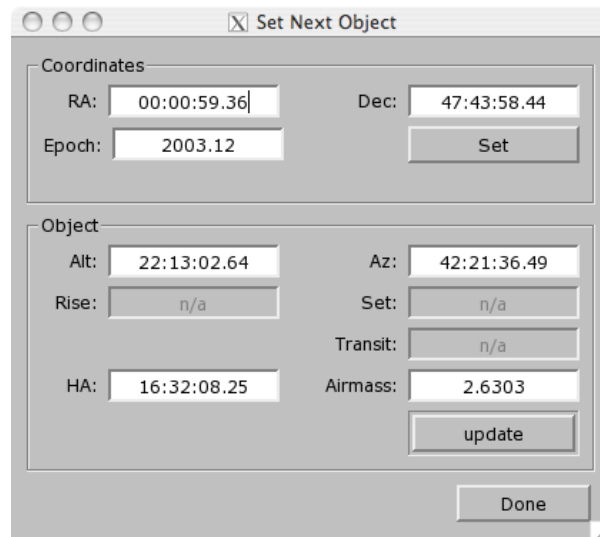


Figure 7.6: Screenshot of the object selection dialog of the control GUI





## Chapter 8

# Summary and Conclusions

In this thesis we presented results from a survey for long period variables in a sample of Local Group dwarf irregular galaxies and drew conclusions about the stellar populations and star formation history of these galaxies. This chapter aims to give a summary of the techniques applied and the derived results.

### 8.1 Summary

In Chapter 2 the selection of the candidate dwarf galaxies, the observational strategy and the applied data reduction are explained. Most of the observations were carried out at the institutes observatory on Mt. Wendelstein, using the CCD camera available at the 80 cm telescope. The continuous availability of the observing site was one of the initial driving factors to the initiation of the project. The galaxies were selected according to existing observational constraints, like sufficient observability during the year and not to interfere with the concurrent monitoring of the Andromeda galaxy done by the WeCAPP project (Riffeser *et al.*, 2001). A total of six candidates were selected, and observed sparsely over a total of five years, with three additional observing campaigns at the 1.23 m telescope at the Calar Alto Observatory, each two weeks long. The data were reduced using an astronomical standard reduction that propagates the errors during the different steps of the reduction in a separate error image (Gössl & Riffeser, 2002). The measurements for the individual epochs were obtained through difference imaging using an implementation of the optimal image subtraction algorithm (Alard & Lupton, 1998), again preserving the individual pixel errors. In this thesis the results for four dwarf galaxies from the sample are presented.

The difference imaging calculates the flux difference between the images obtained for the individual epochs and a deep reference image. To obtain comparable magnitudes a photometric calibration was obtained for the reference images, as explained in Chapter 3. For the dwarf galaxies with Calar Alto observations two different calibrations were obtained, one using the published photometry of Hubble Space Telescope

(HST) observations of the dwarf galaxies (Holtzman *et al.*, 2003), the other using observations of photometric standards obtained during one of the Calar Alto observations. In the case of the HST calibration, well resolved isolated stars were used as secondary standards to carry over the HST calibration to the reference images. For the second approach fields with calibrated standard stars were observed during a night with photometric conditions at the Calar Alto observatory. Published magnitudes of the standard stars were then used to obtain a photometric zeropoint and extinction coefficient for that night. With these values the calibrated magnitudes were calculated for a sample of well resolved, isolated stars in the observations of the dwarf galaxies during that night. These stars then once more served as secondary standards to transfer the calibration over to the reference images. A comparison of the results shows an excellent agreement for the calibration of the *R*-band, but both the *B* and the *I*-band show a significant offset ( $\sim 0.3$  mag) between the two calibrations. An investigation of colors of the stars used as secondary standards reveals that in case of the Calar Alto calibration, the colors of the available stars were probably unsuitable to transfer the calibration. Due to these inconsistencies we decided to rely on the HST calibration.

The detection and determination of the period solution of the variable sources is laid out in Chapter 4. To detect the variable sources a mask image was assembled by summing up the number of epochs the value of an individual pixel is larger than its associated error. In the resulting mask image variable sources can then simply be searched by thresholding the image and assembling the connected pixels to individual sources. The positions of these candidates were correlated against a DAOPHOT catalog of resolved sources in the reference image. The period solutions were determined using the Lafler-Kinman statistic (Lafler & Kinman, 1965). Variables flagged by it were in a final step visually inspected and sources with a clear periodic signal selected. To classify the variables apart from the period, the average magnitude is needed. The reference image is composed from several epochs and might provide average magnitude. To test the feasibility of this approach, artificial cosine shaped light-curves were constructed, the resulting magnitudes in the reference image calculated and compared with the input magnitudes. These tests showed that the approach to obtain average magnitudes from the reference image works well for short period variables. In this case the points on the light-curves contributing to the reference image are distributed randomly enough. The offset from the real average magnitude for variables with periods shorter than  $\sim 120$  days is less than 0.2 magnitudes. For longer periods the results degrade, with mis-measurements of up to 0.6 mag. For this reason, the average magnitudes of the long period variables were obtained by fitting a cosine against the data points reordered according to their phase given the derived period, with average magnitude, amplitude and phase as free parameters. The complete catalogs of periodic variable sources found in the dwarf galaxies are listed accompanied by finding charts. The variables are classified by period and average magnitude, and their position in the color-magnitude diagram.

Chapter 5 explains the completeness simulations carried out to test the limits imposed by the observations and the detection algorithms. To thoroughly address this problem, the complete parameters space consisting of position, magnitude, amplitude

and period was tested. In principle, a cosine shaped light-curve with given average magnitude, amplitude and period was created, the magnitudes for the observed epochs calculated and an artificial source placed into the images obtained at the respective epochs. There is no reason to suspect a cosmic conspiracy resulting in the preference of specific phases in the light-curves, so ten different phases were used for each parameter configuration and the results averaged. The applied difference imaging algorithm is rather time consuming, so to reduce the time needed to explore the complete parameter space a different approach was chosen. Instead of generating the light-curve, placing stars with the corresponding magnitudes in all the images and run the difference imaging pipeline for each parameter combination a grid of stars was placed in each epochs image, the difference algorithm applied and the resulting difference flux recorded. This procedure was repeated for a full set of magnitudes. The grid of difference fluxes could then be used to create light-curves directly in difference fluxes, by creating the light-curve in magnitudes and then translating the magnitudes of the different epochs into the corresponding difference fluxes. This approach made it possible to quickly test the large parameter space.

The completeness of the final catalog of periodic variable sources is composed of the individual completeness fractions of the three applied detection criteria. First, a variable must produce a sufficient amount of deviating epochs in the variation mask. Its corresponding source in the reference image must be bright enough to be detected by DAOPHOT, and finally the  $\Theta$  produced by the Lafler-Kinman statistic must be small enough that the light-curve is visually inspected and the source could be identified. To account for all these effects, the different completeness effects were tested separately. The results show that the total completeness is, as expected, fully dominated by the results for the Lafler-Kinman statistic. Both the thresholding on the variation mask as well as the requirement for a corresponding DAOPHOT detection also affect the resulting limit. The most peculiar result produced by the simulations is a slight deficiency of the Lafler-Kinman statistic to detect sources with periods of approximately one year. The same can be seen to a lesser degree in the completeness of the variation mask thresholding. This stems from the combination of the period and the half-year long observing window. For some parameter combinations the star is only visible in the minimum of the light-curve. Naturally the error will be larger for the resulting faint sources. The variation mask, then might not find enough points above the threshold and the Lafler-Kinman statistic will reject more data points due to too large errors.

The obtained photometry and catalogs of variable sources were applied in Chapter 6 to draw conclusions on the star formation history of the studied dwarf galaxies. To derive star formation histories from the numbers of variables found, the fuel consumption theorem (Renzini & Buzzoni, 1986; Renzini, 1998) was applied. As the age of a stellar population increases, more and more stars leave the main sequence and evolve onto the red giant branch and then onto the asymptotic giant branch. Knowing the time a star of a given age spends in any of these post MS phases, the total number of stars in that stage can be predicted as a function of the age of the population and the luminosity sampled. When only applied to long period variables (LPVs) this procedure can still be degenerate. An observed number of LPVs can either be produced by

a population of one age alone or be a combination of the relative contributions of populations at different ages. To break this degeneracy, a second age indicator is needed. In our case we use the comparison of the color-magnitude diagrams obtained from the reference images with theoretical evolutionary tracks of stellar populations of different ages.

For Leo A the color-magnitude diagram shows a well populated red giant branch (RGB), compatible with an old stellar population ( $\sim 10$  to 14 Gyrs) and main sequence and a blue loop corresponding to a younger population of approximately 0.5 Gyrs. The magnitude of the tip of the red giant branch (TRGB) is in good agreement with Schulte-Ladbeck *et al.* (2002). The comparison of the predictions of the fuel consumption theorem with the eleven LPVs found further confirms the star formation history determined by Schulte-Ladbeck *et al.* (2002) from synthetic color-magnitude diagrams. Vansėvičius *et al.* (2004) found evidence for the existence of an old stellar halo surrounding Leo A. The color-magnitude diagram obtained from our data in the field around Leo A could support an 14 Gyr old population. The complete lack of LPVs in this area could serve as another indicator for a very old population. This can be seen to be in agreement with Dolphin *et al.* (2002), who found one of their RR-Lyrae candidates outside the visually prominent dwarf galaxy.

In case of DDO 216 the comparison of the CMD with the theoretical isochrones shows a young population with an age of  $\sim 0.15$  Gyrs and a red giant branch from an intermediate age population (6 – 10 Gyrs.) The 52 LPVs found are in agreement with that intermediate age population ( $\sim 2$  – 6 Gyrs) a result proposed by Gallagher *et al.* (1998) as well. Similarly we can exclude a dominant young population ( $< 1$  Gyr). The contribution of an old population cannot be fully excluded, but would be inconsistent with the obtained color-magnitude diagrams.

The two LPVs found in GR 8 must be considered to be an incomplete sample, given the *R*-band completeness limit of 21.8 and the *I*-band magnitude of the TRGB of 22.7 (Dohm-Palmer *et al.*, 1998). The color-magnitude diagram indicates a young population (0.05 – 1 Gyrs), a result in agreement with the small number of LPVs found and the findings of Dohm-Palmer *et al.* (1998) using HST data. From the study of the color-magnitude diagrams a contribution of an intermediate age population (5 – 10 Gyrs) cannot be excluded.

The search for variable sources in DDO 210 turned up nothing at all. Given the adopted distance modulus of 20.95 (Lee *et al.*, 1999) and the 50% completeness limit of  $\sim 20.3$  for sources with 1 mag peak to peak amplitude one would expect to find several long period variables. The color-magnitude diagrams constructed from public HST data show either a young (0.5 Gyr) old population at a metallicity of  $Z = 0.008$  or an old one (14 Gyr) with a metallicity of  $Z = 0.0003$ . The lack of variable sources can be explained by an ancient population, so old that all stars massive enough already evolved past their AGB phase. An old population with low metallicity is in agreement with the work by McConnachie *et al.* (2005).

## 8.2 Concluding synthesis

In this thesis we presented results of a long term survey for variable stars in a small sample of dwarf irregular galaxies in the Local Group. We have shown that such a project can be carried out at a small telescope and have established catalogs of variable sources in the observed galaxies. We showed that long period variables can be used as a tracer of stellar populations and the star formation history. To break the remaining degeneracy a second indicator is needed. In this case the still poorly understood late evolutionary phases of stars of intermediate mass, the AGB phase, can be explored. So far the results presented for a small sample of low metallicity dwarf irregular galaxies are in good agreement with the predictions based on the fuel-consumption theorem (Renzini, 1998; Renzini & Fusi Pecci, 1988). A comparison to more sophisticated models has to be postponed until AGB evolutionary models with sub-solar abundances have been developed.

A similar study of a sample of globular clusters, with known ages and metallicities, could be used to obtain measurements of the time stars spent in the LPV phase. Such measurements would remove the dependency on the judgment of the ratio between stars on the TPAGB and LPVs.



# Bibliography

- Alard, C. & Lupton, R. H. 1998: *A Method for Optimal Image Subtraction*, ApJ, 503, 325 [28](#), [91](#)
- Aparicio, A. 1994: *The distance to the Pegasus Dwarf Irregular Galaxy: an open question*, ApJ, 437, L27 [22](#)
- Aparicio, A. & Gallart, C. 1995: *The Stellar Content of the Pegasus Dwarf Irregular Galaxy*, AJ, 110, 2105 [22](#), [75](#)
- Aparicio, A., Gallart, C., & Bertelli, G. 1997a: *The Star Formation History of the Pegasus Dwarf Irregular Galaxy*, AJ, 114, 669 [22](#), [75](#)
- Aparicio, A., Gallart, C., & Bertelli, G. 1997b: *The Stellar Content and the Star Formation History of the Local Group Dwarf Galaxy LGS 3.*, AJ, 114, 680 [19](#)
- Aparicio, A., Garcia-Pelayo, J. M., & Moles, M. 1988: *CCD Photometry of Resolved Dwarf Irregular Galaxies - Part Three - GR:8*, A&AS, 74, 375 [21](#)
- Becker, S. A. 1998: *The Variable Star Menagerie*, in ASP Conf. Ser. 135: A Half Century of Stellar Pulsation Interpretation, 12 [12](#), [13](#), [14](#)
- Bertelli, G., Bressan, A., Chiosi, C., Fagotto, F., & Nasi, E. 1994: *Theoretical isochrones from models with new radiative opacities*, A&AS, 106, 275 [32](#)
- Caldwell, N., Armandroff, T. E., Da Costa, G. S., & Seitzer, P. 1998: *Dwarf elliptical galaxies in the M81 Group - The structure and stellar populations of BK5N and F8DI*, AJ, 115, 535 [69](#)
- Christensen-Dalsgaard, J. & Dziembowski, W. A. 2000: *Basic Aspects of Stellar Structure and Pulsation*, in NATO ASIC Proc. 544: Variable Stars as Essential Astrophysical Tools, 1 [12](#)
- Christian, C. A. & Tully, R. B. 1983: *The local group irregular galaxies LGS 3 and Pegasus*, AJ, 88, 934 [18](#)
- Davidge, T. J. & Rigaut, F. 2004: *Photometric Variability among the Brightest Asymptotic Giant Branch Stars near the Center of M32*, ApJ, 607, L25 [73](#)

- de Vaucouleurs, G. 1975: *Nearby groups of galaxies.*, *Social Studies of Science*, 9, 557 20
- de Vaucouleurs, G. & Moss, C. 1983: *The magellanic irregular galaxy DDO 155*, *ApJ*, 271, 123 21
- de Vaucouleurs, G., Peters, W. L., & Corwin, H. G. 1977: *Possible New Members of the Local Group of Galaxies from Solar Motion Solutions*, *ApJ*, 211, 319 20
- Demers, S., Kibblewhite, E. J., Irwin, M. J., Bunclark, P. S., & Bridgeland, M. T. 1984: *Leo A - Color-magnitude diagram of its brightest stars*, *AJ*, 89, 1160 20
- Dohm-Palmer, R. C., Skillman, E. D., Gallagher, J., Tolstoy, E., Mateo, M., Dufour, R. J., Saha, A., Hoessel, J., & Chiosi, C. 1998: *The Recent Star Formation History of GR 8 from Hubble Space Telescope Photometry of the Resolved Stars*, *AJ*, 116, 1227 21, 49, 50, 77, 78, 94
- Dolphin, A. E., Saha, A., Claver, J., Skillman, E. D., Cole, A. A., Gallagher, J. S., Tolstoy, E., Dohm-Palmer, R. C., & Mateo, M. 2002: *Variable Stars in Leo A: RR Lyrae Stars, Short-Period Cepheids, and Implications for Stellar Content*, *AJ*, 123, 3154 21, 75, 94
- Eddington, A. E. 1917: *Council note on the motions of spiral nebulae*, *MNRAS*, 77, 375 5
- Ellis, G. L., Grayson, E. T., & Bond, H. E. 1984: *A search for faint planetary nebulae on Palomar sky survey prints*, *PASP*, 96, 283 6, 19
- Flaccomio, E., Micela, G., Sciortino, S., Favata, F., Corbally, C., & Tomaney, A. 1999: *BVRI photometry of the star-forming region NGC 2264: the initial mass function and star-forming rate*, *A&A*, 345, 521 25, 32, 34, 36
- Gössl, C. A. & Riffeser, A. 2002: *Image reduction pipeline for the detection of variable sources in highly crowded fields*, *A&A*, 381, 1095 25, 26, 91
- Gössl, C. A. & Riffeser, A. 2003: *Image Reduction Pipeline for the Detection of Variable Sources in Highly Crowded Fields*, in *ASP Conf. Ser. 295: Astronomical Data Analysis Software and Systems XII*, 229 25
- Gallagher, J. S., Tolstoy, E., Dohm-Palmer, R. C., Skillman, E. D., Cole, A. A., Hoessel, J. G., Saha, A., & Mateo, M. 1998: *A Wide Field Planetary Camera 2 Study of the Resolved Stellar Population of the Pegasus Dwarf Irregular Galaxy (DDO 216)*, *AJ*, 115, 1869 22, 47, 75, 76, 94
- Gautschy, A. & Saio, H. 1995: *Stellar Pulsations Across The HR Diagram: Part 1*, *ARA&A*, 33, 75 12
- Gautschy, A. & Saio, H. 1996: *Stellar Pulsations Across the HR Diagram: Part 2*, *ARA&A*, 34, 551 12, 13



- Girardi, L., Bressan, A., Bertelli, G., & Chiosi, C. 2000: *Evolutionary tracks and isochrones for low- and intermediate-mass stars: From 0.15 to 7  $M_{\odot}$ , and from  $Z=0.0004$  to 0.03*, A&AS, 141, 371 [10](#)
- Gössl, C. 2006: *Finding Variable Stars in Northern Dwarf Galaxies of the Local Group*, PhD thesis, Unisternwarte München [1](#), [14](#), [18](#), [24](#), [25](#), [26](#), [27](#), [38](#), [47](#)
- Grebel, E. K. 2001: *Dwarf Galaxies in the Local Group and in the Local Volume (Invited Talk)*, in Dwarf galaxies and their environment, 45 [7](#), [8](#)
- Greggio, L., Marconi, G., Tosi, M., & Focardi, P. 1993: *Star formation in dwarf irregular galaxies - DDO 210 and NGC 3109*, AJ, 105, 894 [22](#)
- Groenewegen, M. A. T., Romaniello, M., Primas, F., & Mottini, M. 2004: *The metallicity dependence of the Cepheid PL-relation*, A&A, 420, 655 [13](#), [43](#)
- Herschel, W. 1785: *On the Construction of the Heavens.*, Philosophical Transactions Series I, 75, 213 [1](#)
- Hodge, P. W. 1967: *The Nature of the Remarkable Galaxy G. R.*, ApJ, 148, 719 [21](#)
- Hoessel, J. G., Abbott, M. J., Saha, A., Mossman, A. E., & Danielson, G. E. 1990: *Variable stars in the Pegasus dwarf galaxy (DDO 216)*, AJ, 100, 1151 [22](#)
- Hoessel, J. G. & Danielson, G. E. 1983: *Photometry of resolved galaxies. III - GR 8*, ApJ, 271, 65 [21](#)
- Hoessel, J. G. & Mould, J. R. 1982: *Photometry of resolved galaxies. I - The Pegasus dwarf irregular*, ApJ, 254, 38 [22](#)
- Hoessel, J. G., Saha, A., & Danielson, G. E. 1988: *Deep CCD observations of nearby dwarf galaxy candidates*, PASP, 100, 680 [19](#)
- Hoessel, J. G., Saha, A., Krist, J., & Danielson, G. E. 1994: *Variable stars in the Leo A dwarf galaxy (DDO 69)*, AJ, 108, 645 [20](#)
- Holmberg, E. 1958: *A photographic photometry of extragalactic nebulae.*, Meddelanden fran Lunds Astronomiska Observatorium Serie II, 136, 1 [22](#)
- Holtzman, J., Afonso, C., & Dolphin, A. 2003ApJS, submitted [31](#), [33](#), [50](#), [75](#), [76](#), [77](#), [78](#), [79](#), [80](#), [92](#)
- Holtzman, J. A., Burrows, C. J., Casertano, S., Hester, J. J., Trauger, J. T., Watson, A. M., & Worthey, G. 1995: *The Photometric Performance and Calibration of WFPC2*, PASP, 107, 1065 [31](#)
- Hopp, U., Gössl, C. A., Snigula, J., & Riffeser, A. 2006: *The classical  $\delta$  Cep stars in Leo A*, A&A, in preparation [21](#)
- Hubble, E. P. 1929: *A spiral nebula as a stellar system, Messier 31.*, ApJ, 69, 103 [1](#)

- Hubble, E. P. 1936: *Realm of the Nebulae*, Yale University Press 1, 7
- Iben, I. 1976: *Further adventures of a thermally pulsing star*, ApJ, 208, 165 8
- Iben, I. & Renzini, A., eds. 1981, Physical processes in red giants; Proceedings of the Second Workshop, Advanced School of Astronomy, Erice, Italy, September 3-13, 1980 8
- Iben, I. & Renzini, A. 1983: *Asymptotic giant branch evolution and beyond*, ARA&A, 21, 271 8
- Irwin, M. 1999: *Proper Motions of Local Group Satellites*, in IAU Symposium, 409 2, 4, 6
- Jacoby, G. H. & Lesser, M. P. 1981: *Distances to nearby galaxies derived from planetary nebulae*, AJ, 86, 185 20, 22
- Karachentsev, I., Drozdovsky, I., Kajsin, S., Takalo, L. O., Heinamaki, P., & Valtonen, M. 1997: *Revised photometric distances to nearby dwarf galaxies in the IC 342/Maffei complex*, A&AS, 124, 559 19
- Karachentsev, I. D., Tikhonov, N. A., & Sazonova, L. N. 1994: *NGC 1569 and UGCA 92: a nearby pair of galaxies in the Milky Way*, Astronomy Letters, 20, 84 19
- Kauffmann, G. & White, S. D. M. 1993: *The merging history of dark matter haloes in a hierarchical universe.*, MNRAS, 261, 921 7
- Kauffmann, G., White, S. D. M., & Guiderdoni, B. 1993: *The Formation and Evolution of Galaxies Within Merging Dark Matter Haloes*, MNRAS, 264, 201 7
- Kowal, C. T., Lo, K. Y., & Sargent, W. L. W. 1978: *New Galaxies of the Local Group*, IAU Circ., 3305, 2 18
- Lafler, J. & Kinman, T. D. 1965: *An RR Lyrae Star Survey with the Lick 20-INCH Astrograph II. The Calculation of RR Lyrae Periods by Electronic Computer.*, ApJS, 11, 216 38, 92
- Leavitt, H. S. & Pickering, E. C. 1912: *Periods of 25 Variable Stars in the Small Magellanic Cloud.*, Harvard College Observatory Circular, 173, 1 5
- Lee, M. G. 1995: *Stellar Populations of the Dwarf Galaxy LGS 3 in the Local Group*, AJ, 110, 1129 18, 19
- Lee, M. G., Aparicio, A., Tikonov, N., Byun, Y.-I., & Kim, E. 1999: *Stellar Populations and the Local Group Membership of the Dwarf Galaxy DDO 210*, AJ, 118, 853 22, 80, 94
- Lee, M. G., Freedman, W. L., & Madore, B. F. 1993: *The Tip of the Red Giant Branch as a Distance Indicator for Resolved Galaxies*, ApJ, 417, 553 5

- Lomb, N. R. 1976: *Least-squares frequency analysis of unequally spaced data*, Ap&SS, 39, 447 38
- Madore, B., Freedman, W., & Murdin, P. 2000: *Cepheid Period-Luminosity Relation*, Encyclopedia of Astronomy and Astrophysics 5, 13
- Madore, B. F. & Freedman, W. L. 1998: *HIPPARCOS Parallaxes and the Cepheid Distance Scale*, ApJ, 492, 110 5, 13
- Maraston, C. 1998: *Evolutionary synthesis of stellar populations: a modular tool*, MNRAS, 300, 872 72
- Marconi, G., Focardi, P., Greggio, L., & Tosi, M. 1990: *DDO 210 - The actual appearance of a 'ghost' irregular galaxy*, ApJ, 360, L39 21
- Mateo, M. L. 1998: *Dwarf Galaxies of the Local Group*, ARA&A, 36, 435 2, 3, 7, 8, 17, 18
- McConnachie, A. W., Irwin, M. J., Ferguson, A. M. N., Ibata, R. A., Lewis, G. F., & Tanvir, N. 2005: *Distances and metallicities for 17 Local Group galaxies*, MNRAS, 356, 979 19, 22, 76, 78, 79, 94
- Miller, B. W., Dolphin, A. E., Lee, M. G., Kim, S. C., & Hodge, P. 2001: *The Star Formation History of LGS 3*, ApJ, 562, 713 19
- Monet, D. 1996: *The 491,848,883 Sources in USNO-A1.0*, Bulletin of the American Astronomical Society, 28, 905 27
- Monet, D. G. 1998: *The 526,280,881 Objects In The USNO-A2.0 Catalog*, Bulletin of the American Astronomical Society, 30, 1427 27
- Mould, J. 1997: *The Star-Formation History of LGS 3*, PASP, 109, 125 19
- Nilson, P. 1974: *"Catalogue of Selected Non-Ugc Galaxies", 1974, Uppsala Observatory Report no.*, in UGCA, 0 6
- Paturel, G., Fouque, P., Bottinelli, L., & Gouguenheim, L. 1989: *An extragalactic database. I - The Catalogue of Principal Galaxies*, A&AS, 80, 299 6
- Perryman, M. A. C., Lindegren, L., Kovalevsky, J., Hoeg, E., Bastian, U., Bernacca, P. L., Cr  z  , M., Donati, F., Grenon, M., van Leeuwen, F., van der Marel, H., et al. 1997: *The HIPPARCOS Catalogue*, A&A, 323, L49 9
- Pietrinferni, A., Cassisi, S., Salaris, M., & Castelli, F. 2004: *A Large Stellar Evolution Database for Population Synthesis Studies. I. Scaled Solar Models and Isochrones*, ApJ, 612, 168 73, 74, 75, 76, 77, 78, 79, 80
- Piotto, G., King, I. R., Djorgovski, S. G., Sosin, C., Zoccali, M., Saviane, I., De Angeli, F., Riello, M., Recio-Blanco, A., Rich, R. M., Meylan, G., et al. 2002: *HST color-magnitude diagrams of 74 galactic globular clusters in the HST F439W and F555W bands*, A&A, 391, 945 11, 12

- Reaves, G. 1956: *Dwarf galaxies in the Virgo cluster.*, AJ, 61, 69 21
- Rejkuba, M., Minniti, D., Silva, D. R., & Bedding, T. R. 2003: *Long Period Variables in NGC 5128 . II. Near-IR properties*, A&A, 411, 351 73
- Renzini, A. 1994: *Stellar-population tools and clues to galaxy formation*, in Galaxy Formation, 303 70, 71
- Renzini, A. 1998: *The Stellar Populations of Pixels and Frames*, AJ, 115, 2459 70, 71, 73, 77, 93, 95
- Renzini, A. & Buzzoni, A. 1986: *Global properties of stellar populations and the spectral evolution of galaxies*, in ASSL Vol. 122: Spectral Evolution of Galaxies, 195–231 8, 71, 93
- Renzini, A. & Fusi Pecci, F. 1988: *Tests of evolutionary sequences using color-magnitude diagrams of globular clusters*, ARA&A, 26, 199 8, 69, 71, 73, 77, 95
- Riffeser, A., Fliri, J., Gössl, C. A., Bender, R., Hopp, U., Bärnbantner, O., Ries, C., Barwig, H., Seitz, S., & Mitsch, W. 2001: *WeCAPP - Wendelstein Calar Alto pixel-lensing project I. Tracing dark and bright matter in M 31*, A&A, 379, 362 17, 23, 91
- Russell, H. N. 1933: *The Constitution of the Stars*, J. R. Astron. Soc. Can., 27, 375 8
- Salpeter, E. E. 1955: *The Luminosity Function and Stellar Evolution.*, ApJ, 121, 161 70
- Sandage, A. 1986: *The brightest stars in nearby galaxies. VII - The Pegasus and Leo A Im V dwarfs*, AJ, 91, 496 20
- Sandage, A. & Tammann, G. A. 1982: *Steps toward the Hubble constant. VIII - The global value*, ApJ, 256, 339 20
- Scargle, J. D. 1982: *Studies in astronomical time series analysis. II - Statistical aspects of spectral analysis of unevenly spaced data*, ApJ, 263, 835 38
- Schild, R. 1980: *CCD camera observations of the local group galaxy LGS-3*, ApJ, 242, 63 18
- Schlegel, D. J., Finkbeiner, D. P., & Davis, M. 1998: *Maps of Dust Infrared Emission for Use in Estimation of Reddening and Cosmic Microwave Background Radiation Foregrounds*, ApJ, 500, 525 72
- Schulte-Ladbeck, R. E. & Hopp, U. 1998: *The Stellar Content of 10 Dwarf Irregular Galaxies*, AJ, 116, 2886 21
- Schulte-Ladbeck, R. E., Hopp, U., Drozdovsky, I. O., Greggio, L., & Crone, M. M. 2002: *The Oldest Stars of the Extremely Metal-Poor Local Group Dwarf Irregular Galaxy Leo A*, AJ, 124, 896 20, 21, 44, 73, 74, 75, 94

- Snigula, J., Drory, N., Bender, R., Botzler, C. S., Feulner, G., & Hopp, U. 2002: *The Munich Near-Infrared Cluster Survey - IV. Biases in the completeness of near-infrared imaging data*, MNRAS, 336, 1329 51
- Stetson, P. B. 1987: *DAOPHOT - A computer program for crowded-field stellar photometry*, PASP, 99, 191 27, 31
- Thé, P. S., Thomas, D., Christensen, C. G., & Westerlund, B. E. 1990: *VRI photometric properties of M-type giants*, PASP, 102, 565 32
- Tikhonov, N. & Makarova, L. 1996: *A colour-magnitude diagram of the Pisces dwarf galaxy*, Astron. Nachr., 317, 179 19
- Tolstoy, E., Gallagher, J. S., Cole, A. A., Hoessel, J. G., Saha, A., Dohm-Palmer, R. C., Skillman, E. D., Mateo, M., & Hurley-Keller, D. 1998: *Wide Field Planetary Camera 2 Observations of Leo A: A Predominantly Young Galaxy within the Local Group*, AJ, 116, 1244 20
- Tolstoy, E., Saha, A., Hoessel, J. G., & Danielson, G. E. 1995: *Variable stars in the dwarf galaxy GR 8 (DDO 155)*, AJ, 109, 579 21
- Tomaney, A. B. & Crofts, A. P. S. 1996: *Expanding the Realm of Microlensing Surveys with Difference Image Photometry*, AJ, 112, 2872 28
- van den Bergh, S. 1959: *A catalogue of dwarf galaxies*, Publications of the David Dunlap Observatory, 2, 147 6, 20, 21, 22
- van den Bergh, S. 1966: *Luminosity classifications of dwarf galaxies.*, AJ, 71, 922 20
- van den Bergh, S. 1999: *The local group of galaxies*, A&AR, 9, 273 7
- van den Bergh, S. 2000: *Updated Information on the Local Group*, PASP, 112, 529 2, 3
- Vansevičius, V., Arimoto, N., Hasegawa, T., Ikuta, C., Jablonka, P., Narbutis, D., Ohta, K., Stonkutė, R., Tamura, N., Vansevičius, V., & Yamada, Y. 2004: *The Full-fledged Dwarf Irregular Galaxy Leo A*, ApJ, 611, L93 21, 75, 94
- Vassiliadis, E. & Wood, P. R. 1993: *Evolution of low- and intermediate-mass stars to the end of the asymptotic giant branch with mass loss*, ApJ, 413, 641 69, 72, 75, 76
- Yahil, A., Tammann, G. A., & Sandage, A. 1977: *The Local Group - The solar motion relative to its centroid*, ApJ, 217, 903 20



## Appendix A

# Rejected dwarf galaxy candidates

In this chapter is presented a list of rejected dwarf galaxy candidates with reasons for the exclusion.

**WLM** Low declination resulting in suboptimal observation conditions and a much concurrent work by other groups, as the object is well accessible from the southern hemisphere where several monitoring projects are conducted.

**IC 10** Low galactic latitude and therefore a strong contamination of foreground stars.

**IC 1613** Low declination and it has been searched for variable sources before.

**Sextans A, Sextans B** Low declination and probably a large distance, lowering the chances of obtaining deep enough imaging to find variables.

**NGC6822** Low declination as well.





## Appendix B

# Variable source lightcurves

### B.1 Light curves of Leo A variables

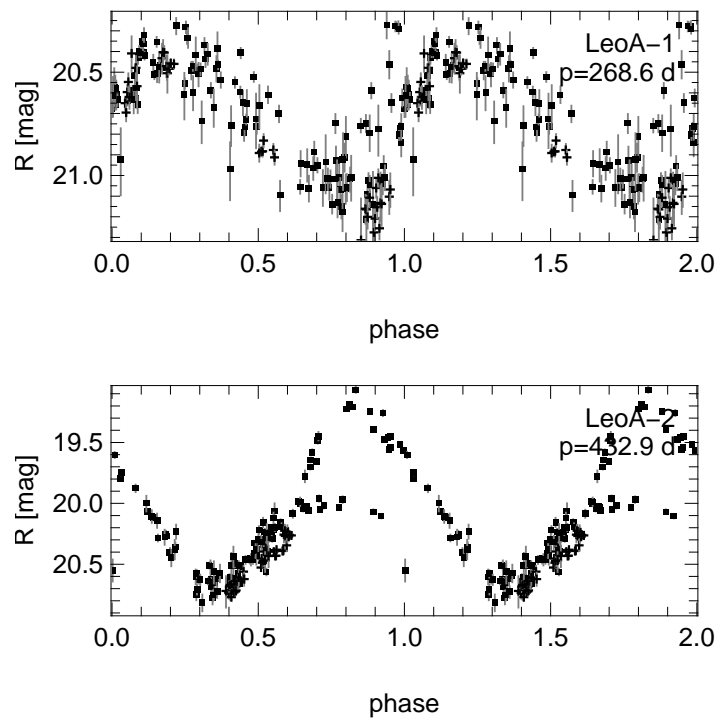


Figure B.1: Light-curves for variable sources found in the Leo A dwarf galaxy. Plotted is the  $R$ -band magnitude against the phase, repeated over for two phases to guide the eye. WST observations are plotted as squares, Calar Alto data as crosses.

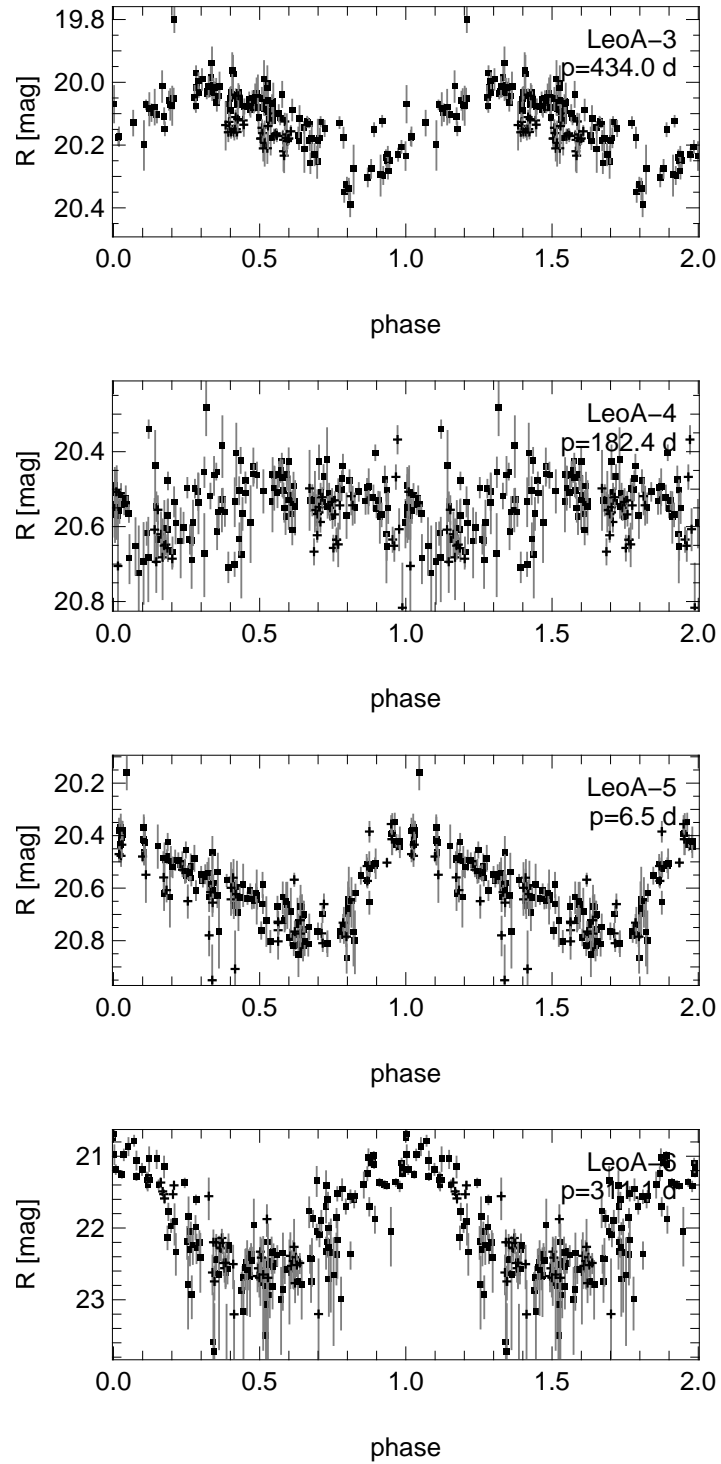


Figure B.2: Light-curves for variable sources found in the Leo A dwarf galaxy. Plotted is the  $R$ -band magnitude against the phase, repeated over for two phases to guide the eye. WST observations are plotted as squares, Calar Alto data as crosses.

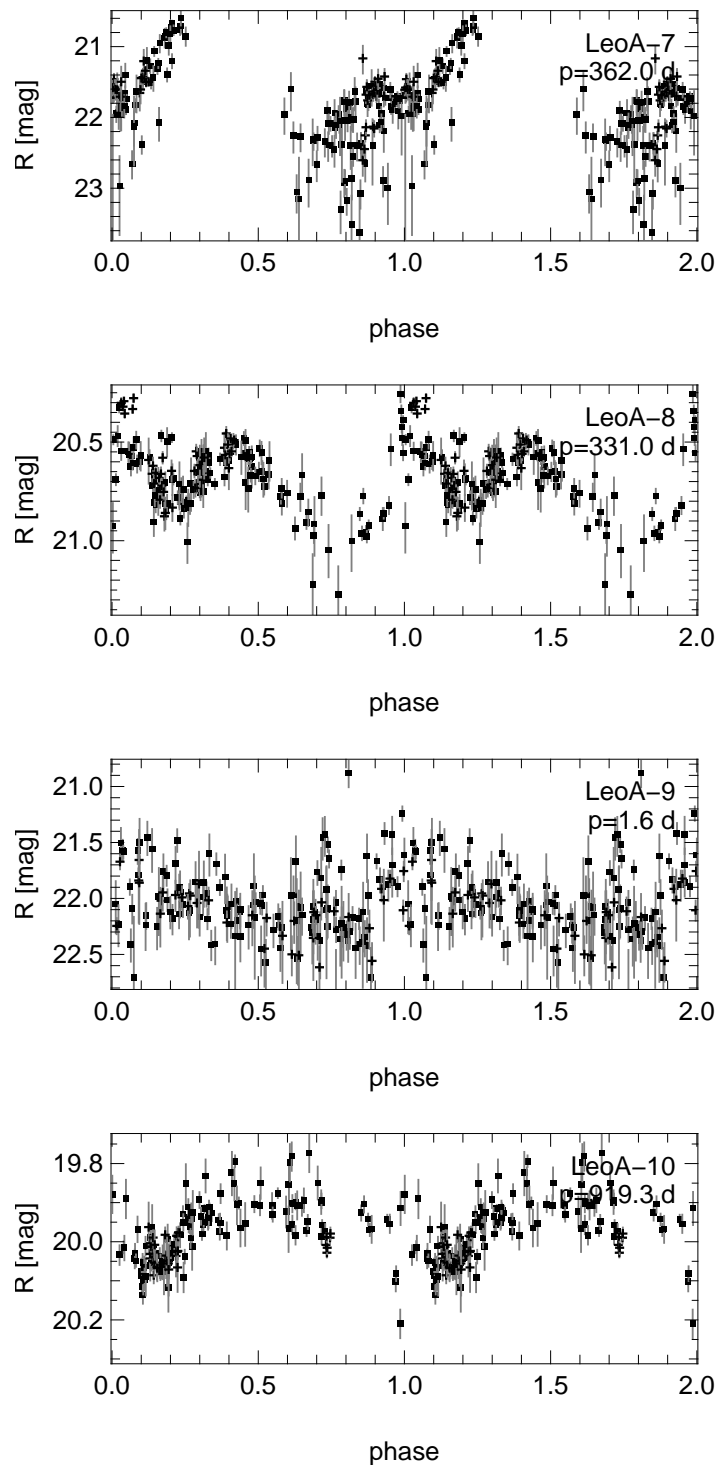


Figure B.3: Light-curves for variable sources found in the Leo A dwarf galaxy. Plotted is the  $R$ -band magnitude against the phase, repeated over for two phases to guide the eye. WST observations are plotted as squares, Calar Alto data as crosses.

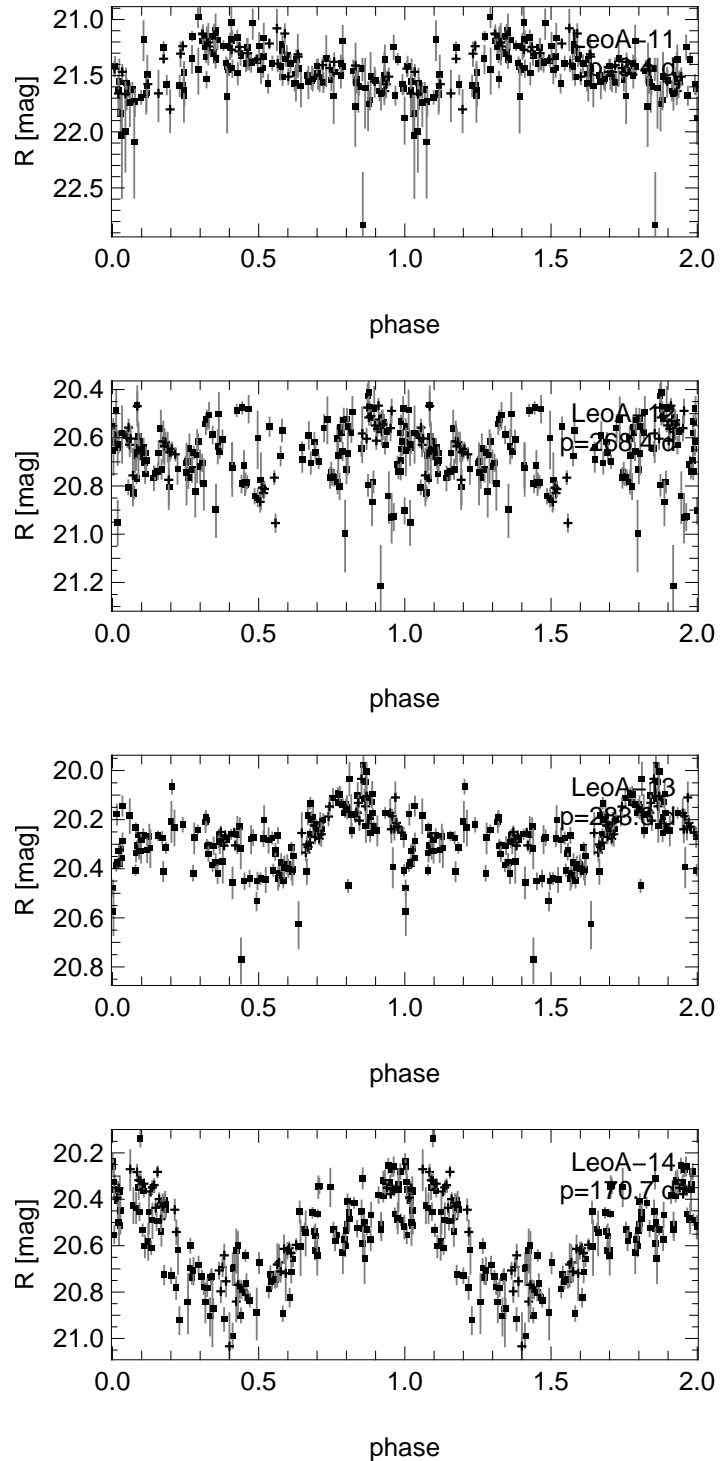


Figure B.4: Light-curves for variable sources found in the Leo A dwarf galaxy. Plotted is the  $R$ -band magnitude against the phase, repeated over for two phases to guide the eye. WST observations are plotted as squares, Calar Alto data as crosses.

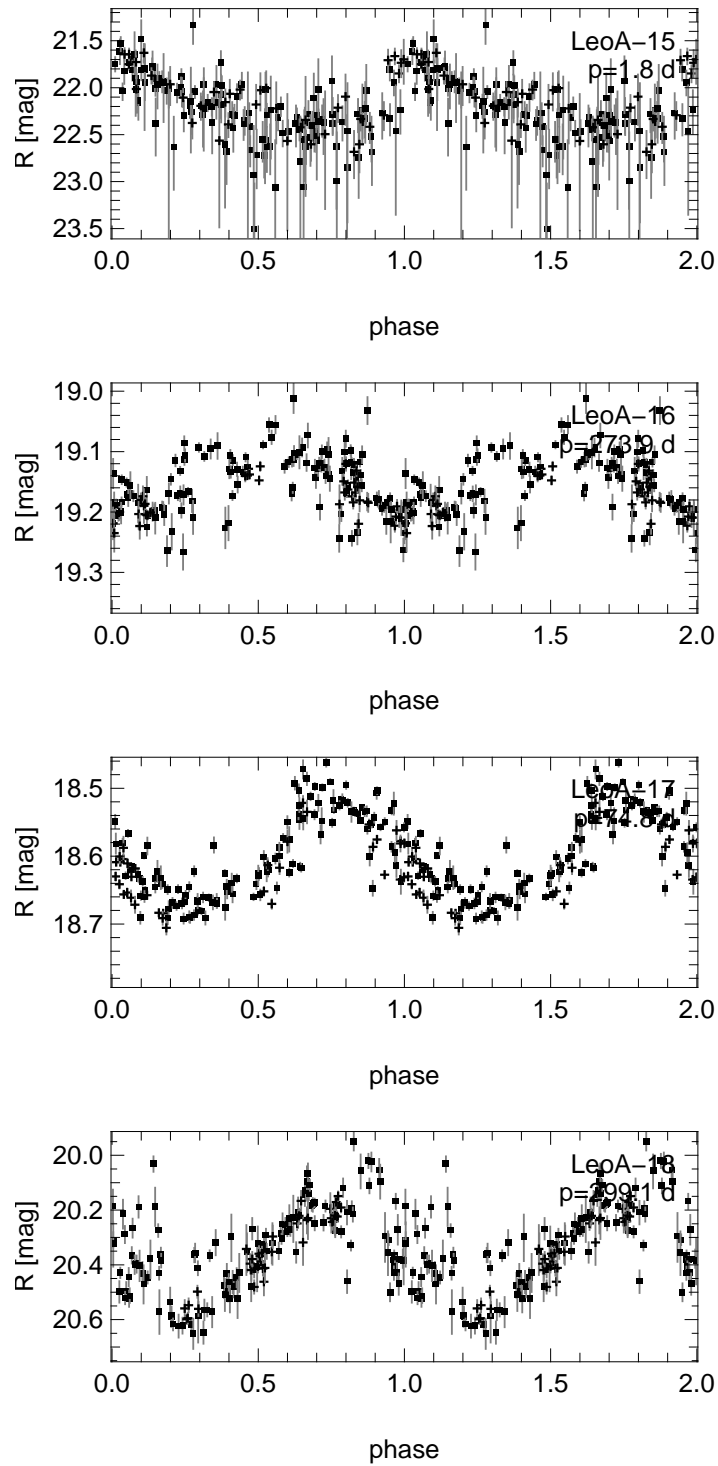


Figure B.5: Light-curves for variable sources found in the Leo A dwarf galaxy. Plotted is the  $R$ -band magnitude against the phase, repeated over for two phases to guide the eye. WST observations are plotted as squares, Calar Alto data as crosses.

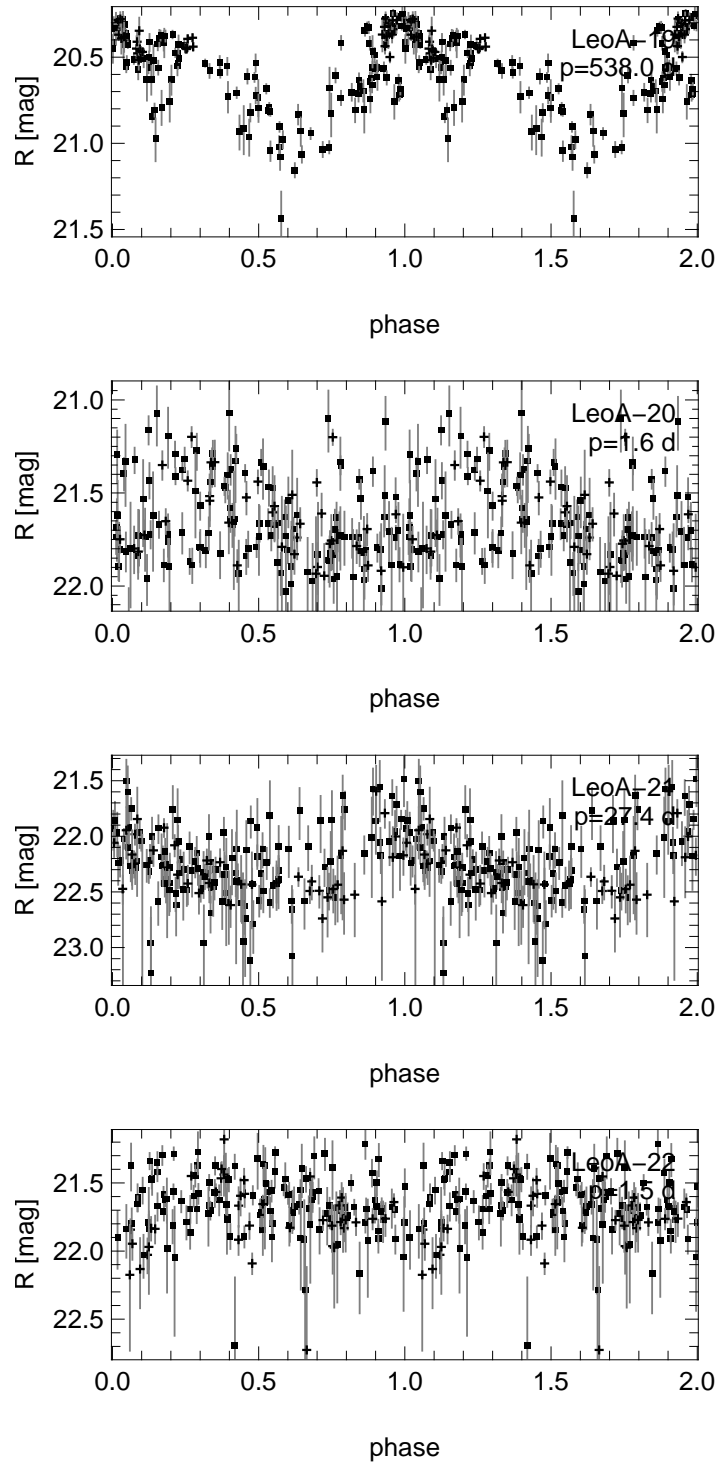


Figure B.6: Light-curves for variable sources found in the Leo A dwarf galaxy. Plotted is the  $R$ -band magnitude against the phase, repeated over for two phases to guide the eye. WST observations are plotted as squares, Calar Alto data as crosses.

## B.2 Light curves of DDO 216 variables

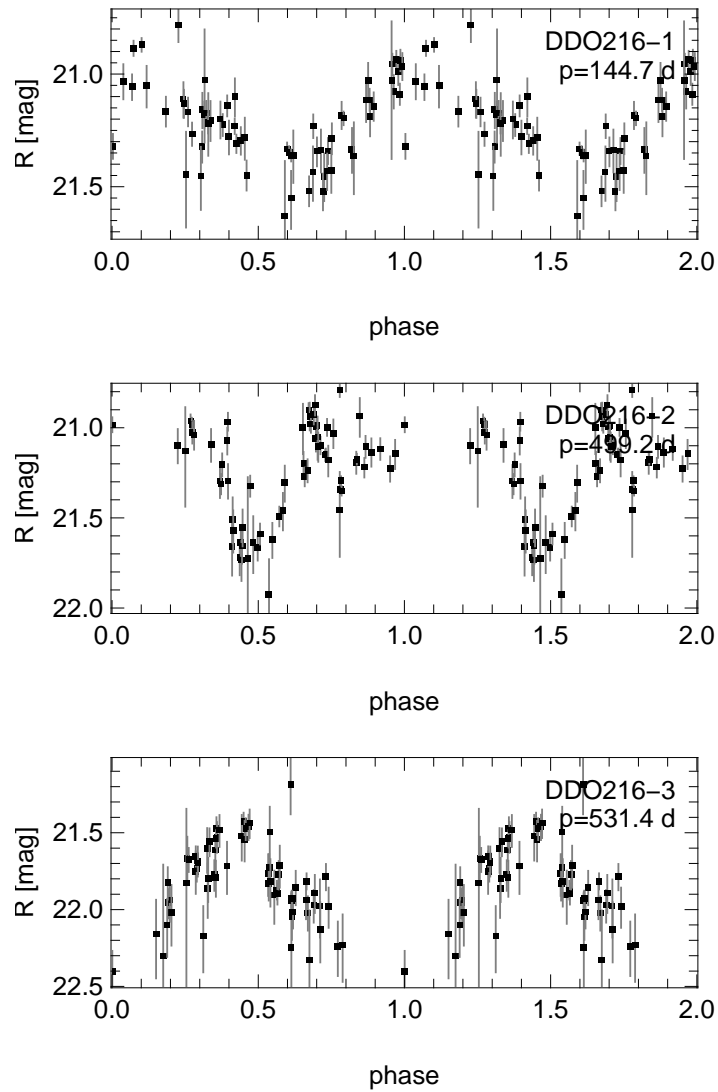


Figure B.7: Light-curves for variable sources found in the DDO 216 dwarf galaxy. Plotted is the  $R$ -band magnitude against the phase, repeated over for two phases to guide the eye.

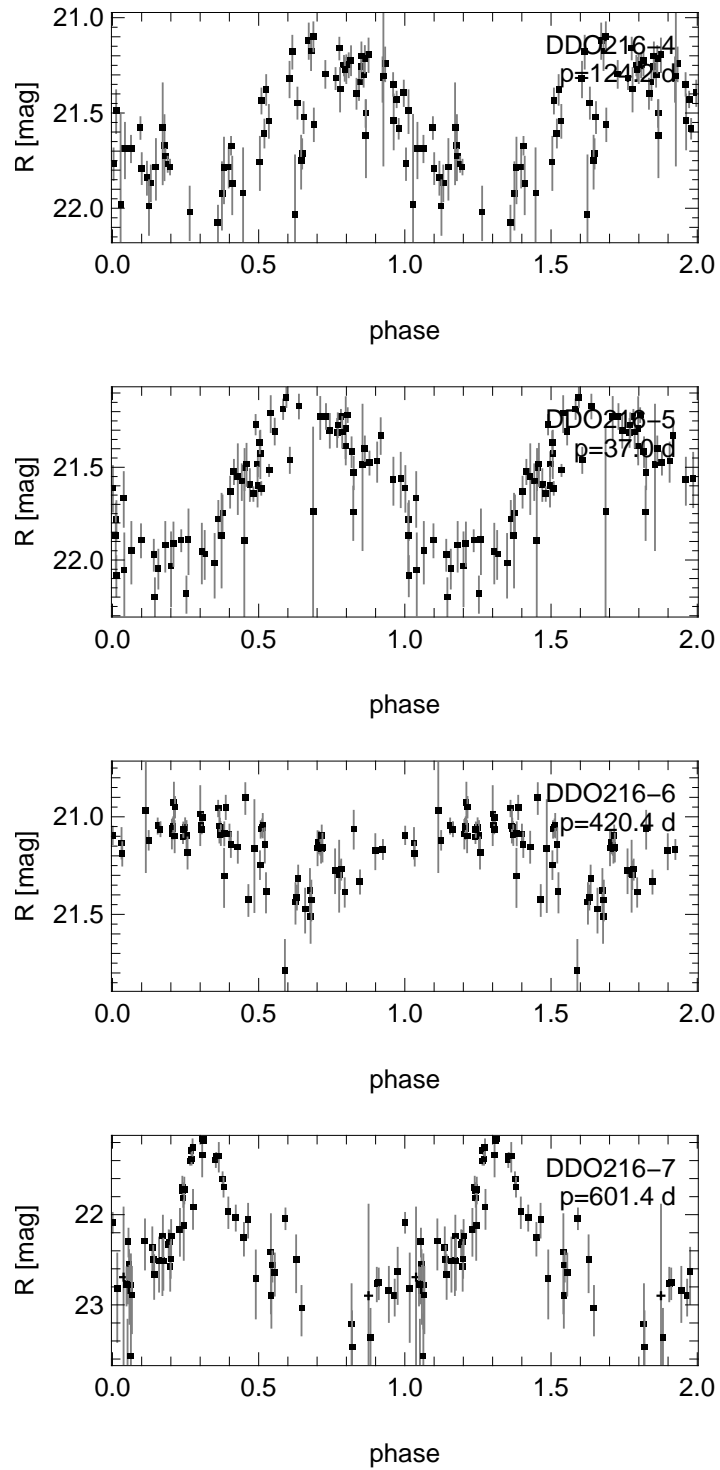


Figure B.8: Light-curves for variable sources found in the DDO 216 dwarf galaxy. Plotted is the  $R$ -band magnitude against the phase, repeated over for two phases to guide the eye.



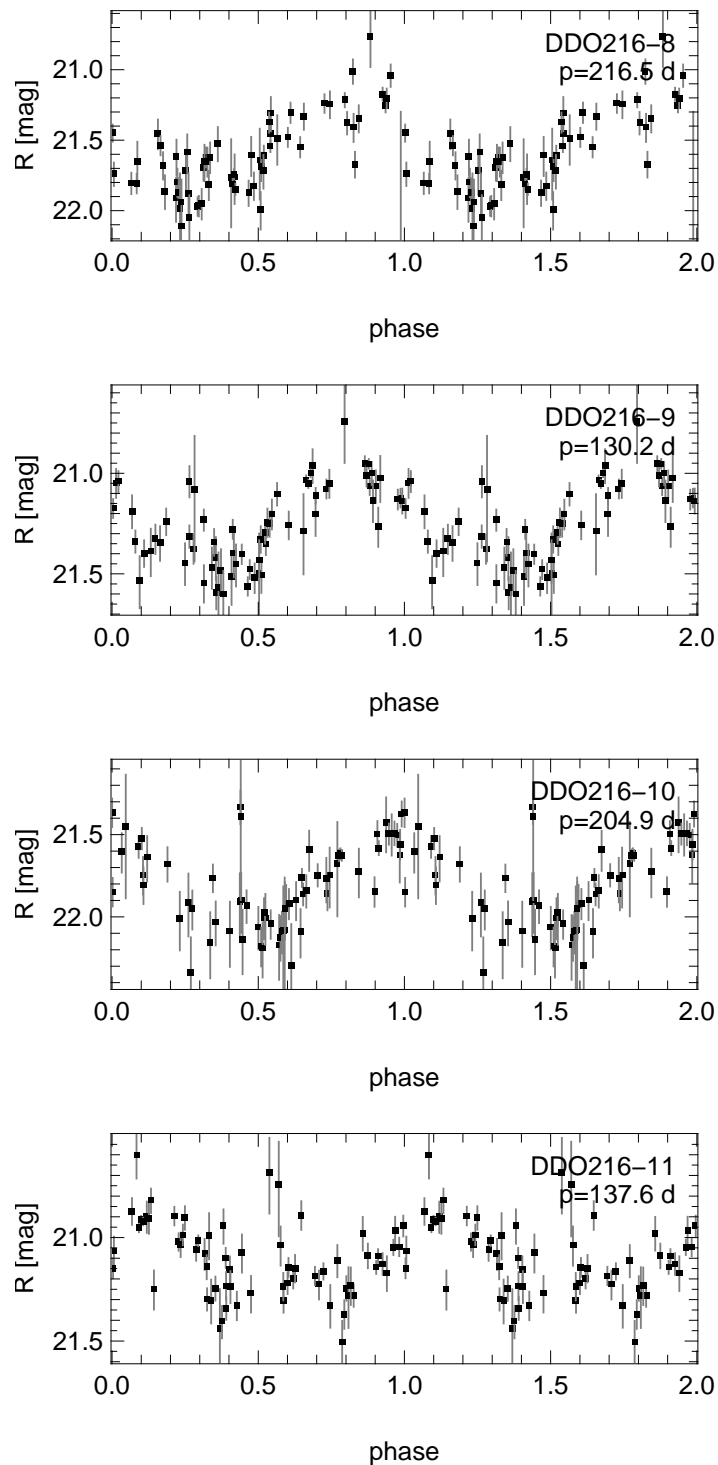


Figure B.9: Light-curves for variable sources found in the DDO 216 dwarf galaxy. Plotted is the  $R$ -band magnitude against the phase, repeated over for two phases to guide the eye.

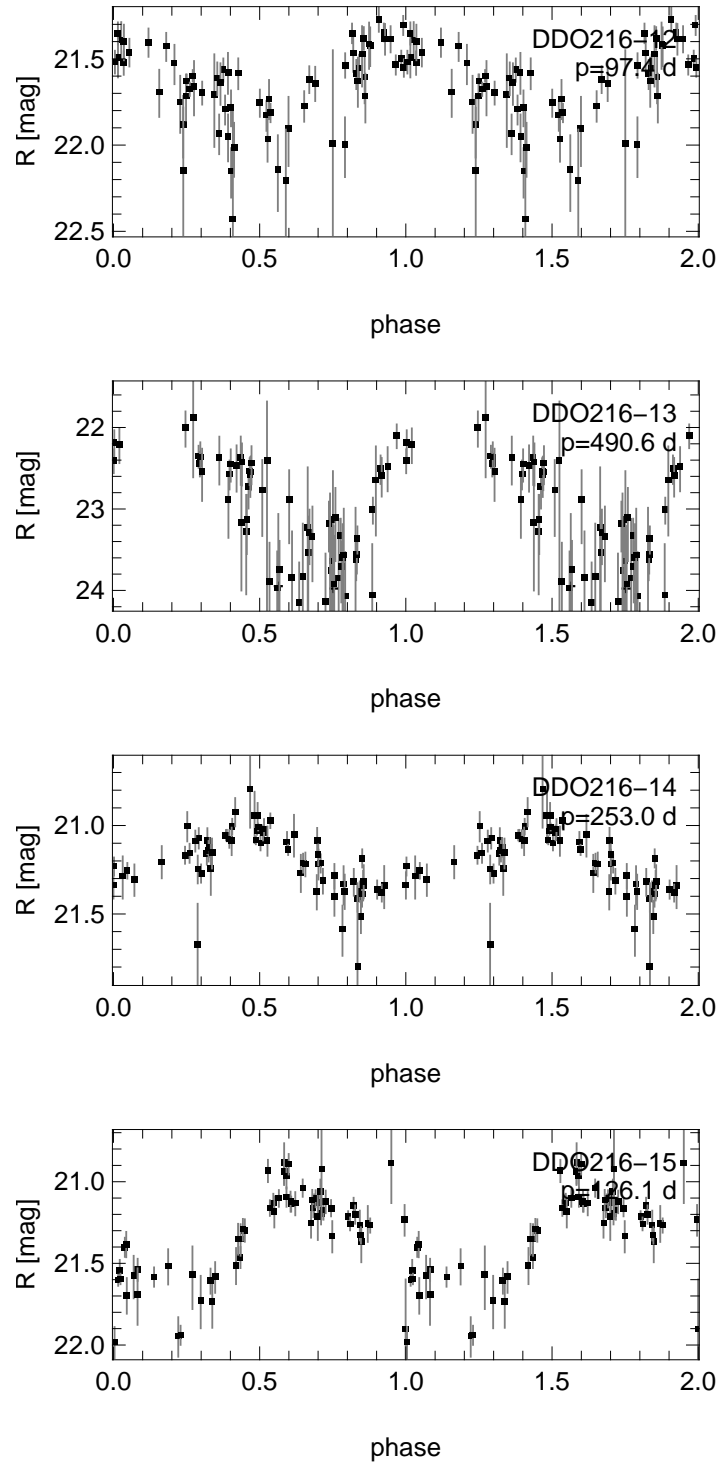


Figure B.10: Light-curves for variable sources found in the DDO 216 dwarf galaxy. Plotted is the  $R$ -band magnitude against the phase, repeated over for two phases to guide the eye.

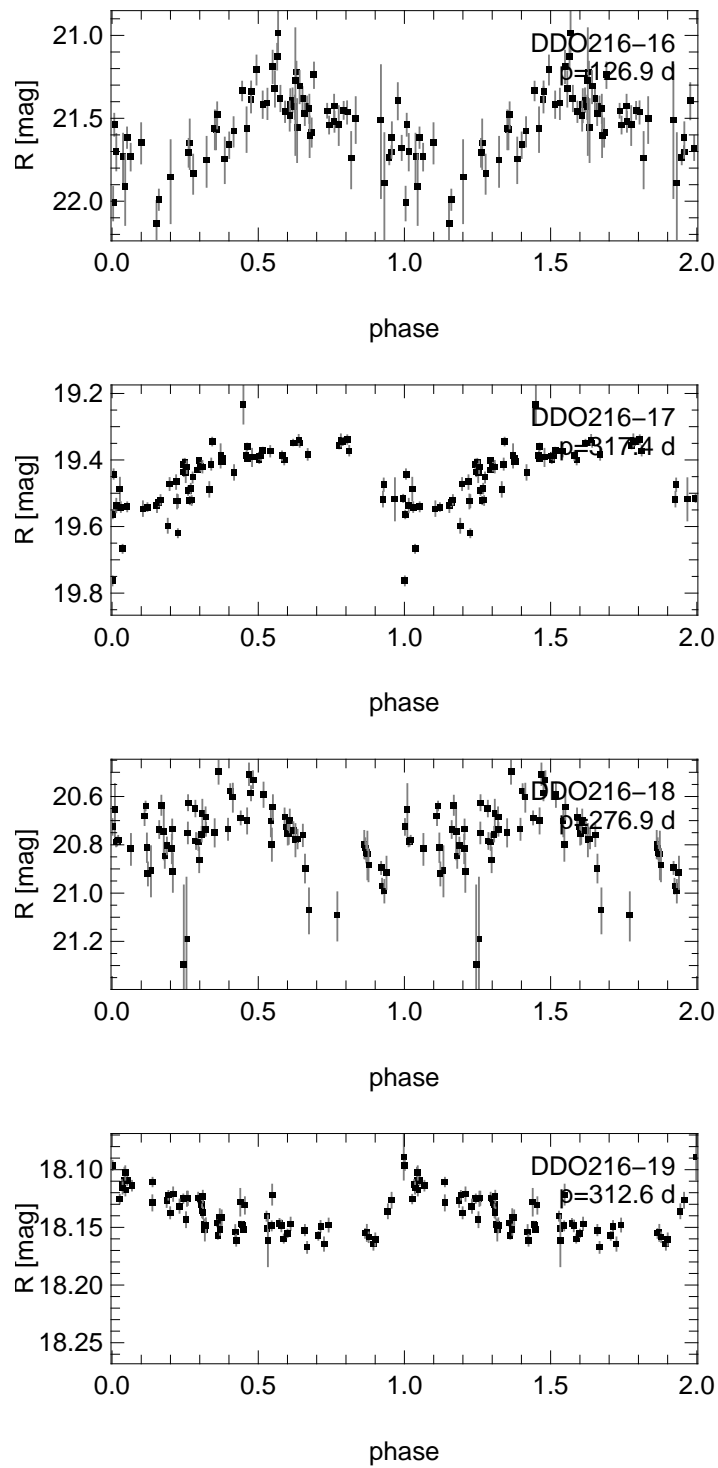


Figure B.11: Light-curves for variable sources found in the DDO 216 dwarf galaxy. Plotted is the  $R$ -band magnitude against the phase, repeated over for two phases to guide the eye.

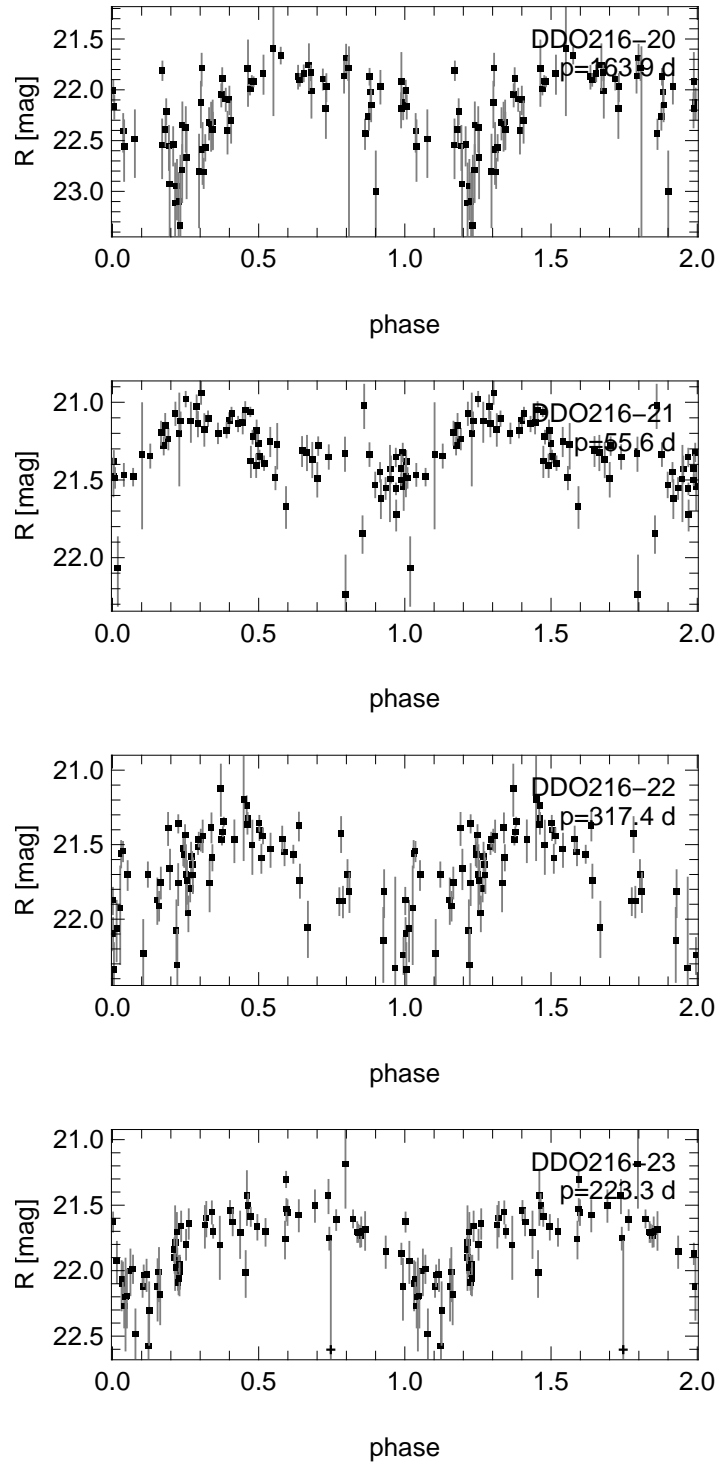


Figure B.12: Light-curves for variable sources found in the DDO 216 dwarf galaxy. Plotted is the  $R$ -band magnitude against the phase, repeated over for two phases to guide the eye.

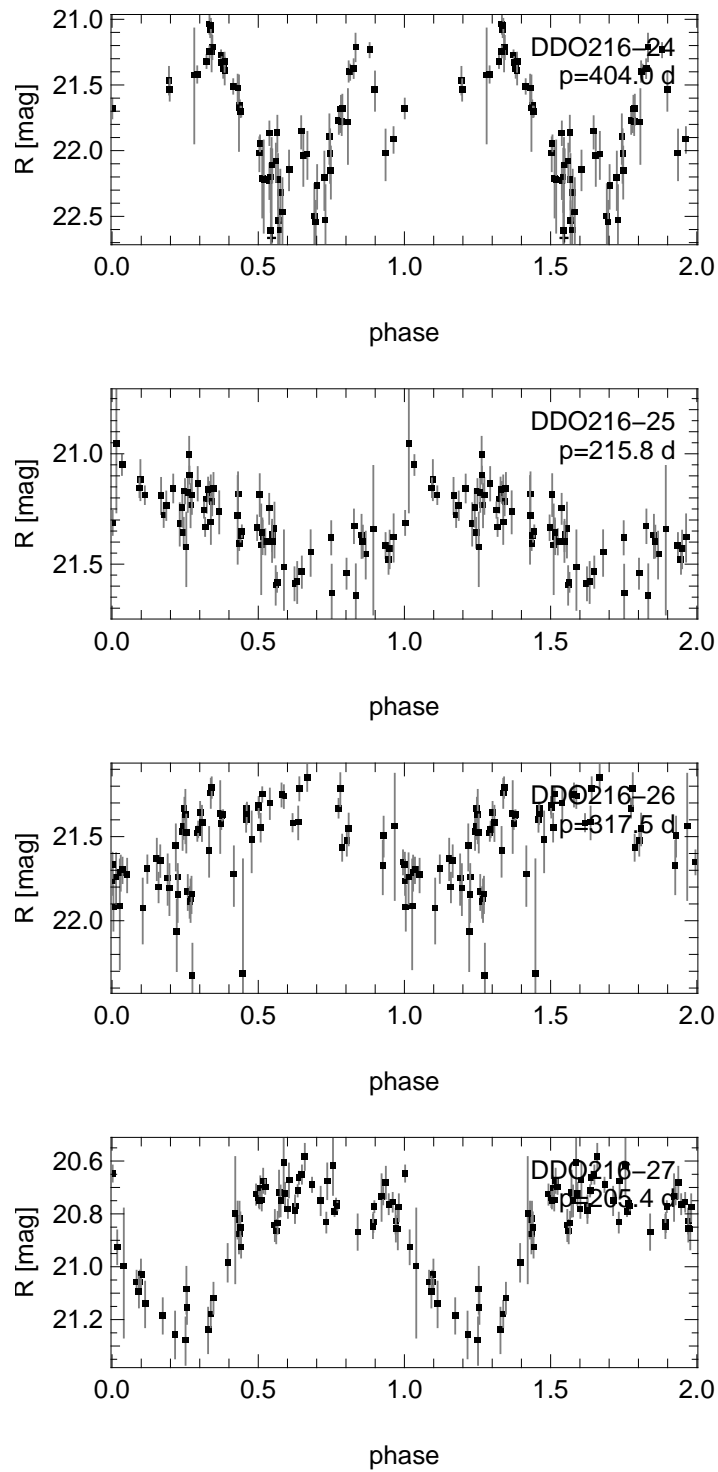


Figure B.13: Light-curves for variable sources found in the DDO 216 dwarf galaxy. Plotted is the  $R$ -band magnitude against the phase, repeated over for two phases to guide the eye.

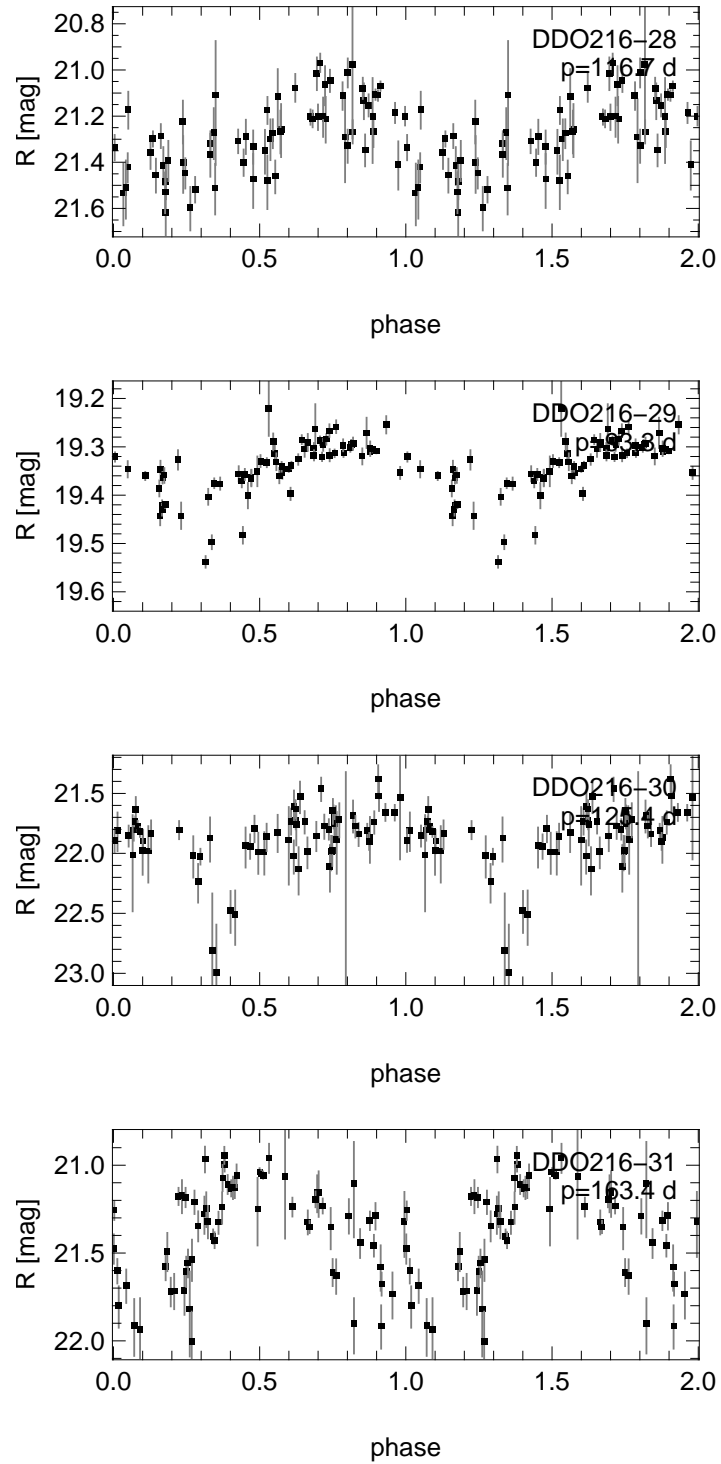


Figure B.14: Light-curves for variable sources found in the DDO 216 dwarf galaxy. Plotted is the  $R$ -band magnitude against the phase, repeated over for two phases to guide the eye.

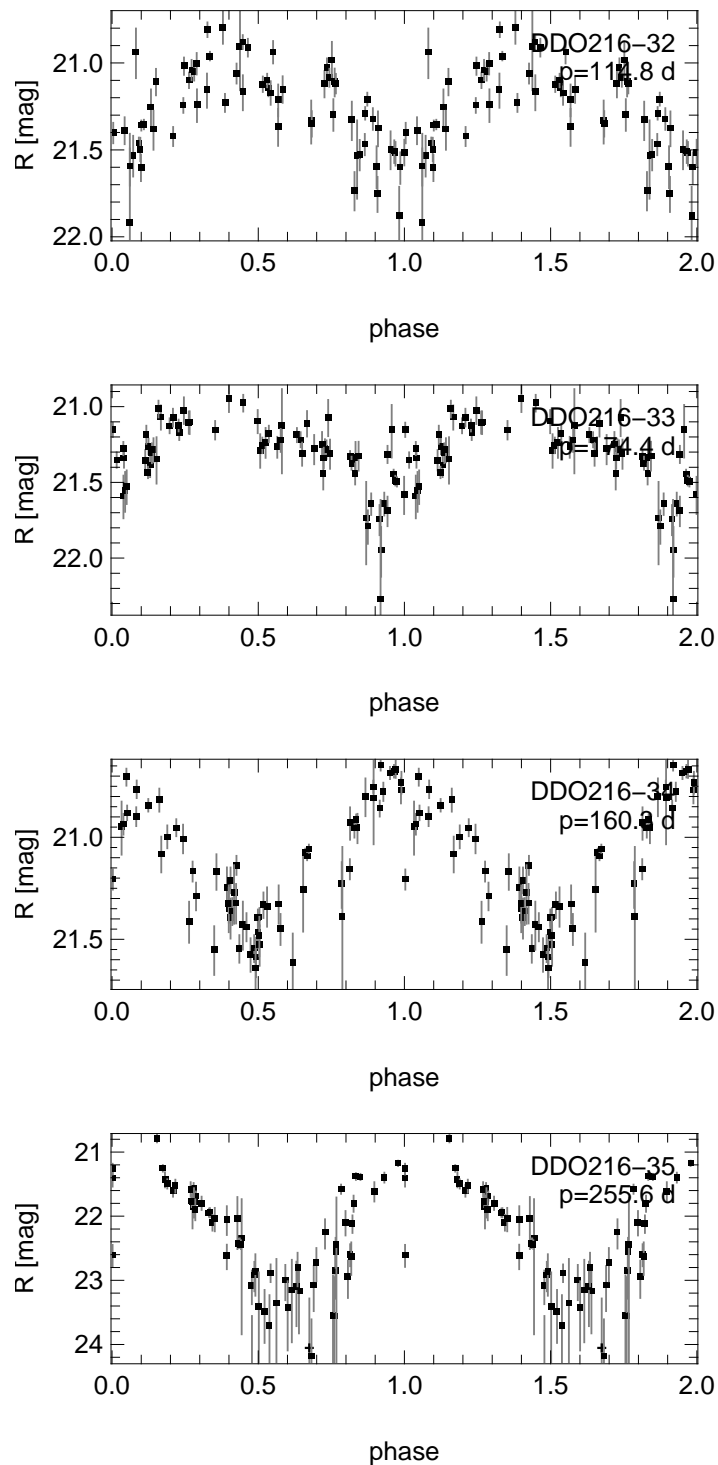


Figure B.15: Light-curves for variable sources found in the DDO 216 dwarf galaxy. Plotted is the  $R$ -band magnitude against the phase, repeated over for two phases to guide the eye.

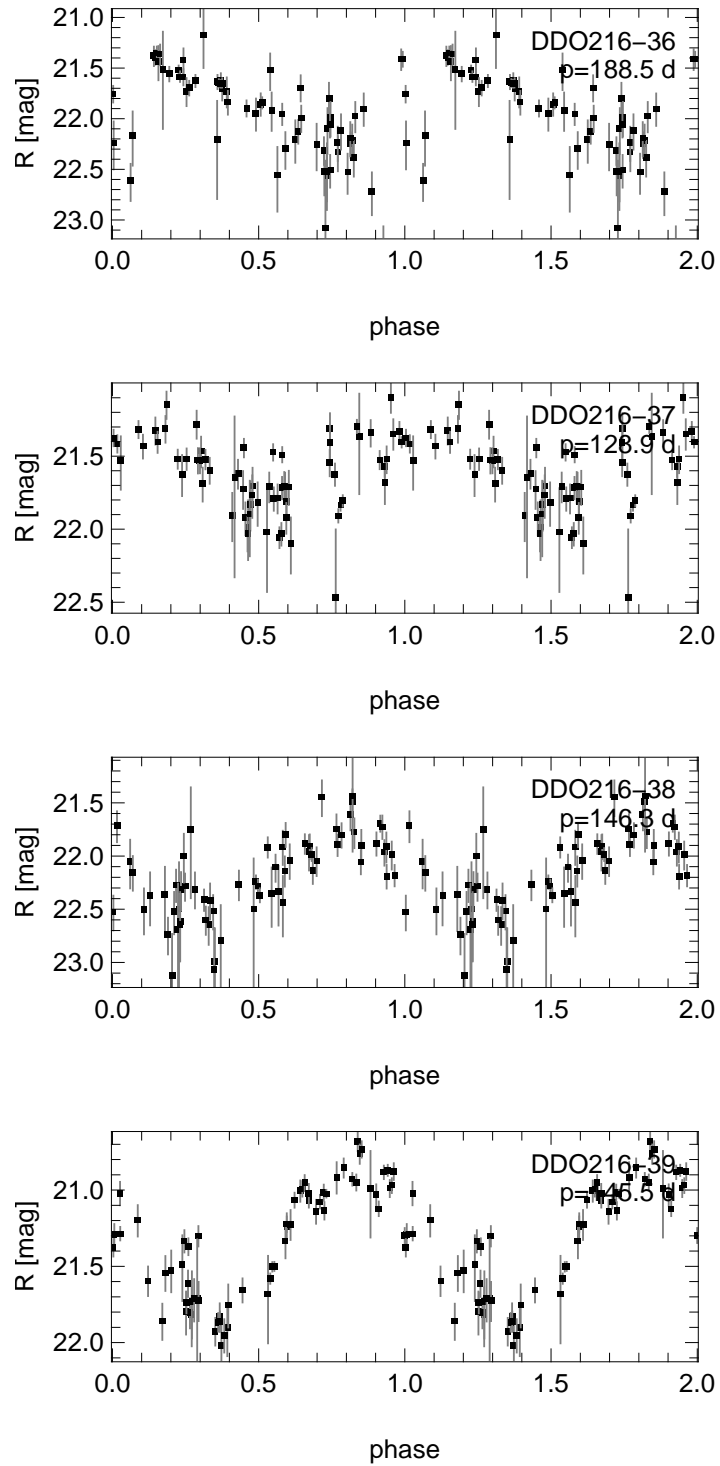


Figure B.16: Light-curves for variable sources found in the DDO 216 dwarf galaxy. Plotted is the  $R$ -band magnitude against the phase, repeated over for two phases to guide the eye.



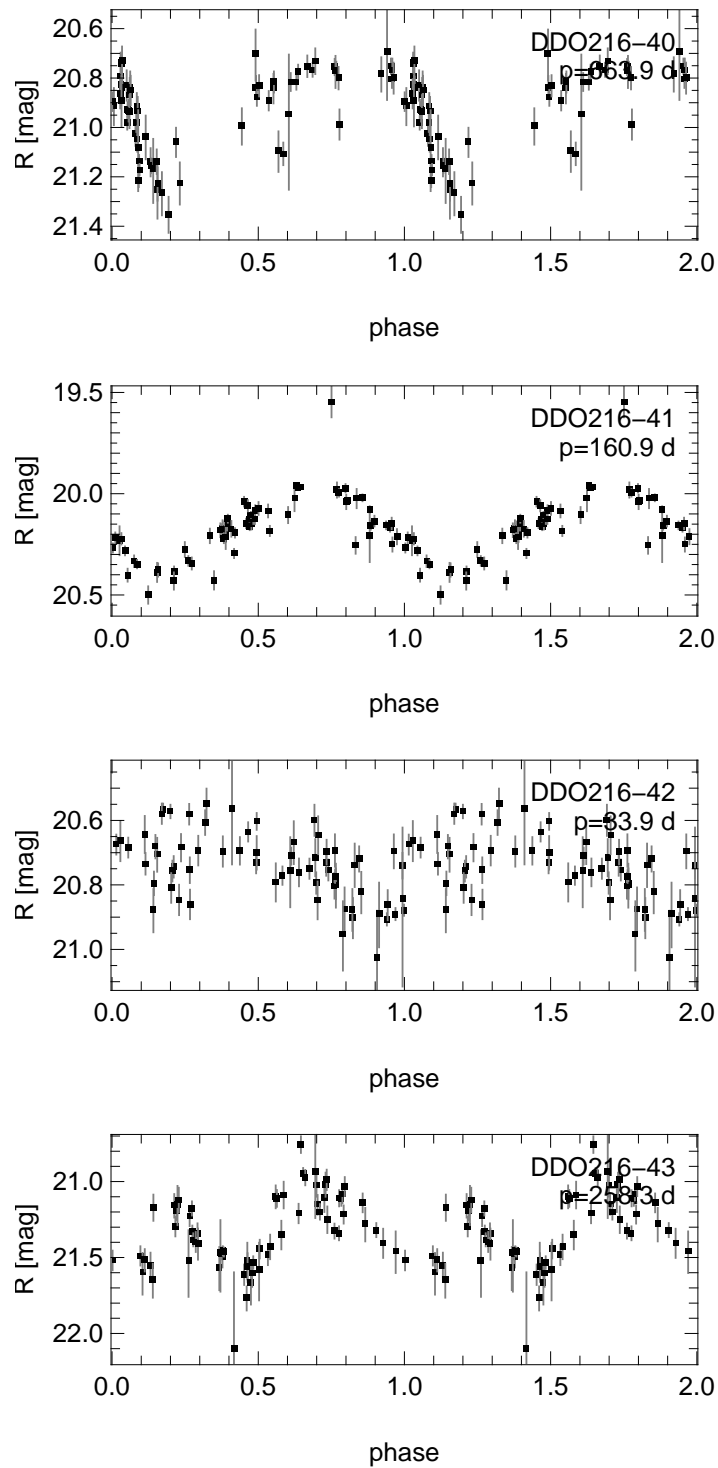


Figure B.17: Light-curves for variable sources found in the DDO 216 dwarf galaxy. Plotted is the  $R$ -band magnitude against the phase, repeated over for two phases to guide the eye.

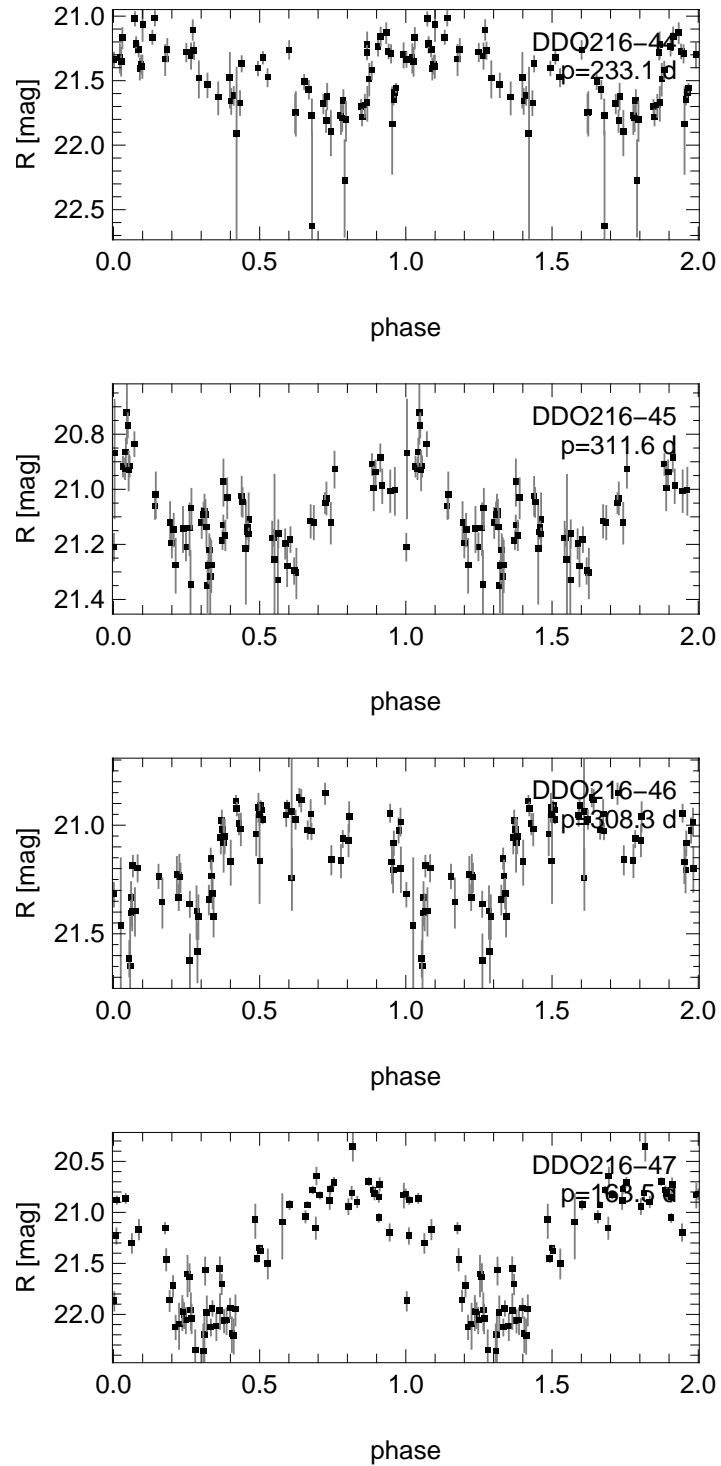


Figure B.18: Light-curves for variable sources found in the DDO 216 dwarf galaxy. Plotted is the  $R$ -band magnitude against the phase, repeated over for two phases to guide the eye.

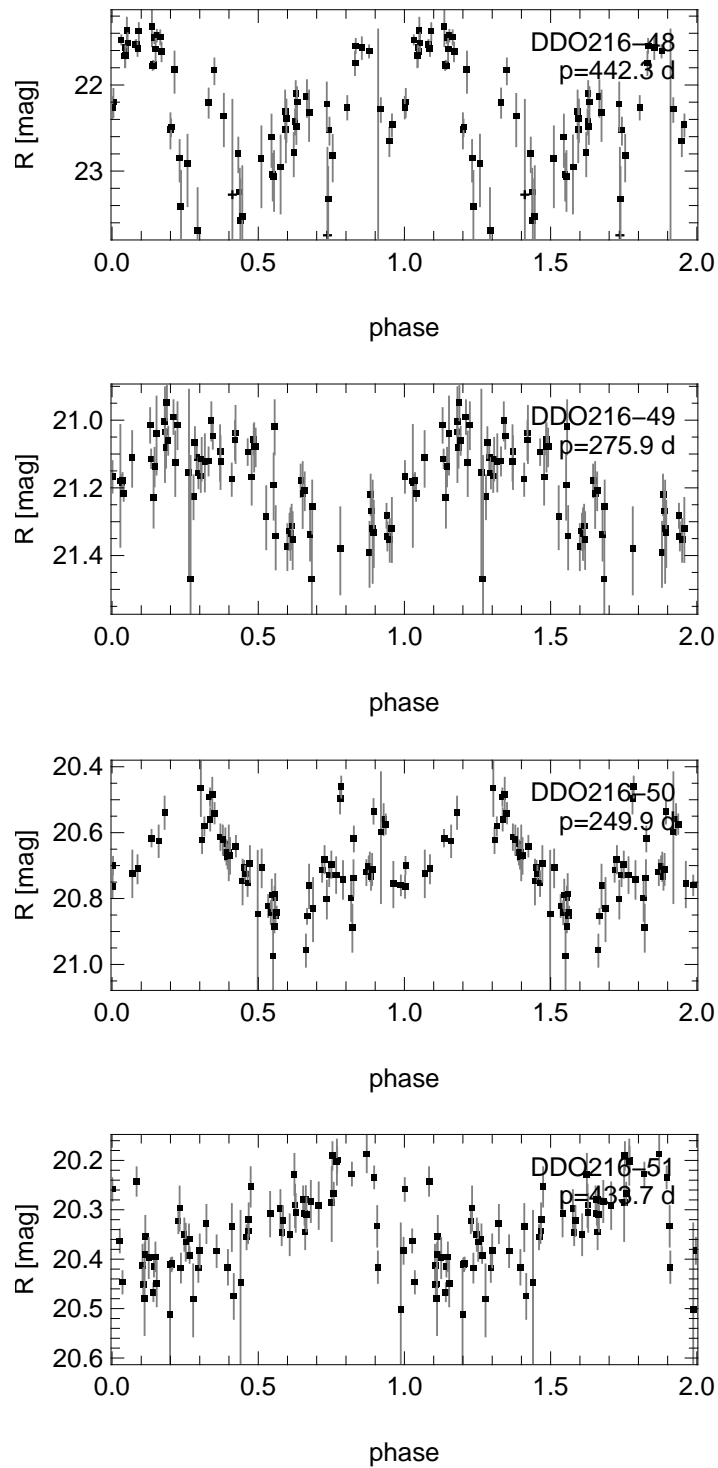


Figure B.19: Light-curves for variable sources found in the DDO 216 dwarf galaxy. Plotted is the  $R$ -band magnitude against the phase, repeated over for two phases to guide the eye.

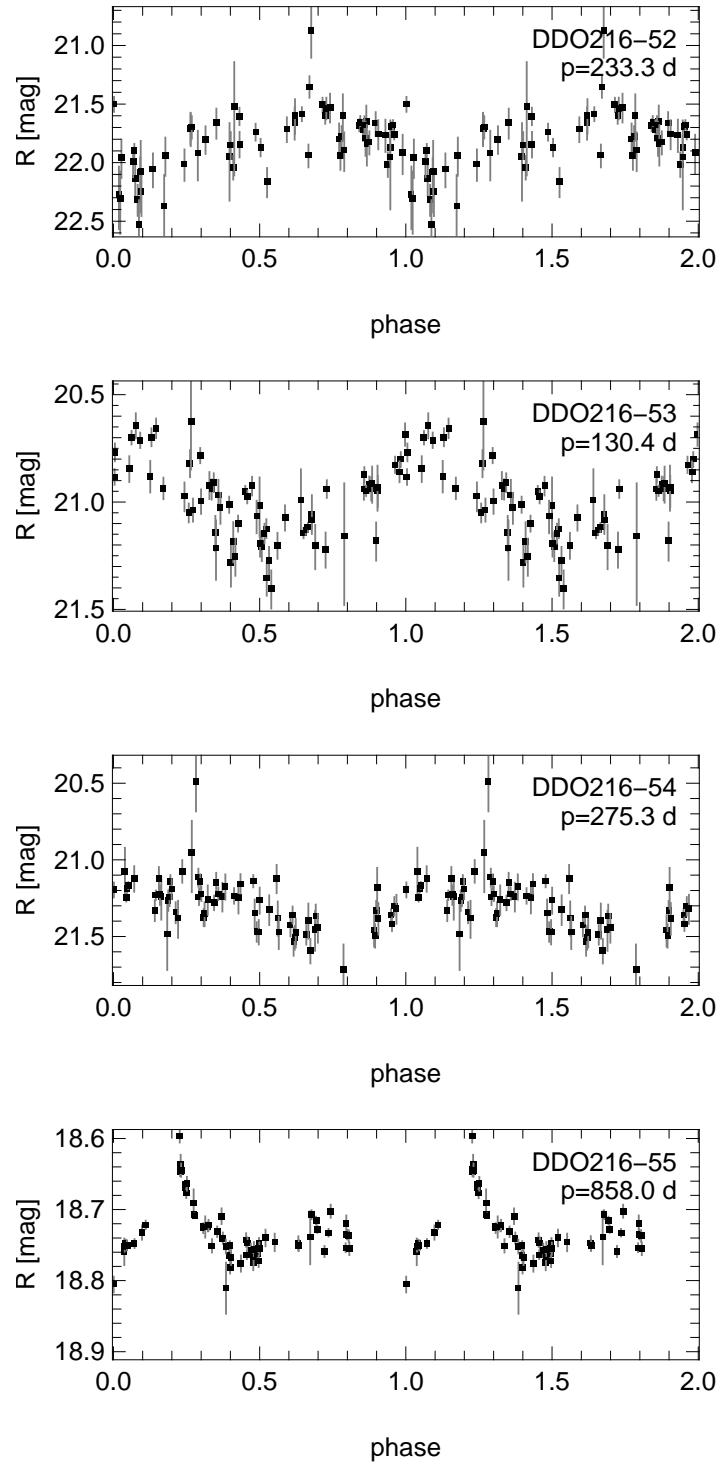


Figure B.20: Light-curves for variable sources found in the DDO 216 dwarf galaxy. Plotted is the  $R$ -band magnitude against the phase, repeated over for two phases to guide the eye.

### B.3 Light curves of GR 8 variables

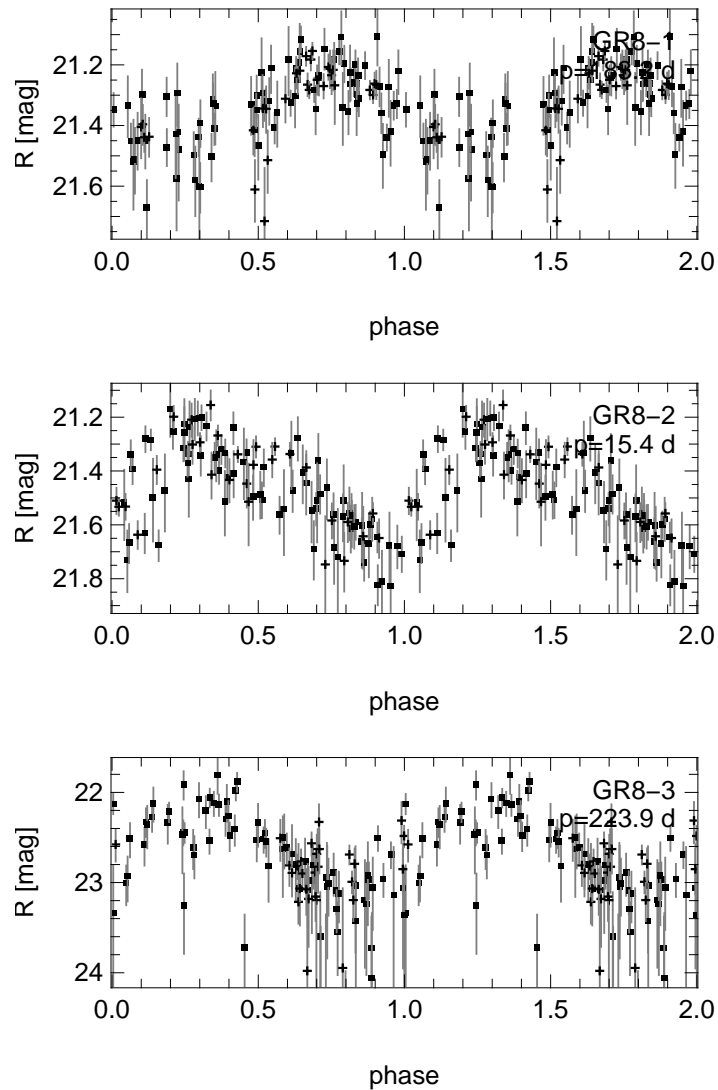


Figure B.21: Light-curves for variable sources found in the GR 8 dwarf galaxy. Plotted is the  $R$ -band magnitude against the phase, repeated over for two phases to guide the eye. WST observations are plotted as squares, Calar Alto data as crosses.



## **Appendix C**

# **TCS daemon commands**

This appendix provides a complete list of commands supported by the TCS daemon, see [chapter 7](#) for more details.

Command	description
tcsd set admin_port p	set admin port to p (admin)
tcsd set client_port p	set client port to p (admin)
tcsd set listen_port p	set listener port to p (admin)
tcsd set TCS relay_ip addr	set TCS relay IP address to addr (admin)
tcsd set TCS relay_port p	set TCS relay port to p (admin)
tcsd set Dome relay_ip addr	set Dome relay IP address to addr (admin)
tcsd set Dome relay_port p	set Dome relay port to p (admin)
tcsd set Slit relay_ip addr	set Slit relay IP address to addr (admin)
tcsd set Slit relay_port p	set Slit relay port to p (admin)
tcsd get TCS relay_ip	return TCS relay IP address (admin)
tcsd get TCS relay_port	return TCS relay port (admin)
tcsd get Dome relay_ip	return Dome relay IP address (admin)
tcsd get Dome relay_port	return Dome relay port (admin)
tcsd get Slit relay_ip	return Slit relay IP address (admin)
tcsd get Slit relay_port	return Slit relay port (admin)
tcsd get instrument_port	return instrument port (admin)
tcsd get admin_port	return admin port (admin)
tcsd get client_port	return client port (admin)
tcsd get listen_port	return listen port (admin)
tcsd reset client	reset the client connection (admin)
tcsd get state	return tcsd state information (admin)
tcsd restart daemon	restart the TCS daemon (admin)
set focus focus	set focus to focus (client)
set coords ra dec [epoch]	set coordinates to ra dec [epoch] (client)
set object d	set next object from TCS object list (client)
set offset d1 d2	set telescope offset (client)
set mark i ra dec [epoch]	set table position i to ra dec [epoch] (client)
move i	set next object to i from mark table (client)
go	start slewing (client)
zenith	move telescope to zenith (client)
stop	stop slewing (client)
get coords	send coords immediately to listeners (client)
get status	send status immediately to listeners (client)
get statcoords	send status and coords to listeners (client)
switch track [on/off]	switch track on or off (client)
switch auxtrack [on/off]	switch aux. track on or off (client)
switch drives [on/off]	switch Drives on or off (client)
switch dome [on/off]	switch dome track on or off (client)
switch autodome [on/off]	switch AutoDome on or off (client)
switch mdoors [open/close]	open or Close the mirror doors (client)
switch slit [open/close/off]	open / Close / Stop the dome slit (client)
switch magnet [on/off]	turn on or off the dome magnet (client)
help	show this help (client)
TCSC	return coordinates to the instrument (instrument)
TCSF focus	set the focus to focus (instrument)

Table C.1: Overview of the commands currently implemented in the TCS daemon



# Acknowledgements

First of all I would like to thank my thesis supervisor Ralf Bender for all his help throughout this project. Without him offering me a PhD position and without all his support the whole project would not have been possible.

Ulrich Hopp, my thesis advisor, deserves my deeply felt gratitude for all the time he invested on this project. Many of the things I know about astronomy today I learned from him, every so often through the sometimes puzzling questions he asked. He always was there, answering questions and enriching the project with new ideas. I would like to thank him for all his support and patience, and simply for being a good friend.

For all the work he contributed to our project alone Claus Gössl would deserve my deepest thanks. Without him all this would never have been possible, as he contributed so much in observing, programming, data reduction and thinking. In all the nights of observations, hours spent trying to solve mysterious problems or training Jiu-Jitsu he has become a great friend.

To my friend Chris Botzler I am deeply grateful for all the support she gave me during my work. Without her patient listening to my sometimes weird ideas, and all her comments and suggestions I probably would never have come that far.

It is a pleasure to thank Georg Feulner and Armin Gabasch for being such good company in the institute, for cheering me up in times of need and for keeping me mentally sane during this work. Both have become valued friends of mine.

Both Georg Feulner and Alekski Halkola deserve my thanks for proof-reading this thesis and pointing out all my mistakes in comma placement and usage of ancient english. Over many a game of snooker Alekski Halkola has become a friend.

I would like to thank my fellow students and roommates Niv Drory, Georg Feulner, Jürgen Fliri, Yulia Goranova, Claus Gössl, Alekski Halkola, Veronika Junk, Arno Riffeser, Jens Thomas, and Silona Wilke for all the discussions, the wonderful parties, all the cookies (thank you Veronika) and simply for the wonderful time we shared. The same is true for the guests and former and current members of our group, in particular Laura Gregg, Claudia Mendes de Oliveira, Mark Neeser, Roberto Saglia, Regina Schulte-Ladbeck and Stella Seitz.

I am deeply grateful to the staff observers at the observatory on Mt. Wendelstein. Without their countless nights spent observing for this project all this would never have been possible.

I would like to thank Maria-Rosa Cioni, Marina Rejkuba and Laura Greggio for helping me finding the right direction when it came to the study of the stellar populations.

The Deutsche Forschungs Gemeinschaft, the European Union and the Max-Planck Institut für Extraterrestrische Physik are thanked for supporting me during work, with special thanks to all the people working on the Astro-Wise project.

Special thanks go to the Calar Alto Observatory for giving us observing time at the 1.23m telescope.

At this point I would like to thank all of my friends for all the time spent together and for their friendship and support.

Last but definitely not least, I owe my deepest thanks to my parents, my sisters, my niece and my nephew for all their love, their encouragement and their endless support. Without them all this would never have been possible.

# Curriculum Vitae

## Persönliche Daten

Name: Jan Michael Snigula  
Geburtsdatum: 20. Dezember 1974  
Geburtsort: München  
Familienstand: Ledig  
Anschrift: Nördliche Münchnerstr. 3 B

## Ausbildung

1981 - 1985 Martin-Kneidl-Grundschule Grünwald  
1985 - 1994 Albert-Einstein-Gymnasium München  
1995 - 2000 Studium der Physik and der Ludwig-Maximilians-Universität München  
2000 - 2001 Diplomarbeit an der Universitäts-Sternwarte München über "Analyse der Galaxienverteilung in den Quasarfeldern des MUNICS-Surveys"  
2001 Diplom in Physik, LMU München  
2001 - 2006 Promotion in Astronomie an der LMU München

## Berufliche Tätigkeit

1994 - 1995 Zivildienst bei der Nachbarschaftshilfe Westermühlbach München  
2001 - 2002 Wissenschaftlicher Angestellter an der LMU München  
2002 - 2003 Wissenschaftlicher Angestellter an der LMU München im Rahmen des Astro-Wise Projektes  
2003 - Wissenschaftlicher Angestellter an der Max-Planck Gesellschaft für Extraterrestrische Physik in Garching bei München im Rahmen des Astro-Wise Projektes